# SOLID-STATE NMR SPECTROSCOPY APPLIED TO MODEL MEMBRANES: EFFECTS OF POLYUNSATURATED FATTY ACIDS

by

**Jacob Jerald Kinnun**

**A Dissertation**

*Submitted to the Faculty of Purdue University*
*In Partial Fulfillment of the Requirements for the degree of*

**Doctor of Philosophy**

Department of Physics

Indianapolis, Indiana

August 2018

**THE PURDUE UNIVERSITY GRADUATE SCHOOL**
**STATEMENT OF COMMITTEE APPROVAL**

Dr. Stephen R. Wassall, Chair
     Department of Physics

Dr. Horia I. Petrache
     Department of Physics

Dr. Yogesh N. Joglekar
     Department of Physics

Dr. Kenneth P. Ritchie
     Department of Physics

Dr. Fangqiang Zhu
     Department of Physics

**Approved by:**
     Dr. Ricardo S. Decca
          Head of the Graduate Program

# ACKNOWLEDGMENTS

In completing this work, no one has made more sacrifices than my wife, Maria. I am indebted to her for her hard work and understanding which allowed me to pursue this research. Importantly, I must also acknowledge my father, Gerald, my mother, Geraldine, and my sister, Michelle, who supported me and encouraged me when times were uncertain. As a younger student of science, two mentors, John Satter and Dr. Michael F. Brown encouraged me to be fearless in the pursuit of discovery. Without them I would have not seen the possible extent of my future potential and would not have attempted to go this far. In this vein I must also acknowledge fellow students who have encouraged me and aided me in my work, specifically Dr. Avigdor Leftin, Andres Cavazos, and Dr. Xiaoling Leng. This work could not have been completed without the facility managers of Dr. Bruce D. Ray and Dr. Andrey V. Struts who have helped educate me on the techniques that make this work possible. I also recognize my current and former committee members, Dr. Horia I. Petrache, Dr. Steve Pressé, Dr. Yogesh N. Joglekar, Dr. Ken Ritchie, and Dr. Fangqiang Zhu, for their time and advice in my research and the preparation of this dissertation. Finally, I have been exceptionally fortunate to have found Dr. Stephen R. Wassall as an advisor. His expertise and direction has been invaluable in my development as a scientist.

# TABLE OF CONTENTS

# LIST OF TABLES

# LIST OF FIGURES

# ABSTRACT

Author: Kinnun, Jacob Jerald. PhD
Institution: Purdue University
Degree Received: August 2018
Title: Solid-State NMR Spectroscopy Applied to Model Membranes: Effects of Polyunsaturated Fatty Acids
Committee Chair: Stephen R. Wassall

Omega-3 polyunsaturated fatty acids (n-3 PUFAs) relieve the symptoms of a wide variety of chronic inflammatory disorders. Typically, they must be obtained in the diet from sources such as fish oils. Docosahexaenoic acid (DHA) is one of these n-3 PUFAs. As yet the structural mechanism responsible for the health benefits within the body is not completely understood. One model that has emerged from biochemical and imaging studies of cells suggests that n-3 PUFAs are taken up into phospholipids in the plasma membrane. Thus the focus here is on the plasma membrane as a site of potential structural modification by DHA. Within cellular membranes, the huge variety of molecules (called lipids) which constitute the membrane suggest inhomogeneous mixing, thus domain formation. One potential domain of interest is called the lipid raft, which is primarily composed of sphingomyelin (SM) and cholesterol (chol). Here the molecular organization of $[^2H_{31}]$-$N$-palmitoylsphingomyelin (PSM-d$_{31}$) mixed with 1-palmitoyl-2-docosahexaenoylphosphatylcholine (PDPC) or 1-palmitoyl-2-oleoylphosphatidylcholine (POPC), as a monounsaturated control, and cholesterol (chol) (1:1:1 mol) in a model membrane was examined by solid state $^2H$ NMR spectroscopy.

Solid state $^2H$ NMR spectroscopy extracts details of molecular orientation and anisotropy of molecular reorientation by analysis of the lineshape. This essentially non-invasive technique allows for a direct measurement of dynamics in bulk materials which has been extensively applied to biological materials. It is a niche area of NMR for which standard software often lack necessary features. Two software programs, "EchoNMR processor" and "EchoNMR simulator", collectively known as "EchoNMR tools", that were developed to quickly process and analyze one-dimensional solid-state NMR data, will be described along with some theoretical background of the techniques used. EchoNMR tools has been

designed with a focus on usability and the open-source mindset. This is achieved in the in the MATLAB® programming environment which allows for the development of the graphical user interfaces and runs as an interpreter which allows the code to be open-source. The research described here on model membranes demonstrates the utility of the software.

The NMR spectra for PSM-$d_{31}$ in mixtures with PDPC or POPC with cholesterol were interpreted in terms of the presence of nano-sized SM-rich/chol-rich (raft-like) and PC-rich/chol-poor (non-raft) domains that become larger when POPC was replaced by PDPC. An increase in the differential in order and/or thickness between the two types of domains is responsible. The observation of separate signals from PSM-$d_{31}$, and correspondingly from $[3\alpha\text{-}^{2}H_{1}]$cholesterol (chol-$d_{1}$) and 1-$[^{2}H_{31}]$palmitoyl-2-docosahexaenoylphosphatidylcholine (PDPC-$d_{31}$), attributed to the raft-like and non-raft domains enabled the determination of the composition of the domains. Most of the SM (84%) and cholesterol (88%) was found in the raft-like domain. There was also a substantial amount of PDPC (70%) in the raft-like domain that appears to have minimal effect on the order of SM. PDPC molecules sequestering into small groups to minimize the contact of DHA chains with cholesterol is one possible explanation that would also have implications on raft continuity. These results refine the understanding of how DHA may modulate the structure of raft domains in membranes.

# CHAPTER 1.    BIOLOGICAL MEMBRANES

## 1.1    General Membrane Properties and Structure

One central aspect of life is that it requires a barrier to isolate and distinguish itself from its environment. Single celled organisms to multi-cellular animals all contain semipermeable barriers, called cellular membranes, of approximately 3 nm in thickness (van Meer, Voelker, & Feigenson, 2008). These membranes are composed of a group of amphiphatic molecules called lipids, that form a bilayer when dispersed in water because they have a head group region which is polar and an acyl chain region which is non-polar (Alberts et al., 2002). In nature lipid bilayers provide a structure for membrane proteins to reside and help regulate the flow of molecules in and out of the cell (Alberts et al., 2002). Within cells, the Golgi apparatus and the endoplasmic reticulum are collections of these lipid bilayers which aid in protein folding and protein insertion to the membrane (Farquhar & Palade, 1981). That environment is not dissimilar from the multilamellar vesicle environment (MLV) depicted in Figure 1.1, which consists of concentric lipid bilayers separated by an aqueous layer. Interestingly it has been shown that membrane thickness and tension modulates the activation of proteins (Brown, 2012; Gullingsrud & Schulten, 2004). With the many roles cellular membranes perform, it is difficult to overstate their importance in relation to biology.

The ability of lipids to form membranes is due to hydrophilic and hydrophobic interactions with water. Water molecules, due to their polarity, are very cohesive which results in water having a high surface tension (Pallas & Harrison, 1990). This also results in water excluding any molecules with a lack of polarity. Lipids, for the most part, have polar head groups but non-polar tails. This results in an interface between the water and the head groups with the tails excluded away (Tanford, 1980). There are a multitude of configurations which will allow for the packing of the lipid tails away from the water but the most common is the bilayer phase. This can occur in single bilayers (unilamellar vesicles) or, as shown in Figure 1.1, stacks of bilayers (multilamellar vesicles). In physiological temperatures often the lipids can laterally diffuse along these bilayers

(Nicolson, 2014). Thus cellular membranes are referred to as smectic liquid crystals, as they are liquid in the lateral direction and form crystalline stacks in a local normal direction (de Gennes, 1974). I use the term "local normal" as the soft nature of lipid bilayers results in the crystalline stacks becoming uncorrelated at long distances (Chaikin & Lubensky, 1995).

Before the early 1970's there were many competing models for membrane structure. Many suggested it was proteins which composed the primary constituent. However, it was the fluid mosaic model, coined by S. H. Singer and G. L. Nicolson, that suggested, at bare-minimum, cellular membranes were composed of lipids, with potentially embedded proteins, in the smectic liquid-crystalline phase (Nicolson, 2014). In modern times we have evidence of lateral inhomogeneity in terms of domain formation (Lingwood & Simons, 2010) and potential biological relevance for other phases (Jouhet, 2013) which were not considered in the original fluid mosaic model. Despite this, the model establishes a framework to build upon and discuss liquid-crystalline aspects of the membrane.

As liquid crystals are quantified by the analysis of order, they are often described in terms of an order parameter, $S$:

$$S = \langle \frac{3cos^2\theta - 1}{2} \rangle \tag{1.1}$$

where $\theta$ is the angle between the liquid-crystalline molecular axis and the local normal which is time averaged (Chaikin & Lubensky, 1995). For isotropic motion, which occurs in liquids, this parameter is reduced to zero. If the molecules are motionless and aligned such that $\theta = 0$, such as the case for many crystals, the order parameter is one. Thus the order parameter is particularly useful in parameterizing the liquid-crystalline properties of materials, such as lipid bilayers.

As opposed to dynamics, with liquid-crystals the structural properties of lipids can be discussed in terms of a unit cell shown in Figure 1.2 (Kinnun, Mallikarjunaiah, Petrache, & Brown, 2015). Similar to attributing an average volume per molecule as one would do for a gas, we can attribute an average cross-sectional area per lipid, $\langle A \rangle$, perpendicular to

the smectic phase normal. Then we can partition the interlamellar repeat spacing ($D$) into three parts: the water spacing ($D_w$) occupied by water, the length occupied by a lipid head group ($D_h$), and the average length occupied by lipid chains ($D_c$), which is called the hydrocarbon thickness. The associated volume for each partition can be found by multiplying the area per lipid by the associated length.

Interestingly for small environmental perturbations around physiological temperatures the chain group volume, $V_c$, is conserved (Petrache, Dodd, & Brown, 2000). This is due to the volume of the individual methylene groups and terminal methyl groups, that primarily compose lipid chain groups, being only slightly affected due to perturbations in the environment. This concept is particularly useful in making predictions on membrane structure if we have an idea of chain dynamics. Typically, the more ordered the chain is the less area it projects to the surface and the thicker in the membrane it is. This is exemplified in equation 1.2 with the help of equations 1.3 and 1.4 (Petrache et al., 2000).

$$V_c = D_c \langle A \rangle \tag{1.2}$$

Equivalently, the volume of a chain region is also proportional to the volume of the methylenes and terminal methyls for each chain of a lipid:

$$V_c = (n_{1c} + 1)V_{CH_2} + (n_{2c} + 1)V_{CH_2} \tag{1.3}$$

where $n_{1c}$ is the number of carbons of the first lipid chain and $n_{2c}$ is the number of carbons of the second lipid chain and $V_{CH_2}$ is the methylene volume. Here there are two assumptions. First that the volume of a terminal methyl is twice that of a methylene (Petrache, Feller, & Nagle, 1997). The second assumption is that neither chain has double bonds, which is not frequently the case (van Meer et al., 2008). For the last ingredient, the methylene volume can be approximated as:

$$V_{CH_2} \cong (26.5 \text{ Å}^3) + (0.0325 \text{ Å}^3/\text{C})T \tag{1.4}$$

where $T$ is the temperature in Celsius.

Despite the approximations, the combination of the preceding three equations remain useful. For example, it is common to have one saturated chain, and in this case you can consider a single chain volume by only considering half of equation 1.3. It is also possible

to modify equation 1.4 by taking away methylene groups and incorporating the volume of the unsaturated groups.

It is important to note that the structure and dynamics of liquid-crystals can be intimately related. For example, it often suffices to describe the structure of a liquid-crystalline molecule, or part of, in terms of a average projected length: $\langle D \rangle = D_m \langle cos\theta \rangle$ where $\langle D \rangle$ is the time-average projected length, $D_m$ is the maximum projected length of the molecule, and again $\theta$ is the angle between the liquid-crystalline molecular axis and the local normal. Often $\langle cos\theta \rangle$ can be determined from the order parameter in equation 1.1 and a statistical model (Petrache et al., 2000; Petrache, Tu, & Nagle, 1999). In general as the order parameter approaches zero, as does $\langle cos\theta \rangle$. Thus as a lipid bilayer becomes more disordered, the thinner it becomes as the projected length reduces, limited by volumetric constraints. Regardless of the groups, the volumes do not vary greatly around physiological temperatures as shown by equation 1.4. Thus one can take $V_c$ to be approximately constant and make inferences on membrane area with equation 1.2 (Petrache et al., 2000). If a disordered lipid bilayer is thinner, then via equation 1.2, the area per molecule tends to increase.

## 1.2    Anatomy of a Lipid

In general lipids need at least two chemical groups where one has the property of being polar and the other apolar. Often these groups are linked together by a backbone (linker) such as glycerol. Glycerophospholipids, which have this linker and a head group based on a phosphate molecule, are the most common lipid found in nature (McKee & McKee, 2015). Although these lipids come with a wide variety of chain groups, two common chains are the saturated palmitoyl with 16 carbons (16:0) and mono-unsaturated oleoyl with 18 carbons (18:0) as shown in Figure 1.3. Together with the head group of phosphocholine they form the lipid 1-palmitoyl-2-oleoyl-sn-glycero-3-phosphocholine (POPC, 16:0-18:1). POPC is one of the most common lipids found in nature and therefore makes a good reference point when studying other lipids (van Meer et al., 2008).

Another biologically important group of lipids are the sphingolipids based on the sphingosine back bone, again shown in Figure 1.3. They were discovered in the myelin sheath that cover some nerve cells but also found in most animal cell membranes (McKee & McKee, 2015). Interestingly, there is increasing evidence, some which I will show later, that show they can segregate from other lipids (Edidin, 2003) and form domains which are called rafts.

Biology is complex as it need not be efficient but sufficient, therefore there are many other lipids which do not obey the structural motif I have outlined. Cholesterol and alpha-tocopherol (vitamin E), also shown in Figure 1.3, are mostly apolar but have a polar hydroxide group, thus satisfying the amphiphilic nature of a lipid. Many other lipid-soluble vitamins and hormones have similar motifs with ring structures and hydroxide groups. Even though they obey a different motif they can be just as important as the phospholipids themselves. In fact, in some membranes, cholesterol can be one to one with the phospholipids in composition (Cooper, 2000).

The last structural group of many lipids that I would like to point out are the hydrocarbon chains. They can be of different carbon lengths and double bond count (called unsaturation as it reduces the hydrogen content). The chain length and saturation plays an important role in the phase and structural role of the membrane. When referring to specific sites on the chain, the typical numbering scheme begins from the oxygen-containing carbonyl and increases down the chain to the methyl. Numbering schemes which start at the methyl are denoted by n or omega (ω). Chains of multiple double bonds, polyunsaturated fatty acids (PUFAs), are of particular importance and thus interest. For example a lack of dietary intake of omega-3 polyunsaturated fatty acids (n-3 PUFAs) has been associated with inflammatory diseases such as inflammatory bowel disorder, cardiovascular disease, rheumatoid arthritis, nonalcoholic fatty liver disease and other diseases such as obesity and Alzheimer's disease (Calder, 2013; Patterson, Wall, Fitzgerald, Ross, & Stanton, 2012). These omega-3 fatty acids are characterized by having their last double bond 3 carbons away from the terminal (omega) methyl of the hydrocarbon chain. Humans cannot synthesize these fatty acids but must obtain them from the diet such as from fish oils where

docosahexaenoic acid is a major constituent (DHA, 22:6) (W. S. Harris et al., 2009; Kučerka et al., 2010; Lingwood & Simons, 2010; Shaikh, Brzustowicz, Gustafson, Stillwell, & Wassall, 2002; Soubias & Gawrisch, 2007; Yaqoob & Shaikh, 2010) as shown in Figure 1.3. Given that dietary intake of n-3 PUFAs alter the membrane composition of living animals (Abbott, Else, Atkins, & Hulbert, 2012), it has been suggested that the effect of n-3 PUFAs on health is, in part, membrane mediated  (Shaikh, Kinnun, Leng, Williams, & Wassall, 2015; Stillwell & Wassall, 2003; Wassall & Stillwell, 2008; Yaqoob & Shaikh, 2010). Given that membrane composition is affected by dietary n-3 PUFAs, they have the potential to affect the structure of the lipid membrane which is under investigation here.

## 1.3    Lipid Dynamics and Phase Behavior

In their physiological form, cellular membranes are most often in their liquid-crystalline state, called the liquid disordered state ($L_d$). In this state, the lipid chains undergo rapid isomerizations about C-C bonds and the lipids can diffuse. This allows liquid-crystalline structures to be more dynamical and flexible than normal solids. Typically, adjacent membranes attract each other due to van der Waals forces, however due to their soft nature the bilayers undergo fluctuations, called undulations, and can repulse each other in close ranges (Israelachvili & Wennerström, 1992).

I described the lipid bilayer as a liquid crystal, but the lipids do not diffuse as a 2D liquid for all temperatures nor physiological conditions. If we cool lipids below normal physiological temperatures, they can enter the gel state, where the rapid isomerizations are greatly reduced, which is a smectic-C liquid crystal (Janiak, Small, & Shipley, 1979). Interestingly the diffusion of the lipids has stopped but the solute, which is typically mostly water, can still be in its liquid form. Thus the liquid-crystalline style of nomenclature is often used. More commonly, and here, this phase is referred to as a solid ordered ($S_o$) phase.

With cholesterol, lipid chain motion can be restricted but the lipids can still diffuse. Lipid chain motion is restricted due to the influence of cholesterol's rigid sterol ring. Samples with cholesterol also are known to have very broad phase transitions, which implies that cholesterol reduces the interaction thus cooperativity between lipids (McKersie &

Thompson, 1979). This is not surprising as one can imagine cholesterol acting as a spacer between lipids, thus reducing their interaction. Since the lipids can diffuse but the chains are ordered in this phase, this is referred to as a liquid ordered phase ($L_o$).

## 1.4 Phase Segregation

As mentioned, physiological membranes contain a large variety of lipids. Some lipids such as palmitoyl sphingomyelin (PSM) have a $S_o$ to $L_d$ phase transition (sometimes called a melting temperature) above the average core body temperature, while other lipids, such as POPC have this phase transition below. Thus in some mixed-lipid membranes phase segregation can occur, where some parts of the membrane are in one phase and the rest in another. The potential physiological importance of phase segregation is the subject of intensive research (Edidin, 2003).

The prime candidate for phase segregation in physiological membranes are call raft domains, or just rafts for short (I. Levental, Grzybek, & Simons, 2010). These rafts are primarily composed of sphingomyelin and cholesterol (Stillwell, 2013; Wassall & Stillwell, 2008) and can potentially be up to 1 micron in diameter but as of yet there is no consensus (Edidin, 2003). They tend to be quite ordered, in a $L_o$ phase, compared to the rest of the membrane which is in a $L_d$ phase (Shaikh, Kinnun, et al., 2015). As lipid volume tends to be preserved, ordered acyl chains produce thicker membranes; thus rafts tend to be thicker than the surrounding membrane. Studies show these rafts contain signaling proteins, thus modifications of their structure are of biological importance (I. Levental et al., 2010; Shaikh, 2012; Shaikh, Wassall, Brown, & R. Kosaraju, 2015; Simons & Toomre, 2000).

In natural systems there are likely many causes for domain formation, where the importance of each is under debate (Almeida, Pokorny, & Hinderliter, 2005). Here I will discuss two causes which have received attention: domain thickness mismatch and cholesterol preference. Domain formation can be discussed terms of unfavorable interaction between domains. That is, there is an energy cost per length of contact between domains. This has the units of force and is given the name: line tension ($\lambda$). You can imagine the line tension as a lasso whose force pulls like lipids together (McConnell, 1991).

The most energetically favorable state has all of the domain-forming lipids in one circular domain which minimizes its contact with the surroundings. However, this is only one configuration of lipids and thus entropically improbable. Therefore, thermal fluctuations often oppose excessively large domains. Electrostatics and volumetric exclusion can also cause lipids to repel as well (Kuzmin, Akimov, Chizmadzhev, Zimmerberg, & Cohen, 2005). However, I will focus on two potential causes of line tension thus domain formation as opposed to lipid repulsion.

One of the most studied forms of line tension is due to thickness mismatch between domains. For the membrane to compensate between different thicknesses, where an ordered domain has a larger thickness of $h_o$ and the disordered domain has a smaller thickness of $h_d$, each monolayer leaflet undergoes strain at the domain boundaries. This is an energy cost which is proportional to the length of the boundary. Thus this generates a line tension as given by equation 1.5:

$$\lambda = \left(\frac{\delta^2}{h_0^2}\right)\frac{\sqrt{B_d K_d B_o K_o}}{\sqrt{B_d K_d} + \sqrt{B_o K_o}} - \left(\frac{1}{2}\right)\frac{(B_d J_d - B_o J_o)^2}{\sqrt{B_d K_d} + \sqrt{B_o K_o}} \tag{1.5}$$

where $\delta = h_o - h_d$, $h_0 = (h_o + h_d)/2$, $B$ is the elastic splay modulus, $K$ is the tilt modulus, and $J$ is the spontaneous curvature for each domain respectively (Kuzmin et al., 2005). In general the stiffer each domain is (thus larger $B$ and $K$) the larger the line tension is thus larger domain formation. However spontaneous curvature has the opposite effect. Lipids that can form curved phases can relieve stresses at the domain boundaries thus reducing line tension.

Concerning rafts and other natural membranes, cholesterol seems to be very important in domain formation (Engberg, Hautala, et al., 2016; Veatch & Keller, 2003b). Most compositions which reveal large-scale domains in lipid membranes contain cholesterol (Veatch & Keller, 2003b; Veatch, Polozov, Gawrisch, & Keller, 2004). What makes cholesterol interesting is that most of it is locked in a rigid ring structure (see Figure 1.3). Because of this, it is believed that cholesterol has unfavorable interactions with disordered lipids (Shaikh, Kinnun, et al., 2015). Remember that unfavorable interactions generate line tension. One reason for this unfavorable interaction is that it is entropically costly for a

disordered lipid to orderly pack around a rigid cholesterol molecule (Almeida et al., 2005). Therefore cholesterol is entropically driven towards more ordered lipids, such as sphingomyelin, where entropic costs of ordering is less (Wassall & Stillwell, 2008). Some authors have even argued that cholesterol preference may be the primary driving force in biological domain formation (Lin et al., 2016).

The story of domain formation in natural membranes may be a synergistic one. Typically studies which look at hydrophobic mismatch increasing domain size also contain cholesterol (Heberle et al., 2013). Conversely, studies which look at cholesterol in forming domains also tend to find that increasing thickness mismatch between domains increases domain size (Veatch & Keller, 2003b). While segregated into a domain, the ordering effect of cholesterol should not be discounted as it increases domain thickness (Bunge, Müller, Stöckl, Herrmann, & Huster, 2008). This ordering effect could accentuate the thickness mismatch, therefore synergistically producing larger domains.

The importance of cholesterol preference leads to a possible role of n-3 PUFAs in living organisms. These n-3 PUFAs have repeating =CH-CH$_2$= segments within which the energy barrier to rotation about C-C bonds is extremely shallow (Feller, Gawrisch, & MacKerell, 2001). Thus n-3 PUFAs are incredibly disordered and very dissimilar to raft-like domains (Wassall & Stillwell, 2008), which leads to a very low cholesterol preference. This idea is consistent with the experimental observation that n-3 PUFAs increase the size of raft domains (Georgieva et al., 2015; Soni et al., 2008; Williams et al., 2012).

Interestingly a difference in head groups between n-3 PUFA containing phospholipids yield different domain forming properties. In general n-3 PUFAs with phosphoethanolamine (PE) head groups form smaller domains than with a phosphocholine (PC) head group (Shaikh, Kinnun, et al., 2015; Shaikh, LoCascio, Soni, Wassall, & Stillwell, 2009; Soni et al., 2008; Williams et al., 2012). This could be due to the smaller PE (in terms of area) head group producing thicker lipid chains (see equation 1.2) thus reducing the line tension with the raft domain (see equation 1.5). Further, it has been shown that DHA with a PC head group when added to model raft-like systems can enter raft

domains (Williams et al., 2012). The question of how it modifies the structure of these domains is of importance and will be addressed here using solid state $^2$H NMR spectroscopy.
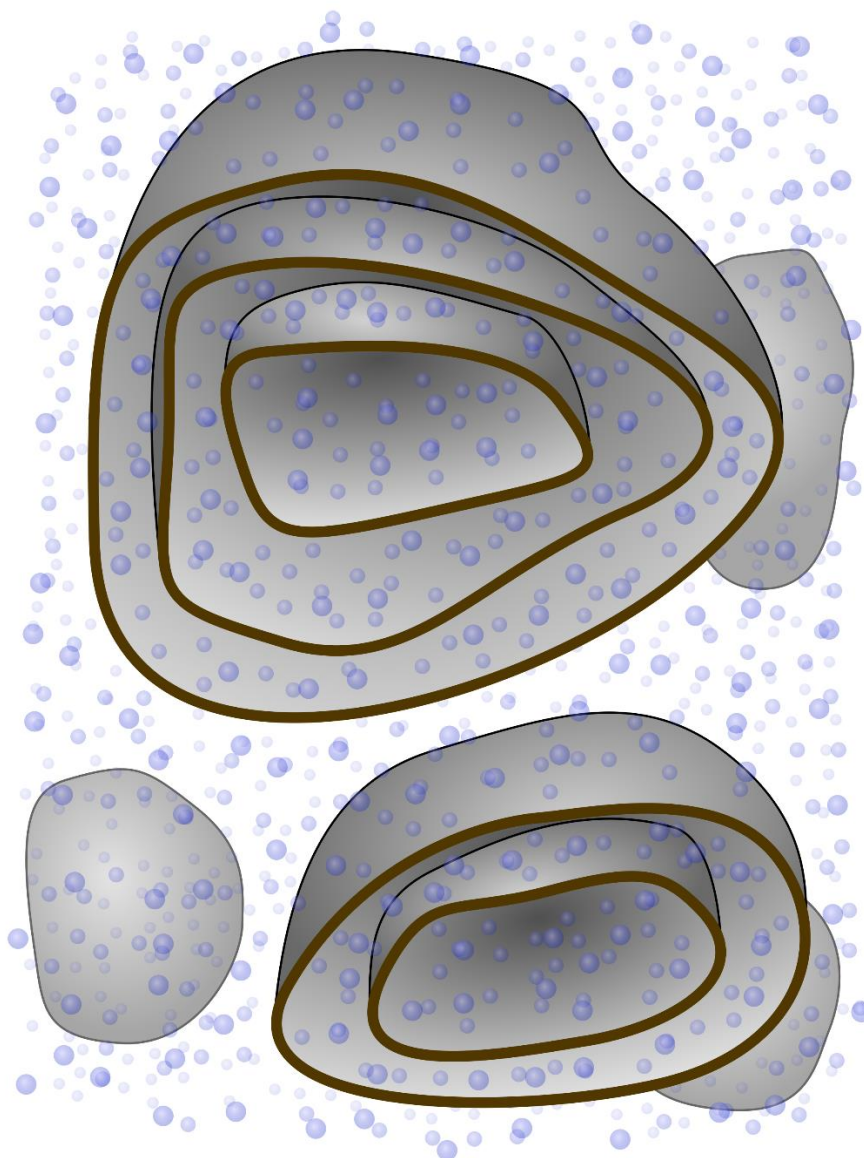
Figure 1.1: A depiction of lipid bilayers in the multi-lamellar vesicle arrangement (MLV) with water denoted by blue spheres.
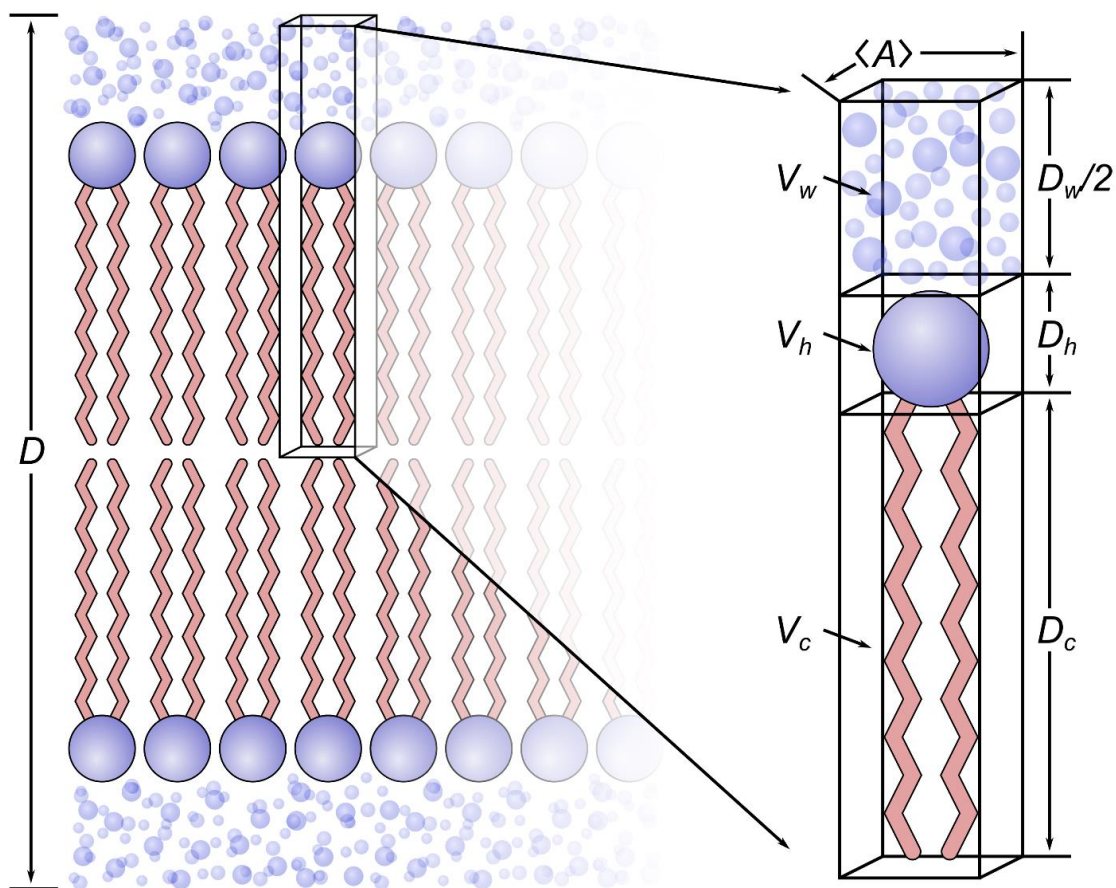
Figure 1.2: Structural parameters for a liquid-crystalline lipid membrane. Locally in the MLV phase, the bilayers repeat in stacks in intervals of the lattice repeat spacing, $D$, which can be further divided into the water spacing, $D_w$, the lipid head group spacing, $D_h$, and the lipid chain spacing, $D_c$. Given an average area per lipid, $\langle A \rangle$, these divisions have corresponding volumes of $V_w$, $V_h$, and $V_c$.
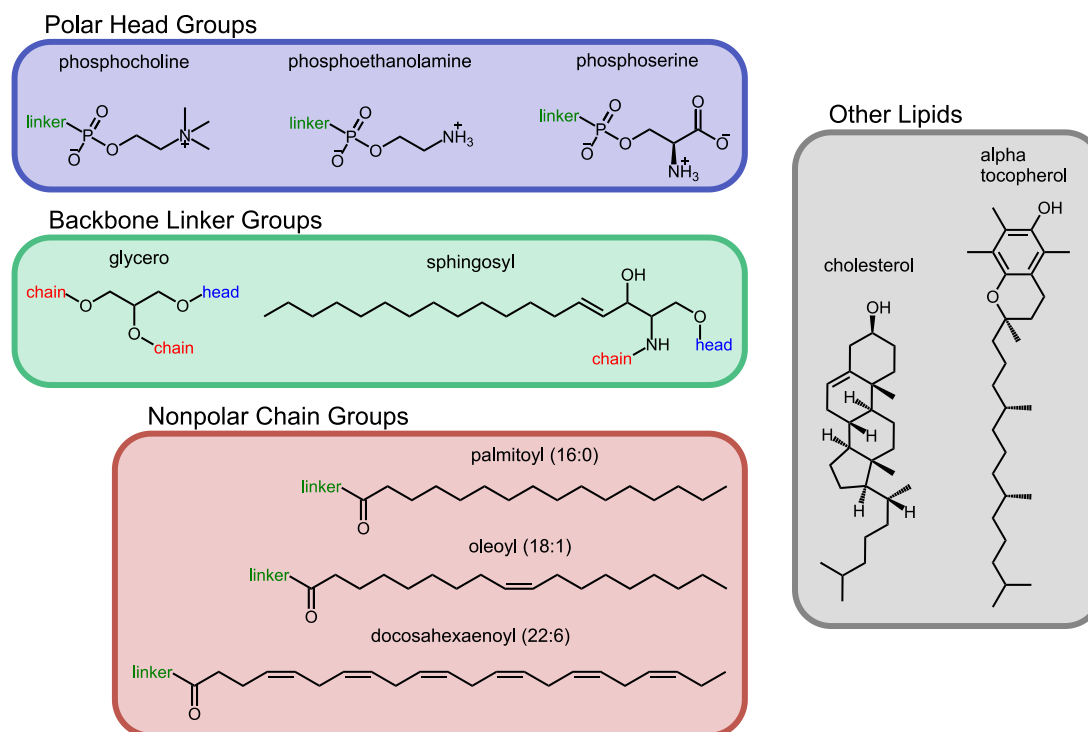
Figure 1.3: Some common chemical groups in the composition of lipids. The polar nature of phosphocholine (PC), phosphoethanolamine (PE), and phosphoserine (PS) is ubiquitous for lipid head groups (top). This is satisfied by the hydroxide group for cholesterol and vitamin E (right). The polar head groups listed are linked to hydrocarbons by a backbone group (middle). Glycerol can link two lipid chains while the sphingosine group has room for one. In general lipid chains are of various lengths and various number of double bonds as shown with the palmitoyl, oleoyl, and docosahexaenoyl chains (bottom).

# CHAPTER 2.     SOLID-STATE NUCLEAR MAGNETIC RESONANCE

## 2.1    Introduction

Solid-state nuclear magnetic resonance (NMR) has found wide application in many scientific fields where interactions in condensed matter must be considered. Such research areas range from determination of molecular structure and dynamics of crystals (Pake, 1948)  and powders (Kinnun, Leftin, & Brown, 2013) as well as studying living systems (Pius, Morrow, & Booth, 2012). As this technique observes the nuclei of atoms it is relatively biologically non-invasive. This allows NMR to be particularly useful in studying biological membranes. The application of solid state $^2$H NMR spectroscopy to study the molecular organization in lipid bilayers was the focus of this research. Here the chief features of the theory will be summarized.

Many nuclei have angular momentum which is called spin which can be manipulated using a magnetic field. Here, I will use NMR notation for the angular momentum operators (where an operator is denoted by a hat), which correspond to the traditional operators in this sense: $\hat{I}_Z = \hat{J}_Z/\hbar$ and $\hat{I}^2 = \hat{J}^2/\hbar^2$, where $\hbar = h/2\pi$ and $h$ is Planck's constant (Levitt, 2008). An atom such as hydrogen, which has only one proton, has a total nuclear spin quantum number of $I = 1/2$. If I consider the deuterium nucleus, which has one proton and one neutron, the total spin quantum number ($I = 1/2 + 1/2$) is 1.  Each of these angular momentum quantum numbers corresponds to a degeneracy of states described by the magnetic quantum number $m$. According to basic principles of quantum mechanics, the values of the projection quantum number,  $m$, range from $-I$ to $I$ in integer steps. For example, nuclei with a spin $I$ of 1/2 have $m$ values of –1/2 and 1/2, and nuclei with spin of 1 have three values of $m = -1$, 0, and 1.  This degeneracy of states can be lifted when a static magnetic field ($\boldsymbol{B_0}$) is applied to the spin system resulting in ($2I$ +1) non-degenerate states, as shown in Figure 2.1 for a spin-one nucleus.  This is the Zeeman effect.

The utility of NMR spectroscopy arises from the characteristic frequency of the quantized energy transitions between the nuclear spin states of the sample. I will use the Schrödinger equation to solve for the Zeeman energy eigenstates:

$$\hat{H}_Z|I,m\rangle = E_m|I,m\rangle \qquad (2.1)$$

where the spin wave function is designated as $|I,m\rangle$. The Zeeman Hamiltonian is proportional to the spin angular momentum operator (Griffiths, 2005):

$$\hat{H}_Z = -\gamma B_0 \hat{I}_z = \omega_0 \hat{I}_z \qquad (2.2).$$

Here $\omega_0 = 2\pi\nu_0$ is the Larmor frequency and is equal to $-\gamma B_0$, where $\gamma$ is the gyromagnetic ratio. The gyromagnetic ratio is the nuclear magnetic moment divided by its angular momentum ($\gamma = |\vec{\mu}|/|\vec{J}|$). In NMR it reveals how much angular momentum can be generated given an amount of magnetic field.

To solve this eigenvalue problem, the angular momentum eigenvalue relations will be used (Griffiths, 2005), as shown in equations 2.3 and 2.4:

$$\hat{I}_z|I,m\rangle = m|I,m\rangle \qquad (2.3)$$

and

$$\hat{I}^2|I,m\rangle = I(I+1)|I,m\rangle \qquad (2.4).$$

The solution to the eigenvalue problem in equation 2.2, with substitution of equation 2.3:

$$E_m = -\gamma\hbar B_0 m = m\hbar\omega_0 \qquad (2.5)$$

where $E_m$ are the Zeeman energy eigenvalues.

Transitions between spin energy states (see Figure 2.2) are observed in NMR spectroscopy, and for this the radiofrequency of the electromagnetic radiation that is absorbed within the spin system must be determined. The Bohr frequency condition (Griffiths, 2005) equates the frequency of the transition to the energy gap between adjacent levels (for single quantum transitions):

$$h\nu = \Delta E = E_{m+1} - E_m \qquad (2.6).$$

By combining equations 2.5 and 2.6, the frequency for the transition corresponding to the Zeeman effect is found to be:

$$\nu_0 = \frac{\omega_0}{2\pi} = -\frac{\gamma B_0}{2\pi} \qquad (2.7)$$

where $\nu_0$ is Larmor frequency, which is observed directly in NMR spectroscopy. The Larmor frequency itself gives us information on nuclear precession while deviations from it gives us more information about molecular interactions in the sample. Interactions of the nucleus with field gradients result in such deviations and provide further information of the electromagnetic environment at the nucleus. This can be used to determine molecular structure and dynamics.

## 2.2    Field Gradient Interactions

Electric and magnetic field gradients are the result of spatially varying fields, which can be described as the curvature of a potential surface. Dipolar nuclei may interact with a magnetic field gradient generated by another dipolar nucleus (dipolar coupling). While quadrupolar nuclei may interact with the electric field gradient due to the distribution of electrons around them (quadrupolar coupling).

To account for the nuclear coupling to field gradients, a perturbing tensor interaction Hamiltonian ($\widehat{H}_\lambda$) is added to the Zeeman Hamiltonian (see Figure 2.2).

$$\widehat{H} = \widehat{H}_Z + \widehat{H}_\lambda \tag{2.8}$$

Here $\lambda$ designates whether the dipolar coupling ($\lambda = D$) or quadrupolar coupling ($\lambda = Q$) is being considered. Note that $\widehat{H}_\lambda$ is a perturbing term, so the main magnetic field interaction should be much greater than the field gradient interaction (high-field limit). In NMR spectroscopy this is typically achieved with superconducting magnets (electromagnets may be sufficient as well (Klein, 1990)). Since field gradients can vary in three dimensions, they are represented as a field gradient tensor $V$ (as shown in Figure 2.3). In general, the coupling Hamiltonian can be written as the dot product of the angular momentum tensor ($\widehat{T}$) with the field gradient tensor ($V$) together with a coupling constant $C_\lambda$ (Spiess & Steigel, 1978).

$$\widehat{H}_\lambda = \hbar C_\lambda \widehat{T} \cdot V \tag{2.9}$$

For a spin-one interaction, the dipolar coupling parameter is $C_D = -2\gamma_I\gamma_S\hbar$, and the quadrupolar coupling parameter is $C_Q = eQ/2\hbar$. Here $\gamma_I$ and $\gamma_S$ are the two magnetogyric ratios for the coupling nuclei (we denote their spins as $\hat{I}$ and $\hat{S}$ respectively), $Q$ is the

quadrupole moment, and $e$ is the elementary charge. Such spin-one interactions may be two spin-one-half nuclei in dipolar coupling or a spin-one nucleus in quadrupolar coupling. The form of the angular momentum tensor and field gradient tensor varies, depending on whether the Cartesian or spherical basis is considered. Each has its benefits and I will discuss both.

## 2.3    Cartesian Basis

In the Cartesian basis, the elements of the angular momentum tensor are as follows:

$$\hat{T}_{jk} = \tfrac{3}{2}\big(\hat{I}_j \hat{S}_k + \hat{I}_k \hat{S}_j\big) - \delta_{jk}\hat{\boldsymbol{I}} \cdot \hat{\boldsymbol{S}} \tag{2.10}$$

were the indices $j$ and $k$ are the Cartesian directions of $x$, $y$, and $z$ (thus $\hat{\boldsymbol{T}}$ is a three-by-three matrix) (Spiess & Steigel, 1978). In equation 2.10, the angular momentum operators of the interacting nuclei are respectively written as $\hat{I}$ and $\hat{S}$. In the case of quadrupolar coupling, where coupling is due to electric field gradients, $\hat{I} = \hat{S}$.

The principal axis system (PAS) is defined as the coordinate system in which the field gradient tensor is diagonal. For deuterium bonded to carbon, the $z$-axis of this coordinate system is parallel to the carbon-deuterium bond vector. This is different from the laboratory frame (LAB), which is defined by the direction of the main magnetic field. To relate the principal axis system to the laboratory frame requires a similarity transform, however as shown later closure may be used in the spherical basis to simplify the transformation. The field gradient tensor in the principal axis system has the diagonal form,

$$\boldsymbol{V}^{\mathrm{PAS}} = \begin{pmatrix} V_{xx}^{\mathrm{PAS}} & 0 & 0 \\ 0 & V_{yy}^{\mathrm{PAS}} & 0 \\ 0 & 0 & V_{zz}^{\mathrm{PAS}} \end{pmatrix} \tag{2.11}$$

Here the convention that $\left|V_{zz}^{\mathrm{PAS}}\right| \geq \left|V_{yy}^{\mathrm{PAS}}\right| \geq \left|V_{xx}^{\mathrm{PAS}}\right|$ is used (Abragam, 1961). Note that the $V_{ii}^{\mathrm{PAS}}$ components of the tensor are not electric or magnetic potentials, but second derivatives of the potential ($V_{ij} = \partial^2 \phi / \partial x_i \partial x_j$ where $\phi$ is the potential). Thus they are components of the electric field gradient.

Since the field gradients are produced by charges and nuclei external to the observed nucleus, regardless of the reference frame, the Laplace equation holds:

$$\sum_i V_{ii} = V_{xx} + V_{yy} + V_{zz} = 0 \tag{2.12}.$$

We observe the interaction in the laboratory frame, thus we only observe the field gradients as they appear in the laboratory frame as depicted in Figure 2.3. With equations 13, 14, and 15, the Hamiltonian for the quadrupolar interaction in the laboratory frame is expressed below:

$$\hat{H}_\lambda = \hbar C_\lambda \left[ V_{xx}^{LAB}\left(3\hat{I}_x\hat{S}_x - \hat{I}\cdot\hat{S}\right) + V_{yy}^{LAB}\left(3\hat{I}_y\hat{S}_y - \hat{I}\cdot\hat{S}\right) + V_{zz}^{LAB}\left(3\hat{I}_z\hat{S}_z - \hat{I}\cdot\hat{S}\right) \right] \tag{2.13}.$$

In order for this Hamiltonian to be a perturbation of the Zeeman effect (high magnetic field limit) it must commute with the Zeeman Hamiltonian (secular). This allows the application of the eigenvalue relations and the Laplace equation to equations 2.8, 2.2, and 2.13 to find the energy eigenvalues in the laboratory frame:

$$E_m = -\gamma \hbar B_0 m + \frac{3}{2}\hbar C_\lambda V_{zz}^{LAB} m^2 \tag{2.14}.$$

The differences between the energy states give rise to the observable transition frequencies. In the case of a quadrupolar spin-1 interaction, there are two transitions as shown in equations 2.15 and 2.16 and in Figure 2.2.

$$\nu_Q^+ = \frac{(E_{-1} - E_0)}{h} \tag{2.15}$$

$$\nu_Q^- = \frac{(E_0 - E_{+1})}{h} \tag{2.16}$$

After inserting the energy eigenvalues, the resulting transition frequencies for a spin-1 interaction are as follows:

$$\nu_Q^\pm = \pm \frac{3}{4\pi} C_\lambda V_{zz}^{LAB} \tag{2.17}$$

where the $\pm$ notation corresponds to the two transitions in equations 19 and 20. These frequency transitions are what are observed in $^2$H NMR spectra (Kinnun et al., 2013) centered about the Larmor frequency. Remember that the field gradients observed are in the laboratory frame, and not in the principal axis system. If the principle axis system happens to be rotated to match the laboratory frame, only then the field gradient terms may be equivalent. The strength of the Cartesian basis is its simple correspondence between experimental observables to fundamental interactions. However, it is not always simple to

relate the laboratory frame interactions to the principal axis system frame interactions. This task is simpler with a transformation to the spherical basis.

## 2.4 Spherical Basis

In the spherical basis, also known as the irreducible representation (Spiess & Steigel, 1978), the tensors can be rewritten with Table 2.1. With equation 2.8 and Table 2.1, the tensor interaction Hamiltonian is re-written as:

$$\hat{H}_\lambda = \frac{\hbar C_\lambda}{2}\left[\frac{V_0^{(2)\mathrm{LAB}}}{\sqrt{6}}\left(3\hat{I}_z\hat{S}_z - \hat{\boldsymbol{I}}\cdot\hat{\boldsymbol{S}}\right) + \frac{1}{2}\left(V_{-2}^{(2)\mathrm{LAB}}\hat{I}_-\hat{S}_- + V_{+2}^{(2)\mathrm{LAB}}\hat{I}_+\hat{S}_+\right)\right] \qquad (2.18)$$

where

$$\hat{I}_\pm|I,m\rangle = \sqrt{(I\mp m)(I\pm m + 1)}|I,m\rangle \qquad (2.19).$$

Here $\hat{I}_\pm$ and $\hat{S}_\pm$ are the raising and lowering operators for the respective nuclei (where $\hat{S}_\pm$ has the same corresponding relation as equation 23), and $V_m^{(2)}$ are the irreducible components of the field gradient tensor.

In the spherical coordinate system, the field gradient tensor in the principal axis system can be transformed to the laboratory frame using the Wigner rotation matrix elements $D_{sm}^{(2)}(\Omega_{PL})$ shown in Table 2.1 via the relation:

$$V_m^{(2)\mathrm{LAB}} = \sum_{s=-2}^{2} V_s^{(2)\mathrm{PAS}} D_{sm}^{(2)}(\Omega_{PL}) \qquad (2.20)$$

Here $\Omega_{PL}$ are the Euler angles ($\alpha$, $\beta$, and $\gamma$) and *PL* indicates a transformation from the principal axis system to the laboratory frame. These Euler angles represent rotations in three dimensions and allow the determination of the projection of the principal axis system to the laboratory frame (shown in Figure 2.4).

The advantage of using Wigner rotation matrix elements is that they obey a property called closure as they are a part of the special orthogonal group in three dimensions, SO(3) (Brown, 1996). Just as two rotations of 45° can achieve a 90° rotation, with successive rotations via Wigner rotation matrix elements can rotate through different intermediate

frames. As an example, the rotation from the principal axis system ($P$) to the laboratory frame ($L$) can be separated with an intermediate frame ($I$) using the equation below:

$$D_{sm}^{(2)}(\Omega_{PL}) = \sum_r D_{sr}^{(2)}(\Omega_{PI})D_{rm}^{(2)}(\Omega_{IL}) \tag{2.21}.$$

If needed, rotation could have been further expanded to include a sequence of intermediate frames. The only condition that must be obeyed is that all of these frames must sequentially transform from the initial frame (PAS) to the final frame (designated LAB), thus closure.

Due to the strong external magnetic field ($\mathbf{B_0}$) the corresponding $V_0^{(2)\text{LAB}}$ component of the field gradient tensor is the only one observed in the NMR experiment. By using equation 2.21, this component of the laboratory field gradient tensor can be decomposed in terms of the principal axis system field gradient tensor elements:

$$V_0^{(2)\text{LAB}} = V_{-2}^{(2)\text{PAS}}D_{-20}^{(2)}(\Omega_{PL}) + V_0^{(2)\text{PAS}}D_{00}^{(2)}(\Omega_{PL}) + V_{+2}^{(2)\text{PAS}}D_{+20}^{(2)}(\Omega_{PL}) \tag{2.22}.$$

Taking into consideration that only the $V_0^{(2)\text{LAB}}$ component is observed in strong magnetic fields, the secular part (commutes with the Zeeman Hamiltonian) of the tensor interaction Hamiltonian (equation 2.18) can be written with help of table 2.1 as:

$$\hat{H}_\lambda = \tfrac{1}{2}\hbar C_\lambda \delta_\lambda^{\text{PAS}}\left(3\hat{I}_z\hat{S}_z - \hat{\boldsymbol{I}}\cdot\hat{\boldsymbol{S}}\right)\left[D_{00}^{(2)}(\Omega_{PL}) - \frac{\eta_\lambda^{\text{PAS}}}{\sqrt{6}}\left(D_{-20}^{(2)}(\Omega_{PL}) + D_{20}^{(2)}(\Omega_{PL})\right)\right] \tag{2.23}.$$

Where $\delta_\lambda^{\text{PAS}} = V_{zz}^{\text{PAS}}$ is the largest eigenvalue of the electric field gradient and $\eta_\lambda^{\text{PAS}} = \left(V_{yy}^{\text{PAS}} - V_{xx}^{\text{PAS}}\right)/V_{zz}^{\text{PAS}}$ is the asymmetry parameter in the principal axis system. Assuming a spin-one quadrupolar nucleus such as deuterium, the frequency transitions (with equations 2.15 and 2.16) can be solved for:

$$\nu_Q^\pm = \pm\frac{3C_\lambda\delta_\lambda^{\text{PAS}}}{4\pi}\left[D_{00}^{(2)}(\Omega_{PL}) - \frac{\eta_\lambda^{\text{PAS}}}{\sqrt{6}}\left(D_{-20}^{(2)}(\Omega_{PL}) + D_{+20}^{(2)}(\Omega_{PL})\right)\right] \tag{2.24}.$$

After substituting the Wigner rotation matrix elements from Table 2.1, equation 2.24 becomes:

$$\nu_Q^\pm = \pm\frac{3C_\lambda\delta_\lambda^{\text{PAS}}}{4\pi}\left[\tfrac{1}{2}(3\cos^2\beta_{PL} - 1) - \frac{\eta_\lambda^{\text{PAS}}}{2}\left(\cos(2\alpha_{PL})\sin^2(\beta_{PL})\right)\right] \tag{2.25}$$

which gives a frequency splitting, $\Delta\nu_Q = \nu_Q^+ - \nu_Q^-$, of:

$$\Delta\nu_Q = \frac{3C_\lambda\delta_\lambda^{\text{PAS}}}{2\pi}\left[\tfrac{1}{2}(3\cos^2\beta_{PL} - 1) - \frac{\eta_\lambda^{\text{PAS}}}{2}\left(\cos(2\alpha_{PL})\sin^2(\beta_{PL})\right)\right] \tag{2.26}.$$

By using spherical coordinates in the irreducible representation, the observed transitions in the laboratory frame can be directly related to the field gradients in the principal axis system. This will be important when discussing orientational dependence of NMR spectra and motional averaging.

## 2.5    Static Line Shapes

The orientation of the external magnetic field in respect to the sample gives the direction of quantization of the quadrupolar nucleus. To illustrate how this orientation is observed in an NMR line shape, consider a single homogeneous crystal of perfectly aligned molecules (and thus the interaction is aligned as well). If the magnetic field is parallel to the *z*-direction of the principal axis system, then the *z*-direction field gradient component, $V_{zz}^{PAS}$, is observed ($V_{zz}^{LAB} = V_{zz}^{PAS}$) as directly shown in Figure 2.5a. Likewise for the *x*- and *y*-orientations where the $V_{xx}^{PAS}$ or $V_{yy}^{PAS}$ components of the electric field gradient respectively ($V_{zz}^{LAB} = V_{xx}^{PAS}$ or $V_{yy}^{PAS}$) would be observed (see Figure 2.5b,c). This allows NMR spectroscopy to detect molecular-scale interactions by rotating the material we are interested in within the magnetic field.  Remember for deuterium bonded to carbon, the largest field gradient in the principal axis system ($V_{zz}^{PAS}$) is along the carbon-deuterium bond.

The NMR line shape of a randomly-oriented powder has contributions from all orientations, as shown in Figure 2.5e and f. The frequency splitting of a powder spectrum is given by the components of the electric field gradient, while the amplitude is given by the density of states for each orientation. First note that from the equation 16 (the Laplace equation), the sum of $V_{xx}^{PAS}$ and $V_{yy}^{PAS}$ components of the electric field gradient must be of opposite sign of $V_{zz}^{PAS}$:

$$V_{zz} = -\left(V_{xx} + V_{yy}\right) \tag{2.27}.$$

A general rule of thumb is the stronger the interaction, the less number of orientations that correspond to it, and thus the weaker the signal, which will be more obvious in the spherical basis (see Figure 2.6e and f). So the $V_{zz}^{PAS}$ component of the spectrum will have the greatest deviation from the Larmor frequency, and also will be the smallest in amplitude. The next

largest frequency component will be the $V_{yy}^{\text{PAS}}$ field gradient component, and it will be slightly greater amplitude. The smallest frequency component, but the largest amplitude, will be the $V_{xx}^{\text{PAS}}$ component. Finally recall from equations 2.17 and 2.25, that spin-one nuclei have two transitions of opposite sign, and thus will show two branches of the spectrum superimposed. Importantly, with powders all components of the field gradient are simultaneously observed. See Figure 2.5e for the complete line shape.

The spherical basis has an advantage in determining frequency components off the principal axes without difficult similarity transforms. When the principal axis system is parallel with the main magnetic field, $\beta_{PL} = 0°$, the $V_{zz}^{\text{PAS}}$ component of the field gradient is observed. Furthermore, when the principal axis system is perpendicular to the main magnetic field, $\beta_{PL} = 90°$, either the $V_{xx}^{\text{PAS}}$ component of the field gradient is observed when $\alpha_{PL} = 0°$, or the $V_{yy}^{\text{PAS}}$ component when $\alpha_{PL} = 90°$. If the principal axis system is rotated by arbitrary angles, then we can simply insert the angles into equation 29 to find the resulting frequency components.

To simplify our lineshape calculations of randomly oriented powders, axial symmetry about the $z$-axis in the principal axis system will be assumed. This situation applies approximately to the C-$^2$H bond vector and is attained by molecules undergoing fast axial rotation, which is often the case for lipids in the liquid disordered phase. The case of an axially symmetric field gradients requires:

$$V_{xx}^{\text{PAS}} = V_{yy}^{\text{PAS}} \tag{2.28}$$

which from Table 2.1 implies

$$\eta_\lambda^{\text{PAS}} = 0 \tag{2.29}.$$

With use of equations 31, 32 and Table 2.1, I obtain the property:

$$V_{zz}^{PAS} = -2V_{xx}^{PAS} = -2V_{yy}^{PAS} = \delta_\lambda \tag{2.30}.$$

Given equations 2.25 and 2.29 with Table 2.1, spin-one frequency transitions simplify to:

$$\nu_Q^\pm = \frac{\Delta^\pm}{2}(3\cos^2\beta_{PL} - 1) \tag{2.31}$$

where

$$\Delta^\pm = \pm \left(\frac{3}{8\pi}\right) C_Q \delta_Q^{\text{PAS}} \qquad (2.32).$$

To generate a lineshape, the angular distribution of a power must be mapped to a frequency distribution. In a randomly-oriented powder, the density over all Euler angles is constant. Given a lineshape function $f(\nu)$, the area under the curve between two frequencies, $\nu_a$ and $\nu_b$, is proportional to the density summed over the corresponding angles, $\beta_a$ and $\alpha_a$ to $\beta_b$ and $\alpha_b$. Note that the range of frequencies observed for these transitions given any $\alpha$ and $\beta$ is limited by equation 2.25. Furthermore, since the density of states is constant in respect to the Euler angles due to random distribution of orientations; summation can be pulled out and designated as $C$ (with other conversion factors included). Putting this into an integral form gives (Häberlen, 1976):

$$\int_{\nu_a}^{\nu_b} f(\nu)d\nu = C \int_{\alpha_a}^{\alpha_b} \int_{\beta_a}^{\beta_b} \sin\beta d\beta \, d\alpha \qquad (2.33).$$

Due to axial symmetry, the integral over the $\alpha$ angle is a constant, and may be simply absorbed into $C$. By using equation 2.31, $\sin\beta$ in terms of $\nu$ can be determined by taking a derivative with respect to the angle, which the result in integral form is:

$$\int_{\beta_a}^{\beta_b} \sin\beta d\beta = \int_{\nu_a}^{\nu_b} \frac{1}{\sqrt{3}\Delta^+} \frac{d\nu}{\sqrt{\frac{2\nu_Q^+}{\Delta^+} + 1}} \qquad (2.34).$$

Note that this integral is applicable to both transitions, despite only the positive transition being shown. This is due to the fact that the negative sign in the negative transition is cancelled. The limits of $\nu_a$ to $\nu_a$ are determined by the limits of equation 2.31 and will be further elaborated upon. Because of this $\nu = \nu_Q^+$ effectively. Inserting equation 2.34 into 2.33, given the $\alpha$ dependence is absorbed into $C$, yields:

$$\int_{\nu_a}^{\nu_b} f(\nu)d\nu = C \int_{\nu_a}^{\nu_b} \frac{1}{\sqrt{3}\Delta^+} \frac{d\nu}{\sqrt{\frac{2\nu_Q^+}{\Delta^+} + 1}} \qquad (2.35)$$

where recognizing $\nu = \nu_Q^+$, this implies

$$f(\nu) = \frac{1}{\sqrt{3}\Delta^+} \frac{d\nu}{\sqrt{\frac{2\nu_Q^+}{\Delta^+} + 1}} \qquad (2.36)$$

and given equation 2.31, this can be written in terms of the angle $\beta$ to be

$$f(\beta) = \frac{C}{3\Delta^+} \frac{1}{|\cos\beta|}$$ 

(2.37).

This determines the lineshape for all orientations, $\beta$, as shown in Figure 2.6a. Looking at the perpendicular components of the spectrum, where $\beta = 90°$ and $v_Q^{\pm} = -\Delta^{\pm}/2$, which is the lower limit ($v_a$) for $v_Q^+$ and the upper limit ($v_b$) for $v_Q^-$, the line shape becomes a singularity. This can be understood by imagining the Earth. The equator can theoretically correspond to infinitely many places; thus the number of states becomes infinite. Now at the North Pole, there is only one spot where we could achieve this positioning, and there is only one state. This corresponds to the Euler angle of $\beta = 0°$ with $v_Q^{\pm} = \Delta^{\pm}$ and according to equations 2.36 and 2.37 this should be the weakest part of the signal amplitude given that it is the upper frequency limit ($v_b$) for $v_Q^+$ and the lower limit ($v_a$) for $v_Q^-$. Practically samples have a finite number of nuclei thus there is not infinitely many states at the equator.

## 2.6    Motional Averaging

$^2$H NMR spectroscopy can be sensitive to the structure and orientation of molecules, but the motions of molecules result in motionally averaged field gradients (if occurring near or faster than the static coupling constant). Understanding of these dynamics is of great importance within condensed matter physics and biophysics, especially in the case of biological membranes which have a static and dynamic properties.

To distinguish between rotations of the entire sample, and motions within the molecular system, the molecular frame is introduced. The field gradients in this frame are labeled as $V_{xx}^{MOL}$, $V_{yy}^{MOL}$, and $V_{yy}^{MOL}$. In between the principal axis and the molecular frame, fast motions occur which results in motional averaging; while between the molecular frame and the laboratory frame molecular orientations result in powder patterns. In general, motional averaging can reduce the magnitude of $v_Q^{\pm}$, the fraction of which defines an order parameter, $S$. For axially symmetric tensor interactions ($V_{xx} = V_{yy}$), as shown in Figure 2.6a, the order parameter in the Cartesian basis is defined as:

$$S_{PM} \equiv \frac{\langle V_{zz}^{MOL} \rangle}{V_{zz}^{PAS}} \qquad (2.38).$$

where $\langle V_{zz}^{MOL} \rangle$ is the observed residual field gradient which is reduced due to molecular motion. This is compared to the static field gradient interaction of $V_{zz}^{PAS}$. In the most general cases, for static powders the maximum value of the order parameter is 1, unless all of the molecules are fixed to a particular orientation such as in a crystal.

As an initial example, consider a case of a molecule randomly tumbling in all directions (isotropic) such as the behavior of liquids. Effectively all of the electric field components are motionally averaged, which requires:

$$\langle V_{xx}^{MOL} \rangle = \langle V_{yy}^{MOL} \rangle = \langle V_{zz}^{MOL} \rangle \qquad (2.39).$$

Here the angular brackets $\langle \ \rangle$ indicate averaging over time. Remember from the Laplace equation (equation 2.12) requires that the $x$- and $y$-components must be opposite in sign to the $z$-component, yet equation 2.39 requires all components to be the same. There is only one solution that satisfies these conditions:

$$\langle V_{xx}^{MOL} \rangle = \langle V_{yy}^{MOL} \rangle = \langle V_{zz}^{MOL} \rangle = 0 \qquad (2.40)$$

which yields an order parameter of:

$$S_{PM} = 0 \qquad (2.41).$$

Thus none of the field gradients contribute to the NMR spectrum. This allows typical liquids NMR spectroscopy to see small shifts in main magnetic field (**B₀**) without being obfuscated by field gradient contributions.

Next consider the case of motional averaging in the $x$-$z$ plane of the principal axis system. Because of the axial symmetry condition this is also equivalent to motional averaging in the $y$-$z$ plane of the field gradient tensor. Examples of this type of motion are molecules that are isomerizing about a bond axis or about a ring. In this case, the observed $z$-component of the interaction is averaged with the $x$-component in the principal axis system. Since the $x$- and $z$-components are being averaged, the largest non-averaged component is the $y$-component of the principal axis system. By the standard convention, the largest component is defined as the $z$-component, so equation 2.12 yields:

$$\langle V_{zz}^{MOL} \rangle = V_{xx}^{PAS} = -\frac{1}{2}V_{zz}^{PAS} \qquad (2.42)$$

where according to equation 2.38, the order parameter is:

$$S_{PM} = -\frac{1}{2} \qquad (2.43).$$

Here the planar motion results in the observed frequency splitting being reduced by half as shown in Figure 2.6b.

What happens if the motion occurs at some arbitrary angle, or if there are a combination of motions? In the Cartesian basis this is a difficult task, however in the spherical basis this task is greatly simplified. Using the assumption of axial symmetry and equation 2.22, the following equation can be obtained:

$$V_0^{(2)\text{LAB}} = V_0^{(2)\text{PAS}} D_{00}^{(2)}(\Omega_{PL}) \qquad (2.44).$$

As in the Cartesian basis, it is useful to distinguish the orientation in the laboratory frame of the material and the molecular motions in the material. The property of closure (see equation 2.21) and the introduction of the molecular frame as an intermediate frame, expands equation 2.44 into:

$$V_0^{(2)\text{LAB}} = V_0^{(2)\text{PAS}} D_{00}^{(2)}(\Omega_{PM}) D_{00}^{(2)}(\Omega_{ML}) \qquad (2.45).$$

Here the Euler angles labeled *PM* are the orientation of the principal axis with respect to the molecular orientation, and likewise the Euler angles labeled *ML* are the orientation of the molecules with respect to the laboratory frame. If there are fast motions in the system, then the field gradient tensor is averaged. Now in solids, it is typically the case that the orientations of the molecules are fixed; however, there may be motion within the molecules themselves (between the principal axis and the molecular axis). This results in an averaged form of equation 2.45:

$$\langle V_0^{(2)\text{LAB}} \rangle = V_0^{(2)\text{PAS}} \langle D_{00}^{(2)}(\Omega_{PM}) \rangle D_{00}^{(2)}(\Omega_{ML}) \qquad (2.46).$$

In this formalism, molecular motions that average the field gradient tensor and molecular orientations which can result in partially-averaged powder lineshapes can be distingiushed. In terms of only the motionally averaged part, the order parameter is defined in the irreducible representation as:

$$S_{PM} \equiv \langle D_{00}^{(2)}(\Omega_{PM}) \rangle = \frac{1}{2} \langle 3\cos^2(\beta_{PM}) - 1 \rangle \qquad (2.47).$$

For deuterium labeled molecules, the corresponding order parameter is typically defined as $S_{CD} \equiv \frac{1}{2} \langle 3\cos^2(\beta) - 1 \rangle$, where it is assumed that deuterium is bonded to a carbon atom.

Here the frame of reference is typically not stated but it is assumed that the order parameter is representative of motional averaging and not a specific orientation of a powder distribution (although average orientations due diminish reported order parameters).

In condensed matter and in biophysics, the tetrahedral configuration of atoms is quite common. In this configuration, four atoms are located around a central atom angled at 109.5° from each other. It is often the case where one of the four atoms is immobilized and the other atoms can rotate about that bond—this is called free rotation. In this case, the angle between the rotating atoms and the axis of rotation (the molecular axis) is the tetrahedral angle ($\beta_{PM}$ = 109.5°). Thus the angular distribution is a sharp Dirac delta function at $\beta_{PM}$ = 109.5°. With this angle insterted into equation 2.47, the order parameter is obtained:

$$S_{PM} = \langle D_{00}^{(2)}(\beta_{PM} = 109.5°)\rangle = \tfrac{1}{2}[3\cos^2(109.5°) - 1] = -\frac{1}{3} \qquad (2.48).$$

The order parameter reveals that the frequency splitting is reduced by one-third as shown in Figure 2.6c. Importantly, this demonstrates how different molecular motions yield different motional averaging of tensors, and thus they can be distinguished in NMR measurements of condensed matter.

Interestingly additional independent motion results in an additional multiplicative order parameter. Introducing an intermediate frame, $I$, closure from equation 2.24 can be used to break up the Wigner rotation matrix element in equation 2.47 into two:

$$S_{PM} \equiv \langle D_{00}^{(2)}(\Omega_{PM})\rangle = \langle D_{00}^{(2)}(\Omega_{PI})\rangle\langle D_{00}^{(2)}(\Omega_{IM})\rangle = S_{PI}S_{IM} \qquad (2.49)$$

where $S_{PI} = \langle D_{00}^{(2)}(\Omega_{PI})\rangle$ and $S_{IM} = \langle D_{00}^{(2)}(\Omega_{IM})\rangle$. For example, if there is a methyl group undergoing rotation, from equation 2.48 the order parameter is $S_{PI} = -1/3$. But if this rotating group was also rotating in a plane, from equation 47, the order parameter is $S_{IM} = -1/2$. This yields an observed order parameter of $S_{PM} = (-1/3)(-1/2) = 1/6$ as shown in Figure 2.6d. Similar combinations of motions are seen in simple molecules (Kinnun et al., 2013) and in more-complex molecules such as lipids (Kinnun et al., 2015).

## 2.7    Multi-component Spectra

Deuterium has a quadrupolar nucleus, thus it can be a useful probe of molecular motion. It is typically a replacement for hydrogen and can be used to label multiple sites on a single molecule. Since it is chemically similar to hydrogen, only more massive, it does not perturb the molecular properties much when compared to non-deuterated analogs. This makes using deuterium as a probe for dynamics especially useful for organic thus biological systems. When multiple sites are labeled, a superposition of powder lineshapes are observed. This can produce a complicated spectrum, however there are techniques which simplify the process of analyzing multicomponent spectra.

According to the Laplace equation (equation 2.12) motional averaging reduces the frequency splitting. If there are multiple superimposed spectra, the average width of the spectrum is proportional to the average order of the system. The average width of a spectrum can be characterized in terms of moments:

$$M_n \equiv \frac{\int_{-\infty}^{\infty} |\omega|^n f(\omega) d\omega}{\int_{-\infty}^{\infty} f(\omega) d\omega} \tag{2.50}$$

where $\omega = 2\pi\nu$ and $f(\omega)$ is the total lineshape amplitude akin to equation 2.37 but potentially for multiple superimposed spectra. For the systems studied here, the first moment ($M_1$) will be the most relevant, however higher moments can be used to determine other molecular properties (J. H. Davis, 1983). In particular, lipid dynamics are indicative of lipid phases. Since lipid dynamics can modulate motional averaging of spectra, the first moment can be sensitive to phase transitions of the lipid membrane. Figure 2.7 shows the first moment plot of [$^2$H$_{31}$]-*N*-palmitoylsphingomyelin (PSM-d$_{31}$), an analog of palmitoylsphingomyelin perdeuterated along the amide linked palmitoyl chain, mixed with 1-palmitoyl-2-oleoylphosphatidylcholine (POPC), in a one-to-one mole ratio, as a function of temperature. At low temperature PSM-d$_{31}$ is in the solid ordered (gel) state, where its labeled chain segments do not undergo many isomerizations. This results in a broad lineshape with some asymmetry shown in the left inset spectrum of Figure 2.7 which was recorded at -10 °C. At around 10 °C a phase transition into the liquid disordered phase occurs as indicated by the inflection point of the first moment plot. The sample spectrum shown in the right inset of Figure 2.7 recorded at 30 °C is narrower with well-defined peaks.

This is indicative of the liquid disordered phase as the chain isomerizations result in a reduced frequency splitting and distinct motions between many of the labeled segments.

Given that the order parameter (equation 2.47) is related to the axially-symmetric lineshape (equation 2.36) via equations 2.31 and 2.47 with Table 2.1, the first moment (equation 2.50) is related to the ensemble-average order parameter (J. H. Davis, 1983):

$$M_1 = \frac{\pi}{\sqrt{3}} \chi_Q \overline{|S_{CD}|} \tag{2.51}$$

where $\overline{|S_{CD}|}$ is the ensemble-average order parameter and the quadrupolar coupling constant is $\chi_Q = C_\lambda \delta_\lambda^{\mathrm{PAS}}/\pi = 168$ kHz for deuterium bonded to carbon (Burnett & Muller, 1971). Here the average order parameter is weighed by the number of deuterons which contribute to each axially-symmetric powder pattern. As this is only valid for axially-symmetric powder patterns, it is primarily applicable to liquid disordered phases where isomerizations about C-C bonds result in reorientation of the labeled chain segments that is fast enough to produce such motional averaging.

In the liquid disordered phase, many of the methylene segments, and the terminal methyl segment, are undergoing distinct dynamics. This often allows for the determination of distinct order parameters along the acyl chain. The magnitude of the maximum theoretical value expected for the order parameter is $S_{CD} = 0.5$. This situation corresponds to a rigid chain in all-trans conformation lined up and rapidly reorienting about the membrane normal, $\mathbf{n_0}$. In the upper left of Figure 2.8 these fast motions are represented by the angle $\beta_{PD}^{(i)}$, which denotes the instantaneous angle the principal axis of the carbon-deuterium bond makes with the director of the local membrane normal $\mathbf{n_0}$, and $(i)$ refers to a specific segment of the hydrocarbon chain. Numbering begins at the carboxyl group and increases until it reaches the terminal methyl of a chain. The top right of Figure 2.8 shows the numbering for the sn-1 palmitoyl chain of POPC. If the membranes are in a multilamellar vesicle arrangement, the various angles, $\theta$, the director of the membranes, $\mathbf{n_0}$, makes with the external magnetic field, $\mathbf{B}$, result in each segment producing a powder pattern. To simplify the calculation of the order parameter, the frequency splitting in equation 2.26 for axial symmetry, with the definition of the order parameter (equation 2.47) and closure

(equation 2.24), can be written in terms of the quadrupolar coupling constant ($\chi_Q = 168$ kHz) as:

$$\Delta\nu_Q(\theta) = \frac{3}{2}\chi_Q|S_{CD}|P_2(cos\theta) \tag{2.52}$$

where $S_{CD}$ is the order parameter associated with fast motions as represented by the angle $\beta_{PD}$ and $\theta$ corresponds to a particular powder orientation with respect to the main magnetic field.

An example of the motion of individual chain segments producing a superposition of distinct powder patterns is shown for [$^2$H$_{31}$]-1-palmitoyl-2-oleoylphosphatidylcholine (POPC-d$_{31}$), an analog of POPC perdeuterated along the palmitoyl chain, in the middle of Figure 2.8 (the blue spectrum). The spectrum consists of a narrow signal with peaks at ±1 kHz, due to the disordered terminal methyl groups, and is superposed upon a broader superposition of signals, due to progressively more ordered methylene groups. A plateau region of methylene groups that are motionally similar in the upper portion of the chain is responsible for the sharp edges at ±12 kHz. Remember that each of these peaks should have a corresponding shoulder, denoting the edge of the powder pattern, at twice that frequency where the methyl shoulders can be seen at ±2 kHz. Due to the superposition of the remaining methylene segments, their shoulders are less distinct.

Due to the overlapping powder patterns it can be difficult to determine the areas under each peak and precise locations. As the peak areas are proportional to the number of deuterons represented, they are useful in determining which segment, phase, and domain they belong to. Intensive simulations can be done to fit these powder patterns; however, it is more efficient to deconvolute the powder pattern from the spectra. This technique is known under the term "dePaking" as the original lineshape is often called the Pake powder pattern (Pake, 1948). This effectively produces a spectrum as if each local membrane normal was oriented at $\theta = 0°$ with the main magnetic field. Typically, dePaking algorithms operate in the frequency domain following Fourier transformation and are computationally intensive (Sternin, Bloom, & MacKay, 1983). The speed of this process has been greatly

improved by a weighted fast Fourier transform algorithm that operates in the time domain as given by equation 2.53 (McCabe & Wassall, 1997):

$$F_0(-2\omega) = \sqrt{96\pi\omega}\,\frac{\text{FFT}\big(g(t)\sqrt{t}\big)}{[1-i]} \tag{2.53}$$

here $F_0$ is the dePaked lineshape, FFT is the fast Fourier transform process, and $g(t)$ is the original powder-pattern lineshape in the time domain (obtainable by inverse Fourier transform if needed).

An example of a dePaked lineshape produced by this algorithm is shown for POPC-d$_{31}$ in the bottom of Figure 2.8. Notice that the produced dePaked lineshape has twice the width of the angular frequency of the original spectrum. This means that the peaks it produces are primarily the result of the sharp perpendicular parts of the powder lineshape, hence the origin of the arrows between the powder lineshape and the dePaked lineshape of Figure 2.8. As equation 2.53 is technically an asymptotic approximation it can produce artifacts of low intensity at twice the frequency of any peak (McCabe & Wassall, 1997). These artifacts are visibly present in the dePaked spectrum at the bottom of Figure 2.8 at ±4 kHz, due to the methyl powder pattern. Weighted Fourier transforms, such as equation 2.53, are related to derivatives and fractional derivatives thus they are particularly sensitive to changes in slope. This is why the sharp perpendicular parts of the powder pattern are enhanced. But this also results in the edges of the powder pattern shoulders producing artifacts.

As the dePaking algorithm only deconvolves the powder lineshape that scales as $P_2(cos\theta)$, what remains is Gaussian or Lorentzian line broadened peaks (the convolution of both is a Voigtian lineshape). These peaks can be fit to determine the splitting of doublets and, thus, order parameters as shown in the top of Figure 2.9. Since the spectrum is representative of a zero-degree orientation, equation 2.52 simplifies to:

$$\Delta\nu_Q(\theta = 0°) = \frac{3}{2}\chi_Q|S_{CD}|P_2\big(cos(0)\big) = \frac{3}{2}\chi_Q|S_{CD}| \tag{2.54}$$

or

$$|S_{CD}| = \frac{2\Delta\nu_Q(\theta = 0°)}{3\chi_Q} \tag{2.55}$$

where $\Delta\nu_Q(\theta = 0°)$ is the frequency splitting between a doublet in the dePaked spectrum in the bottom of Figure 2.8 or the top of Figure 2.9. This allows for the determination of an order parameter profile, where the order parameter is plotted with respect to the segment position. The assumption made here is that the order parameters for lipid chains monotonically decrease from the carboxyl segment near the headgroup (at the polar water interface) to the terminal methyl end (Lafleur, Fine, Sternin, Cullis, & Bloom, 1989). For this reason, the plateau region (the large pair of peaks at the maximum frequency splitting) is often sliced according to area under the curve and assigned decreasing frequency splittings (based on weighted average) to determine the order parameters of the segments in this composite peak. There are some slight exceptions to this assumption (Seelig & Waespe-Sarcevic, 1978; Yasuda, Tsuchikawa, Murata, & Matsumori, 2015), however the majority of the labeled segments obey this motif. The order parameter profile constructed in this motif for POPC-d$_{31}$ is shown at the bottom of Figure 2.9. It reproduces the general shape of the profile obtained using selectively labeled POPC (Seelig & Waespe-Sarcevic, 1978), consisting of a plateau region of slowly varying order in the upper portion of the chain followed by a progressive reduction in order towards the terminal methyl. The is characteristic of phospholipid bilayers in the liquid crystalline state (Seelig, 1977; Shaikh, Kinnun, et al., 2015).

Table 2.1: The coupling and angular momentum tensors in the spherical basis correspond to the Cartesian basis with the use of the Wigner rotation matrix elements. Here $\Omega$ is the solid angle as represented by the Euler angles, $\delta_\lambda = V_{zz}^{\text{PAS}}$ is the largest eigenvalue of the electric field gradient, and $\eta_\lambda = \left(V_{yy}^{\text{PAS}} - V_{xx}^{\text{PAS}}\right)/V_{zz}^{\text{PAS}}$ is the asymmetry parameter.

| **Coupling Tensor** | **Angular Momentum Tensor** | **Wigner Rotation Matrix** |
|---|---|---|
| $V_0^{(2)\text{PAS}} = \sqrt{\frac{3}{2}} V_{zz}^{\text{PAS}} = \sqrt{\frac{3}{2}}\,\delta_\lambda$ | $\hat{T}_0^{(2)\text{LAB}} = \frac{1}{\sqrt{6}}\left(3\hat{I}_z\hat{S}_z - \hat{\boldsymbol{I}}\cdot\hat{\boldsymbol{S}}\right)$ | $D_{00}^{(2)}(\Omega) = \frac{1}{2}(3\cos^2\beta - 1)$ |
| $V_{\pm 1}^{(2)\text{PAS}} = 0$ | $\hat{T}_{\pm 1}^{(2)\text{LAB}} = \mp\frac{1}{2}\left(\hat{I}_z\hat{S}_\pm + \hat{I}_\pm\hat{S}_z\right)$ | $D_{\pm 10}^{(2)}(\Omega) = \mp e^{\mp i\alpha}\sqrt{\frac{3}{2}}\sin\beta\cos\beta$ |
| $V_{\pm 2}^{(2)\text{PAS}} = -\frac{1}{2}\left(V_{yy}^{\text{PAS}} - V_{xx}^{\text{PAS}}\right)$ $= -\frac{1}{2}\delta_\lambda\eta_\lambda$ | $\hat{T}_{\pm 2}^{(2)\text{LAB}} = \frac{1}{2}\hat{I}_\pm\hat{S}_\pm$ | $D_{\pm 20}^{(2)}(\Omega) = e^{\mp 2i\alpha}\sqrt{\frac{3}{8}}\sin^2\beta$ |
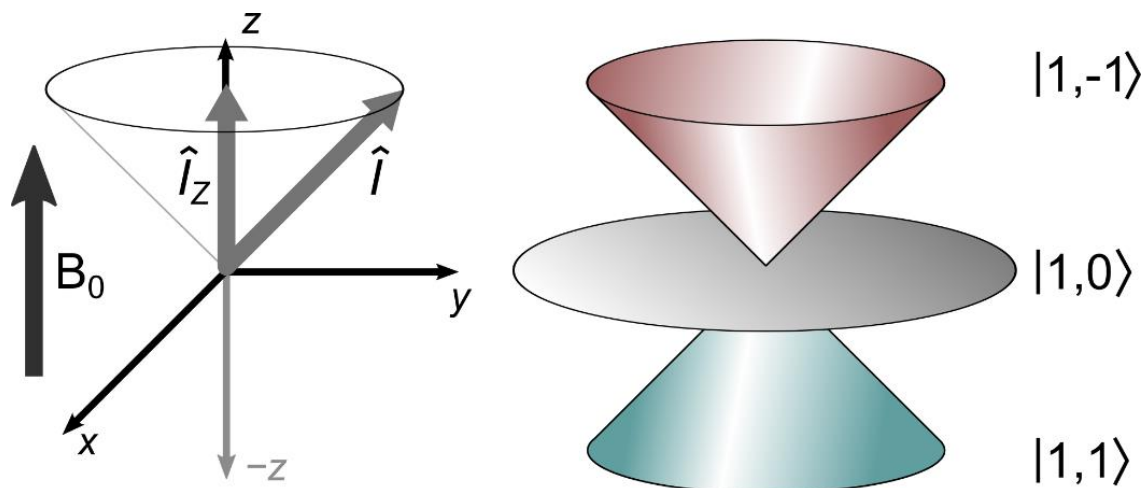
Figure 2.1: In the presence of a strong magnetic field ($\mathbf{B_0}$) the axis of quantization is along the main magnetic field direction. The nuclear spin angular momentum gives rise to a magnetic moment which interacts with the static external magnetic field (Zeeman effect). Here the main magnetic field is defined to be along the *z*-direction.
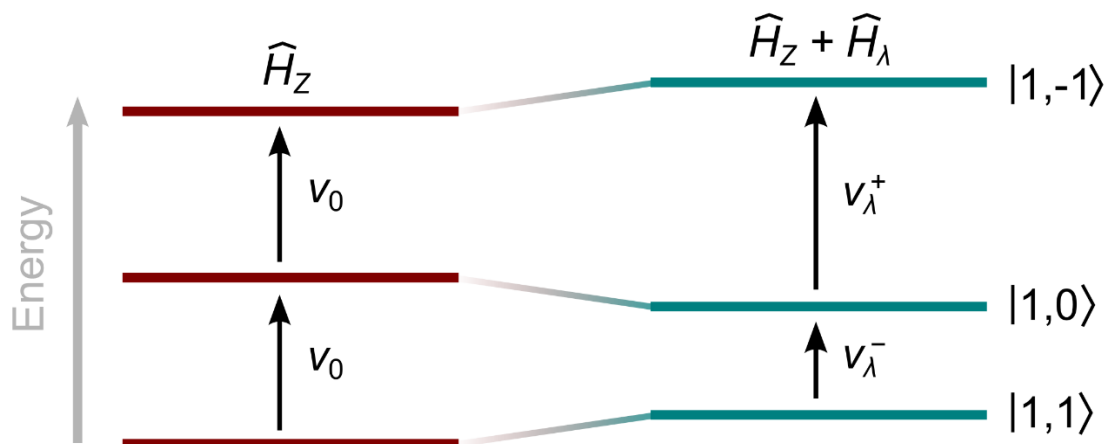
Figure 2.2: For a spin-one interaction with a magnetic field two transitions at Larmor frequencies of $v_0$ can occur. The tensor interaction Hamiltonian, $\widehat{H}_\lambda$, is a perturbation of the Zeeman Hamiltonian, $\widehat{H}_Z$, as shown in the shift of the right-side energy levels. When the tensor interaction is present, the Larmor frequency is modulated differently in each spatial direction. The presence of this perturbation results in two inequivalent transitions, $v_\lambda^-$ and $v_\lambda^+$.
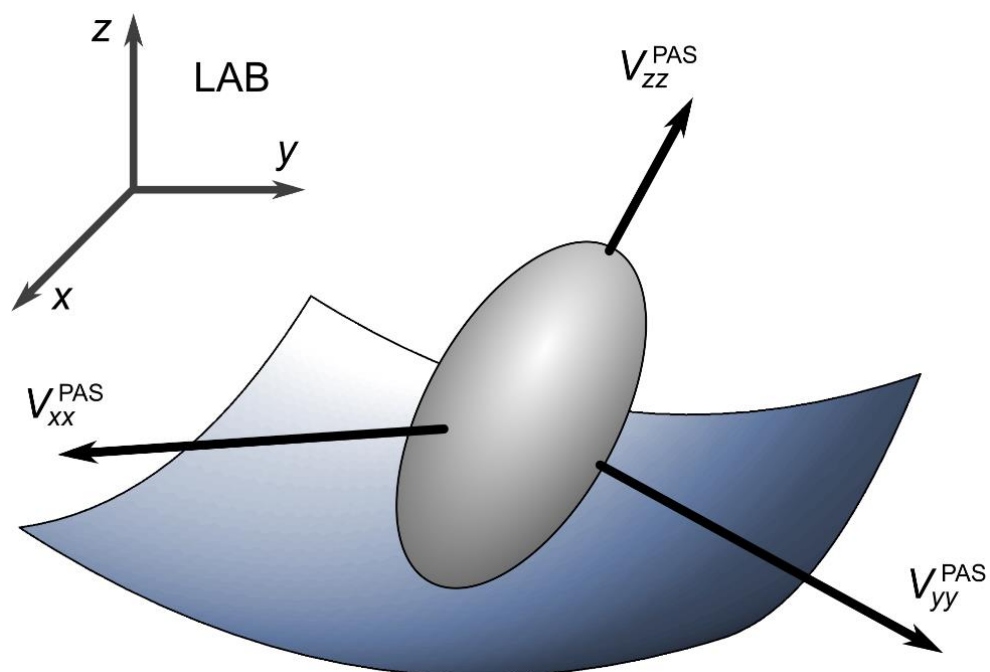
Figure 2.3: Nuclei can interact with electromagnetic field gradients within their environment. Field gradients ($V_{ii}$) are curvatures of the potential energy as represented by the blue potential surface. Mathematically these are tensor interactions and can be represented by ellipsoids (shown in grey), where the longest part of the ellipsoid represents the largest eigenvalue of the interaction. This defines a principal axis system (PAS). This principle axis system is not necessarily aligned with the lab frame (LAB). Which leads to an orientational (and motional) dependence of the observed interaction.
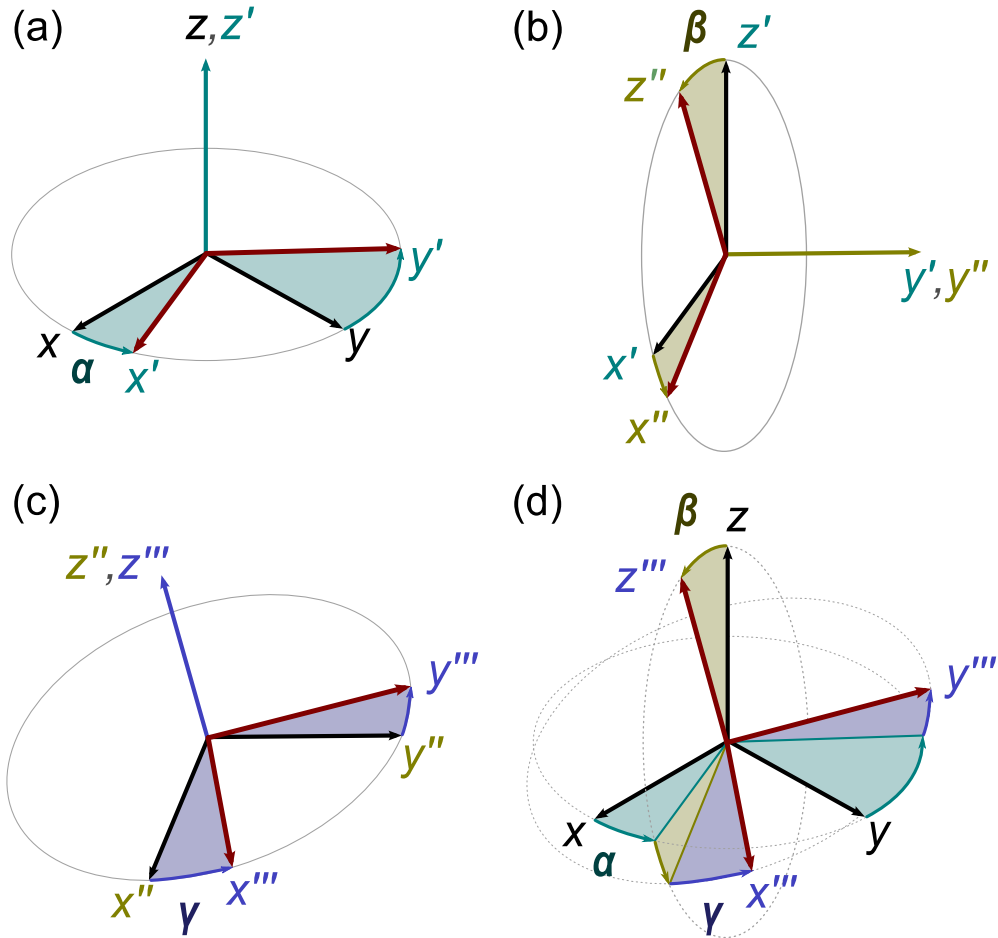
Figure 2.4: With the Euler angles the unprimed axis system can be rotated to the final triple-primed axis system for a complete 3-dimensional rotation. (a) The first Euler angle, $\alpha$, rotates the unprimed axis system about the z-axis to the prime coordinates. (b) Then, the second Euler angle, $\beta$, rotates the primed axis system about the y'-axis to the double prime coordinates. (c) Finally the last Euler angle, $\gamma$, rotates the double primed axis system about the z"-axis to the final triple primed axis system. (d) Notice that the x direction is rotated three times, the y twice, and the z once; this allows for each of the three axes to be rotated to a designated direction.
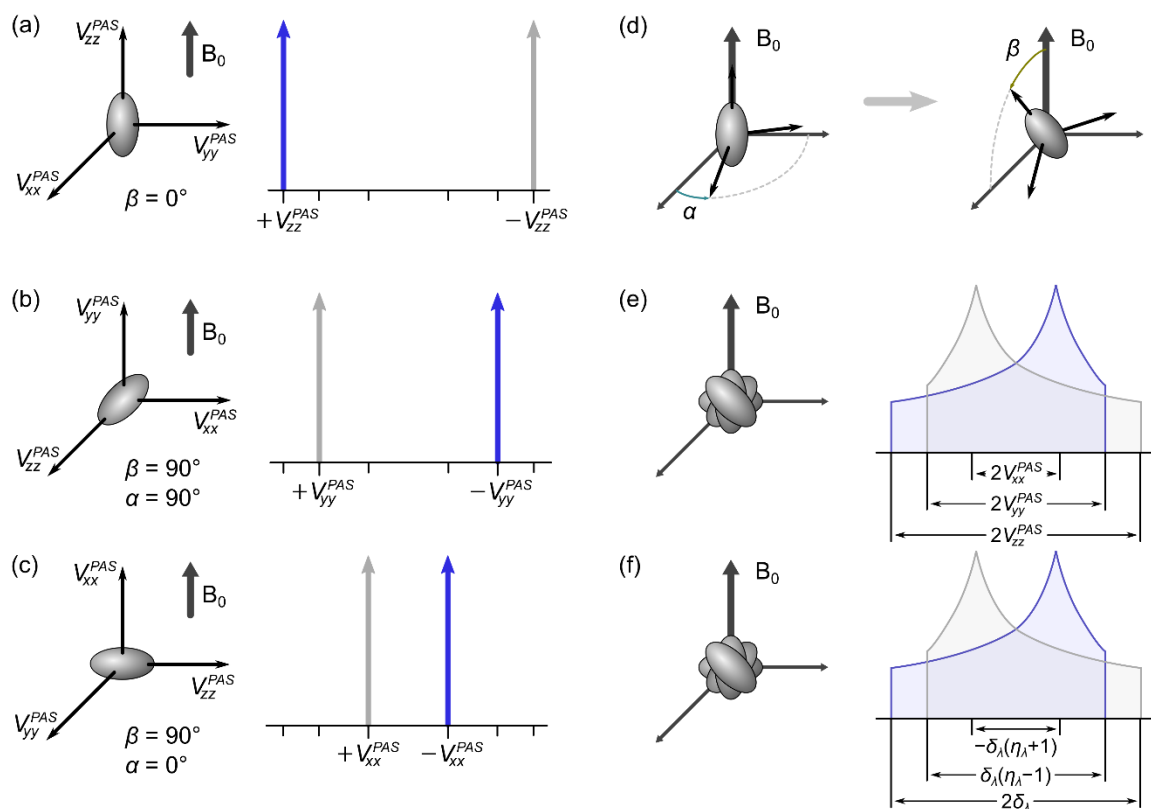
Figure 2.5: The orientation of the main magnetic field with respect to the principal axis system yields different principal components of the spectrum. If all of the nuclei are (a), (b), (c) aligned along one of the Cartesian components of the field gradient, then the frequency observed is given by the strength of the field gradient pointing in that direction, and the amplitude is given by the number of nuclei populating that state. (d) Orientations off of these axes can be handled in the irreducible representation with Euler angles $\alpha$ and $\beta$, where the corresponding angles for the Cartesian coordinates are labeled in (a), (b), and (c). If all orientations are present, such as a powder, then the entirety of the frequency distribution is observed (called a powder pattern) as shown in Cartesian coordinates in (e) and the irreducible representation in (f).
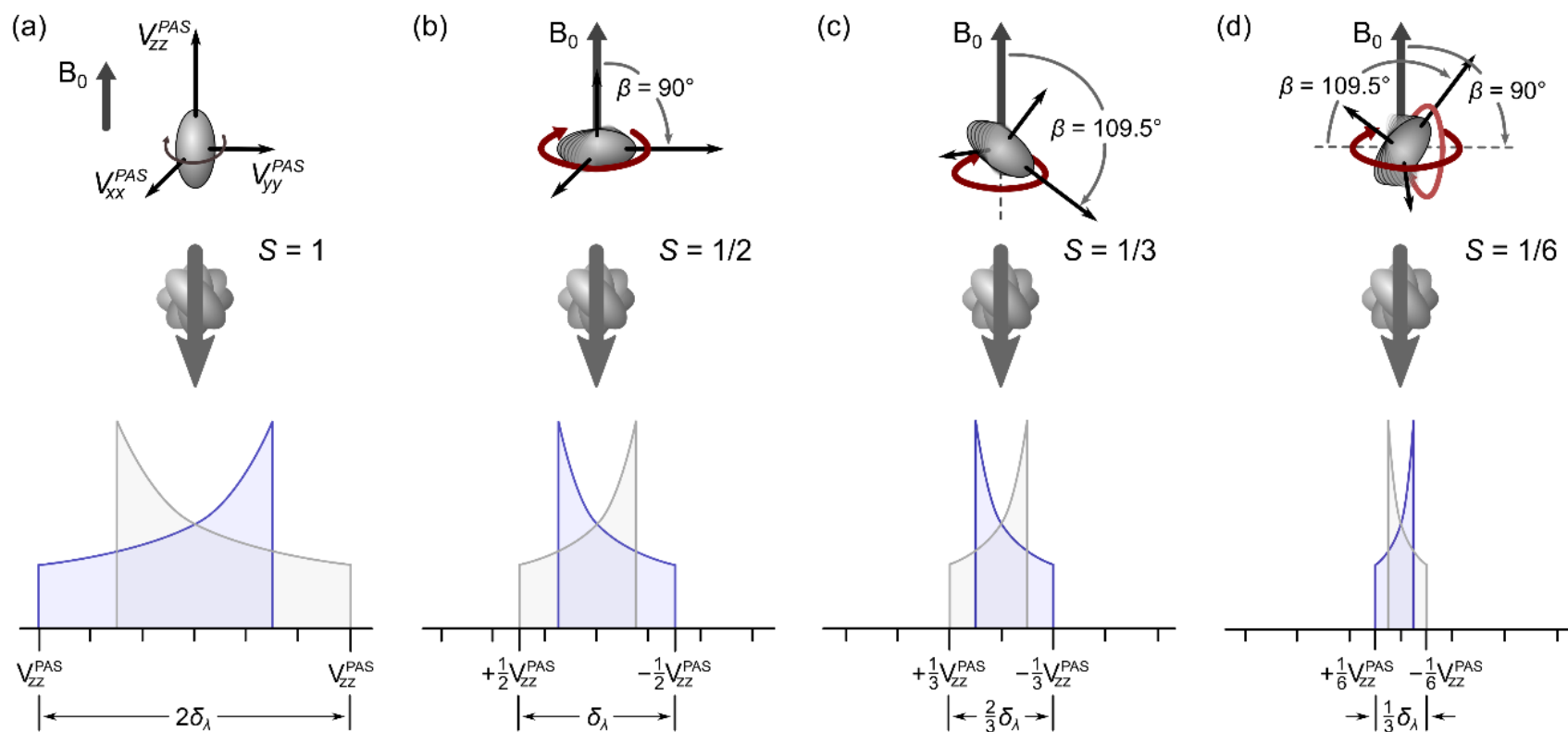
Figure 2.6: To discuss motional averaging consider an axially symmetric tensor interaction (a top) which if all static orientations are present yields a powder pattern (a bottom). If fast planar motion is present (b top) the magnitude of the interaction is reduced by half ($S_{PM} = -1/2$) and thus the observed frequency splitting is reduced by half (b bottom). For motional averaging about a tetrahedral angle (c top) the observed spectral is reduced by a third (c bottom). If both tetrahedral and planar motions are present (d top) the observed frequency splitting is reduced by a sixth (d bottom).
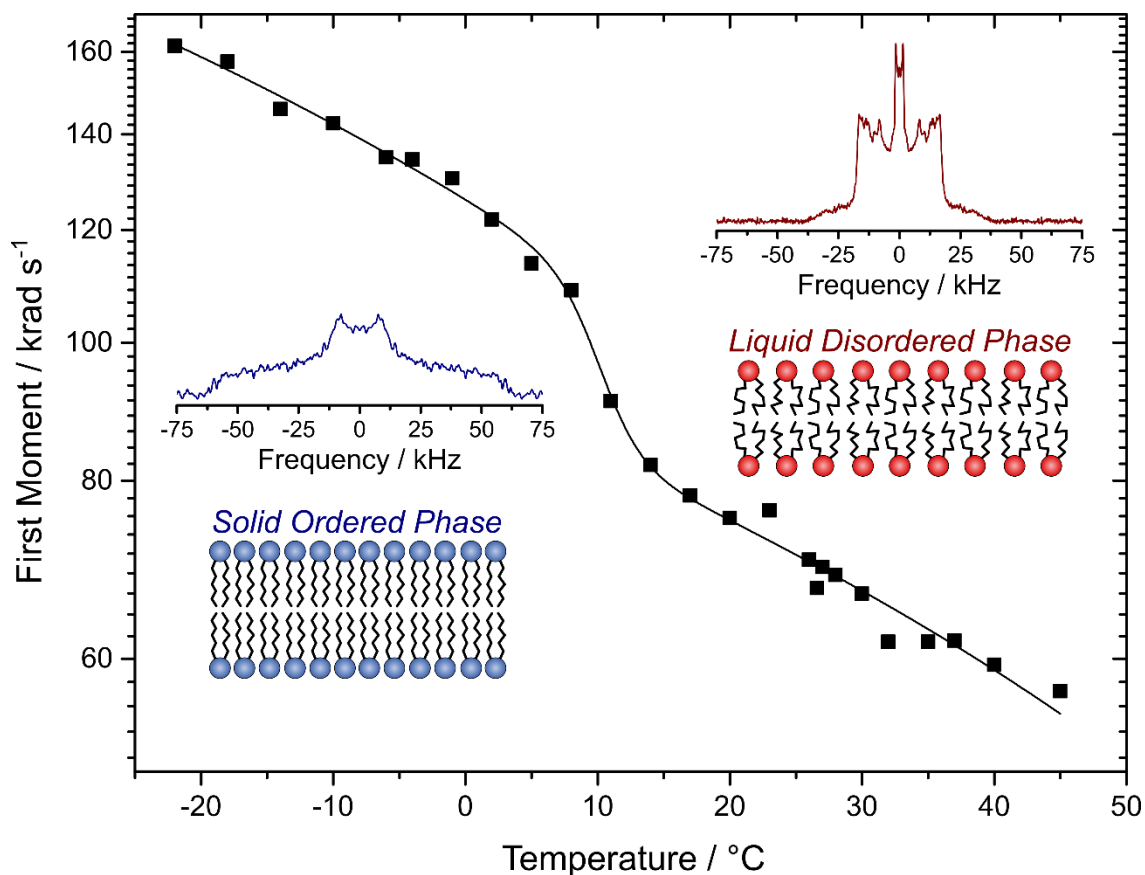
Figure 2.7: A first moment plot of PSM-d$_{31}$ mixed with POPC (1:1 mol.) as a function of temperature reveals a phase transition at 9.9 °C. A represented spectrum (left inset) of PSM-d$_{31}$ mixed with POPC at -10 °C is indicative of the solid ordered phase where the labeled hydrocarbon chains are relatively ordered. While a representative spectrum (right inset) of PSM-d$_{31}$ mixed with POPC at 30 °C is indicative of the liquid crystalline phase where now the hydrocarbon chains are relatively disordered and many of the segments are undergoing distinct dynamics.
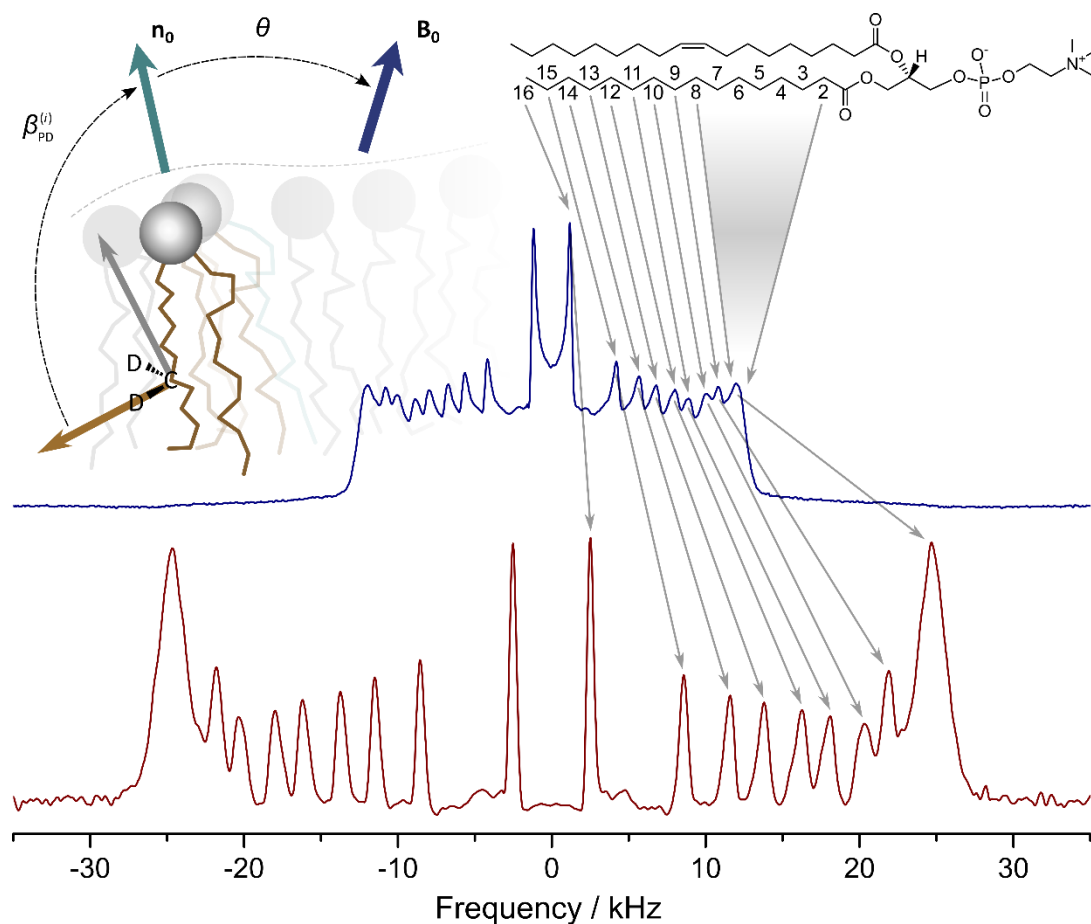
Figure 2.8: For a perdeuterated lipid chain, each segment, represented by the angle $\beta_{PD}^{(i)}$, can potentially produce a distinct powder pattern (top left). Segment numbering ($i$) begins at the carboxyl group and increases until it reaches the terminal methyl of a chain. This is shown for the palmitoyl chain of POPC-$d_{31}$ in the upper right. These powder patterns superimpose to form the blue spectra of POPC-$d_{31}$ at 37 °C as shown in the middle. To enhance the resolution of the spectrum a dePaking algorithm can be performed which deconvolutes the powder patterns to a collection of doublets as shown at the bottom.
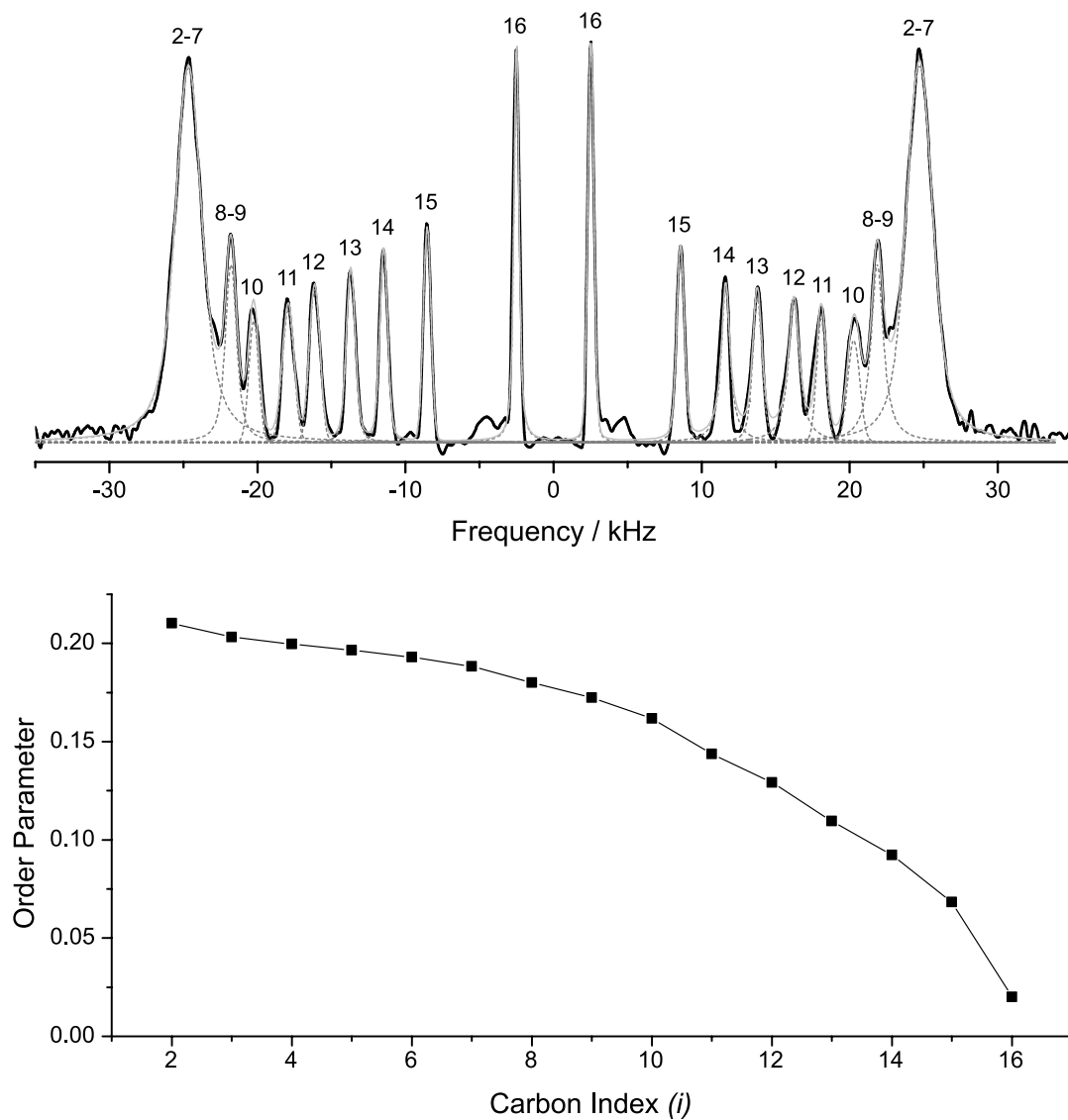
Figure 2.9: DePaked spectra (top) are useful in determining order parameter profiles (bottom). The dePaked spectra shown on top is of POPC-d$_{31}$ at 37 °C (black). To determine the frequency splittings for each doublet pair, Voight (Lorentzian convoluted with a Gaussian lineshape) lineshapes were fit to each distinct peak (grey dotted line) and formed a cumulative fit (grey solid line). The doublet with the maximum width is a composite of many segments. This was split according to area (2 deuterons per segment) and assumed a monotonic decrease in frequency splitting. With equation 2.55, the frequency splittings were used to determine the order parameter profile (bottom).

# CHAPTER 3.    $^2$H NMR IMPLEMENTATION AND ANALYSIS

## 3.1    Introduction

In solution state NMR spectroscopy, molecular motion that is fast and isotropic completely averages anisotropic magnetic and electric interactions. A sharp high-resolution spectrum, revealing residual magnetic interactions, results. In solid state NMR, by contrast, molecular motion is slow and/or anisotropic so that motional narrowing is incomplete. There are two general approaches, broadline NMR and magic angle spinning (MAS) NMR, in this regime. By rapidly spinning a sample about an axis at the magic angle ($\theta = 54.74°$) relative to the magnetic field, MAS spectroscopy eliminates magnetic interactions that scale as $P_2(cos\theta)$ (Levitt, 2008). The methods of solution state NMR spectroscopy can then be applied and under certain spinning conditions specific magnetic interactions can be observed (Griffin, 1998). Broadline NMR spectroscopy extracts details of molecular orientation and anisotropy of molecular reorientation by analysis of the lineshape. This technique allows for a direct measurements of dynamics in bulk materials which has been extensively applied to biological materials (Brown, Lope-Piedrafita, Martinez, & Petrache, 2006) and non-biological materials (Schmidt-Rohr, 1996). It is a niche area of NMR for which standard software often lack necessary features.

Two software programs, "EchoNMR processor" and "EchoNMR simulator", collectively known as "EchoNMR tools", developed to quickly process and analyze one-dimensional solid-state NMR data, will be described along with some theoretical background of the techniques used. EchoNMR tools is developed in the MATLAB® (Mathworks) programming environment which runs as an interpreter language that allows the software demonstrated here not only to be open-source but also easily modified. Both packages utilize a graphical user interface (GUI) without the need for command-line steps which allows for a reduced learning-curve for novices. Advanced features such as automated routines and corrections due to pulse sequence-related distortions are included.

In EchoNMR processor, all processing is done in batch. In this method the original recorded signal is always preserved. Once a processing parameter is changed, the original signal is reprocessed in batch to yield a processed signal, standard spectrum, and a dePaked spectrum. This is in contrast to the iterative approach, where the original signal is not preserved and each processing step is done sequentially. The iterative approach is less processing intensive, but modern computers are capable of all steps of processing within a fraction of a second. One of the drawbacks of the iterative approach is the difficulty in going back in steps. Batch processing avoids all of this. Also EchoNMR processor simultaneously shows the spectrum, achievable due to batch processing, which can aid in finding the appropriate processing parameters.

## 3.2   Pulse Sequences and the Solid Echo

Most modern NMR spectroscopy techniques rely on super conducting magnets to generate the large main magnetic field. The spectra here were recorded with samples placed within a 7.05 T superconducting magnet (Oxford Instruments, Osney Mead, UK) which yields a $^2$H Larmor resonance frequency of 46.0 MHz. To accompany the magnet, and obtain spectra for labeled membrane samples, a homebuilt NMR spectrometer was utilized (Williams et al., 2012). The spectrometer is equipped with an in-house assembled programmable pulse generator, a dual-channel digital oscilloscope (R1200 M; Rapid Systems, Seattle, WA) to acquire signals in quadrature and a temperature controller (1600 Series; Love Controls, Michigan City, IN) that regulates temperature to ±0.5°C.

The aforementioned console uses a pulse sequence at the Larmor frequency which generates an observable signal in the time domain, called the free induction decay (FID). To obtain a spectrum a Fourier transform is then performed. This pulse-Fourier transform technique resulted in a Nobel prize for Richard Ernst in 1991 (Shampo, Kyle, & Steensma, 2012).

To understand the effect of pulses, consider a nucleus in its initial state within the main magnetic field. Since the lowest energy state is aligned with the main magnetic field, there will be a slight excess of nuclear spins in this state, as shown in Figure 3.1 (bottom left). This slight excess is what is observed in NMR spectroscopy. For simplicity, the main

magnetic field will be pointing along the $+\hat{z}$ axis, thus the nuclei aligned in this direction are labeled as $|+z\rangle$. This state has the property of:

$$\langle +z|\hat{I}_Z|+z\rangle = m_{max} \tag{3.1}$$

where $m_{max}$ is the maximum magnetic quantum number (1/2 for spin-half and 1 for spin-one nuclei). Solving the time-dependent Schrödinger equation with the Zeeman Hamiltonian gives the time-evolution of the state:

$$|+z(t)\rangle = e^{-i\omega_0 \hat{I}_Z t}|+z(0)\rangle \tag{3.2}.$$

Notice that the time-dependent wave function has a phase factor that depends on the Larmor frequency and time. With this phase factor, it is typically said that this state is precessing at the Larmor frequency.

The effect of an oscillating pulse on the orientation of the spins is easier to understand with a transform to the rotating frame, which modifies the initial state, $|+z(t)\rangle$:

$$\left|\widetilde{+z(t)}\right\rangle = e^{i\omega_0 \hat{I}_Z t}|+z(t)\rangle = |+z(0)\rangle \tag{3.3}$$

where $\left|\widetilde{+z(t)}\right\rangle$ is the state in the rotating frame. Notice that the explicit time-dependence is canceled out and the state appears static in the rotating frame.

If an additional field is applied along the x-axis it can be used to rotate (nutate in the lab frame) the spin state into the x-y plane (bottom middle of Figure 3.1). From the time-dependent Schrödinger equation with the transverse magnetic field:

$$\left|\widetilde{+y(t)}\right\rangle = e^{-i\omega_P \hat{I}_X t_P}\left|\widetilde{+z(t)}\right\rangle \tag{3.4}$$

where $\omega_P = -\gamma B_P$, $B_P$ is the magnetic field due to the transverse pulse, and $\omega_P t_P = \pi/2$. To achieve this in a laboratory frame, a coil is used to deliver a pulse (top middle of Figure 3.1) oscillating at the Larmor frequency, $\omega_0$, for a pulse length equivalent to $t_P = \pi/(2\gamma B_P)$. Typical pulse lengths for solid-state experiments vary between 2 and 5 μs, where the pulse is supplied by a coil supported by a probe which is inserted into the bore of the superconducting magnet. In the rotating frame, an oscillating pulse appears as a static magnetic field. According to equation 3.4, the resulting state is rotated to the y axis with the state label of $\left|\widetilde{+y(t)}\right\rangle$. This can be verified by finding the expectation value, $\langle \hat{I}_Y \rangle$, of this state:

$$\langle \hat{I}_Y \rangle = \langle \widetilde{+y(t)}|\hat{I}_Y|\widetilde{+y(t)}\rangle = \langle \widetilde{+z(t)}|e^{i\omega_P \hat{I}_X t_P}\hat{I}_Y e^{-i\omega_P \hat{I}_X t_P}|\widetilde{+z(t)}\rangle \qquad (3.5).$$

Taylor expanding the exponentials it can be shown that:

$$e^{i\omega_P \hat{I}_X t_P}\hat{I}_Y e^{-i\omega_P \hat{I}_X t_P} = \hat{I}_Y cos(\omega_P t_P) + \hat{I}_Z sin(\omega_P t_P) \qquad (3.6)$$

and given $\omega_P t_P = \pi/2$, this results in equation 3.5 becoming:

$$\langle \hat{I}_Y \rangle = \langle \widetilde{+z(t)}|\hat{I}_Z|\widetilde{+z(t)}\rangle = m_{max} \qquad (3.7).$$

Following the pulse, the state is projected along the transverse plane. With equations 3.2 and 3.3, now in respect to the $+y$ state, this state can be transformed back to the laboratory frame:

$$|+y(t)\rangle = e^{-i\omega_0 \hat{I}_Z t}|\widetilde{+y(t)}\rangle = e^{-i\omega_0 \hat{I}_Z t}|+y(0)\rangle \qquad (3.8).$$

The phase factor, $e^{-i\omega_0 \hat{I}_Z t}$, indicates that this state is precessing in the $x$-$y$ plane (bottom right of Figure 3.1), which can be shown by finding the $\langle \hat{I}_X \rangle$ and $\langle \hat{I}_Y \rangle$ expectation values. Importantly this precession is a precession of a magnetic moment (due to the summation of the spins). If this magnetic moment is surrounded by a coil, it creates an oscillating magnetic field within the coil. Due to Lenz's law, this results in an observable current, or a free induction (top right of Figure 3.1). This is a near field effect as opposed to the coherent emission of radiation from the sample (Hoult, 2009). Typically, the same coil used to pulse the sample is also used to observe the oscillating magnetic moment. Due to thermal fluctuations the spin state will eventually align back to the $|+z(t)\rangle$ state and the induction will decay away. Thus, this observed signal is called the free induction decay (FID).

At this point it is important to point out that in the most general case spin systems do not exhibit a single resonance at $\omega_0$, but a distribution of resonances due to interactions (some of which produce the theoretical powder patterns). To observe all of these resonances in the FID, the entirety of the frequency distribution needs to be excited by the pulse. In the time-domain, a pulse is simply a sinusoidal wave at the Larmor frequency multiplied by a box function. The length of this box function is equivalent to $t_P = \pi/(2\omega_P)$ for a $\pi/2$ pulse. In the frequency space this pulse is a Dirac delta function at the Larmor frequency convoluted with a sinc function ($2\,sin(\omega t_P/2)/(\omega t_P)$). In the frequency space, the sinc function crosses zero at $\pm\omega = \pm\pi/t_P$. To avoid the distortion that this zero crossing

causes, the magnetic field of the pulse, $B_P$, must be particularly strong. This is especially the case if the orientation-dependence of the interactions are not averaged out such as in the solid state. Because of this solid state NMR spectroscopy tends to use solenoid coils to deliver more power to the sample as opposed to saddle coils which are common in solution state NMR spectroscopy.

The distribution of resonances, due to environmental interactions and orientations, result in a large decoherence. Thus the FID can decay quite quickly below the noise level and can be difficult to observe. In the rotating frame at the center Larmor frequency, there are resonances moving faster and slower than the now static Larmor frequency. With a well-placed 180° pulse about the direction of the Larmor frequency (which is 90° offset from the first pulse) the slow and fast resonances swap places and reconverge (Hahn, 1950). This results in an echo in the FID, which from its maximum can be Fourier-transformed to obtain the full spectrum. In practice for static interactions such as the orientational dependence that produces powder patterns, a second 90° pulse (again 90° offset from the first pulse) suffices (Mansfield, 1965) as shown in Figure 3.2. This is commonly referred to as a solid echo experiment (Levitt, 2008).

In general, the pulsing coil and observing coil are one and the same. As the pulse can be quite powerful, it can take some time to die down (a phenomenon called ringing) before the signal can be observed. This region is referred to as the dead time as depicted in Figures 3.1 and 3.2. As the FID observed in solid-state NMR spectroscopy decays quickly, much of the signal can be lost within the dead time. But if a solid echo pulse sequence is utilized, the echo can occur after the dead time. This can restore a large amount (but not all) of the FID within the observable time domain. Dynamic interactions, such as thermal fluctuations, which result in the sample returning back to equilibrium, cannot be reversed. This will reduce the magnitude of the echo and can even distort the resulting lineshape if the interpulse delay is too large.

### 3.3 FID Processing

EchoNMR processor can open files in various formats, including our home-built and commercial spectrometer formats, with the goal of processing FID produced in echo pulse sequences (see Figure 3.2 for a representative sequence). In general, the recorded FID is needed and EchoNMR processor can automatically open associated parameter files. The FID should be recorded in quadrature, which is the signal from the precessing magnetization (the real channel) and its 90° phase offset (the imaginary channel) are both recorded as shown in the original FID area of Figure 3.3.

Due to the tuning of the probe, the initial point of the precession may not be completely in the real channel. Thus the EchoNMR processor allows the user to manually set the "zeroth-order" phase of the spectrum. This mixes the real and imaginary channels according to an imaginary exponential. For symmetric spectra about the Larmor frequency, such as that produced by $^2$H NMR spectroscopy, ideally the imaginary channel should be flat. This is due to an equal amount of resonances precessing positively and negatively. EchoNMR processor can automatically correct for this by finding the phase such that the slope of the imaginary channel is minimized according to MATLAB's® Nelder-Mead simplex algorithm which is activated by the "Auto Phas" button on the top of Figure 3.3. An example of a phased FID is shown in the processed FID of Figure 3.3, where the red imaginary is minimized. Typically, the phasing process is done first in processing the FID.

The phasing of the FID can also be done through observing the spectral lineshape and, due to the batch processing utilized here, the spectra is simultaneously shown with the FID. As $^2$H NMR spectroscopy typically produces symmetrical powder patterns, the spectra should appear symmetrical with an approximate equal area on each side. In the imaginary channel the spectral area should be equal but of opposite sign, as the resonances are either faster than (positive) or slower than (negative) the Larmor frequency. A trick that can be done is to symmetrize the spectrum (which is an option in the Spectral Processing options of Figure 3.3), where the right side of the spectrum (about zero) is added to the left side of the spectrum. For a properly phased FID, the corresponding imaginary spectrum should cancel itself out under symmetrization for theoretically symmetric spectra.

The baseline for a FID should be at zero. There should not be what is referred to as a DC offset. When one is present it is removed by a technique called phase cycling which adds sequential 90° phases to each pulse in the pulse sequence with each repetition (Levitt, 2008). For the solid echo experiment special consideration of phases must be done to maintain a 90° phase offset between the first two pulses. This alternates the real and imaginary parts of the signal through both quadrature channels with positive and negative amplitudes. After digitization, the computer will appropriately swap the real and imaginary channels and/or flip the sign of the incoming amplitude before adding it to the previously recorded FID. This helps reduce imbalances, especially the baseline, between each channel. However, on our homebuilt system if the pulse sequence is running too fast it can become out of sync with the computer. Thus phase cycling is sometimes turned off for samples which require significant signal averaging, and thus a baseline can appear. For this reason, a user can specify a baseline for each channel in the signal processing panel of Figure 3.3. EchoNMR processor can automatically find this baseline and subtract it out by taking a percentage (defined by the user) of the end of the FID and finding the average value for both the real and imaginary channels which is activated by the "Auto Base" button on the top of Figure 3.3. If there is a baseline in the FID, and not corrected for, it will appear as a sharp peak at the zero frequency of the spectrum.

Although, data acquisition can be set to automatically begin at the expected echo begin point or "echo maximum", it is not always the case and may be prudent to begin recording before the echo to avoid uncertainties. Thus the user can specify the data point at which the echo should occur. As the echo can appear between digitized data points the user may enter a fraction of a data point where EchoNMR processor will interpolate to this point (via cubic spline) and shift the FID accordingly. The processed FID area of Figure 3.3 shows the FID cropped to the echo maximum point. An interpolation-factor option exists which will increase the number of data points in the FID to aid the user in finding the echo maximum. EchoNMR processor can automatically find the echo maximum by fitting a cubic polynomial to the data points near the largest data point which is activated by the "Auto Max" button on the top of Figure 3.3.

Further, EchoNMR processor allows the user to retain the pre-echo data by symmetrizing it with the remaining FID. This can potentially enhance signals that have decayed due to relaxation. However, since the pre-echo data is often a small-number of data points, it is subject to truncation distortion (which appears as a convoluted sinc lineshape in the frequency domain). Since the shape of the echo in the FID is dependent on phasing, the echo finding procedure should be done after phasing.

The determination of the location of the echo maximum is important as it affects the phasing of the spectra in Fourier space. The process of adjusting the first point of a Fourier transform is equivalent to a "first-order" phase correction which is a frequency-dependent phase shift in the frequency space: $e^{i\omega\Delta t}$. Here $\omega$ is the angular frequency and $\Delta t$ is the time offset from the echo maximum. As the spectra is shown simultaneously with the FID, a point chosen outside the echo maximum will result in oscillations in the spectrum due to the complex exponential mixing the imaginary with the real spectra. The further away from the echo maximum, the larger the time offset, $\Delta t$, is, and the worse the oscillations appear. This has the potential of greatly affecting moment values obtained, thus it is quite important to determine the echo maximum accurately. Two culprits affecting this are high frequency noise and interference. In the options panel in the lower left of Figure 3.3, the spectral range option will filter out frequency components outside a defined range before fitting with the automated maximum finding function. This can improve the maximum found and thus the overall phasing of the spectrum.

Since the pulses used can be quite powerful and are many times stronger than the signal observed, the circuit can remain oscillating partway into the FID in a phenomenon called ringing (Levitt, 2008). Thus the beginning part of the observed FID can interfere with the automatic phasing, automatic maximum finding, and FID symmetrization processes. Thus in the "Options and Moments" panel of Figure 3.3, there is a FID crop option which tells the program to ignore a defined number of beginning points of the FID.

### 3.4 Spectral Processing and dePakeing

As with the FID, after each processing parameter is applied, the spectrum is updated instantaneously. This is useful for manual adjustment as phasing and maximum finding has a clear effect on the spectrum as mentioned in the previous section. Although most of the major parts of signal processing is directly applied to the FID, further spectral processing can be done to aid in data interpretation and analysis.

EchoNMR processor also allows the user to adjust the appearance of the spectrum. Noise in the spectrum can be reduced by Lorentzian and/or Gaussian line broadening. This can be done in one of two ways. By either multiplying an exponential or Gaussian decay to the processed FID or convoluting the spectrum with the corresponding Lorentzian or Gaussian line-shape. The convolution method can be activated by enabling the "Post Smoothing" option in the "Spectrum Processing" panel of Figure 3.3. It should be noted that line-broadening also distorts the non-noise parts of the signal as well, so it should be used conservatively. Since the lineshape in $^2$H NMR spectroscopy is theoretically symmetrical, the signal to noise can be improved via the aforementioned symmetrization option. This technique requires that the spectrum is centered about its Larmor frequency to avoid the doubling of peaks. As the imaginary spectrum should be minimal under symmetrization, this can be utilized not only for phasing but also for finding the spectral center (in the center option of the spectral processing panel of Figure 3.3). Also EchoNMR processor can automatically determine this center by finding the frequency at which the spectral area is equal in positive and negative frequencies (via a first signed-moment) which is activated by the "Auto Cent" button on the top of Figure 3.3.

The user can increase the number of data points in the spectrum with the "size" option in the spectrum processing panel of Figure 3.3. This is done by "zero-filling" the FID, which adds data points of zero value to the end of the processed FID (which is a sinc interpolation in the frequency domain). The ability to reduce the noise in a spectrum and increase the number of data points allows for the identification and also fitting of NMR peaks. This is important for the determination of structural parameters such as the order parameter.

To analyze anisotropic line shapes, EchoNMR processor also applies the rapid dePaking algorithm developed by McCabe and Wassall (McCabe & Wassall, 1997) which utilizes a weighted-FFT method. As a reminder, this technique enhances the edges of anisotropic line shapes which is useful in identifying and analyzing signals in spectra with multiple line shapes. Since it is based on a weighted-FFT it can be done rapidly and updated with the original spectrum. As the FFT is weighed, an exponential doesn't transform into a Lorentzian and the Gaussian is not preserved after the transform. Thus the apodization of the FID and convolution of the dePaked spectrum produce slightly different outcomes. Finally, this technique requires the lineshape to be centered at its Larmor frequency, which can be done with the aforementioned techniques.

EchoNMR processor will automatically determine moments of the spectrum in the "Options and Moments" panel of Figure 3.3. The first moment is always determined; however, the user can specify a moment of another order. If the spectrum has a baseline, this will skew any moments calculated. Therefore, EchoNMR processor has a baseline correction option in the "Spectrum Processing" panel of Figure 3.3, which will find the average value of a range of data points specified by the user and subtract it from the spectrum. As the amplitude used in the moment calculation is weighed by frequency, high frequency noise and interference can be a major problem. Therefore, EchoNMR processor will ignore data points outside of the range specified in the spectral range fields of the "Options and Moments" panel of Figure 3.3.

Finally, EchoNMR processor has two options in the "Smoothing and Plotting" panel of Figure 3.3 to change the plotting style and hide parts of the plot. The plotting style allows the user to change if the data points are displayed individually, connected by lines, or other variants. This can help in analysis of the spectrum or even aid in maximum finding of the FID. For the most part, the real part of the spectrum is what is analyzed. For this reason, after processing, it might be useful to hide the imaginary (red in Figure 3.3) parts of the plot thus there is a "Hide Imaginary" option. If the user wants more control over the display of the plot, there is an "Edit Plot" button near the top of Figure 3.3. This allows the user to use MATLAB's in-built plot editing features.

## 3.5    Lineshape Analysis and Fitting

After obtaining a spectrum, its lineshape can be analyzed by fitting against a simulated spectrum. EchoNMR fitter (see Figure 3.4) uses the Nelder–Mead algorithm (supplied by the MATLAB® programming environment) to fit data to a chosen lineshape by minimizing the sum of the squared-difference between the chosen lineshape and the data. As the Nelder–Mead algorithm can yield local minima instead of global minima, EchoNMR Fitter has a parameter-randomization process to attempt to escape local minima. This process is iterative and the user can observe the resulting sum of the squared-difference as the process proceeds, which can be limited or canceled by the user. Further the user can manually adjust each fitting parameter. This allows the user to control the fitting process to obtain an optimal fit.

Primarily, EchoNMR fitter allows users to fit anisotropic line shape patterns including the asymmetric variety (see Figure A.1 in Appendix A) which is simulated using an elliptical integral (Häberlen, 1976). This feature allows it to be particularly useful in solid-state NMR spectroscopy in fitting powder patterns. Users may also choose to fit isotropic line shapes as well. Each line shape may be broadened by a combination of Lorentzian or Gaussian line shapes. A large-number of line shapes can be specified at the expense of processing time. An example of multiple powder pattern fit, with an isotropic lineshape, is shown in Figure 3.5.

EchoNMR fitter has utility beyond $^2$H NMR spectroscopy as other nuclei can produce similar lineshapes. It can also be applied to spectra of other nuclei, such as $^{31}$P. The $^{31}$P spectrum shown in Figure 3.6 is an example of separating two components due to POPE and SM in a POPE/SM (1:1 mol.) mixutre (Shaikh et al., 2002). Typical solution-state NMR spectroscopy produces multiple isotropic lineshapes. As EchoNMR fitter can handle multiple lineshapes, including isotropic lineshapes (see Figure 3.5), it is capable of analyzing some solution NMR spectroscopy data (particularly one-dimensional data).

The software can correct spectral distortion due to finite pulse widths. This "pulse correction" is done in the manner as described by Bloom et al. (Bloom, Davis, & Valic,

1980). This distortion occurs as the width of the pulse is inversely proportional to the frequency space it can excite. Therefore, long pulses can produce distortion near the edges of spectra. Users can adjust for long pulses, off-center pules, the pulse angle, and the number of pulses. If necessary users may allow these parameters to be fit by the program if there are uncertainties.

As well as correcting for the distortion due to pulse sequences, EchoNMR fitter can correct for relaxation during the pulse sequence (see section Appendix A). Since relaxation can be orientationally dependent, and thus appears frequency dependent (Domenici, 2009; Morrison & Bloom, 1993, 1994; Separovic & Cornell, 2000), signals far away from the center-frequency of the spectrum can appear to have lower amplitudes in the frequency domain. Importantly, as frequency-dependent decay processes distort the observed lineshape, they alter the value of the first moment, $M_1$, if calculated from the observed spectrum. When the observed first moment is heavily dependent on the interpulse delay, it is described as tau-dependent (Wassall, Thewalt, Wong, Gorrissen, & Cushley, 1986). To remedy this, the solid echo pulse sequence can be repeated for various values of $\tau$. A $M_1$ vs $\tau$ plot can then be generated which allows the extrapolation of $M_1$ back to $\tau = 0$. This extrapolation is error prone but provides a better range of estimates of a distortion-free $M_1$. Alternatively, EchoNMR fitter uses a frequency-dependent relaxation model (see Appendix A) to distort the simulated lineshape which allows it to better-fit the experimental spectrum. This can correct for distortion due to relaxation and provide a better estimate of the average order parameter thus $M_1$ for simple lineshapes.

## 3.6   Concluding Remarks

Both EchoNMR processor and fitter, collectively referred to as EchoNMR tools, have been designed with a focus on user usability and the open-source mindset. This is achieved in the in the MATLAB® (Mathworks) programming environment which allows for the development of the graphical user interfaces and runs as an interpreter which allows the code to be open-source. The research described in chapter 4 provides an example of a study that demonstrates the utility of the software.
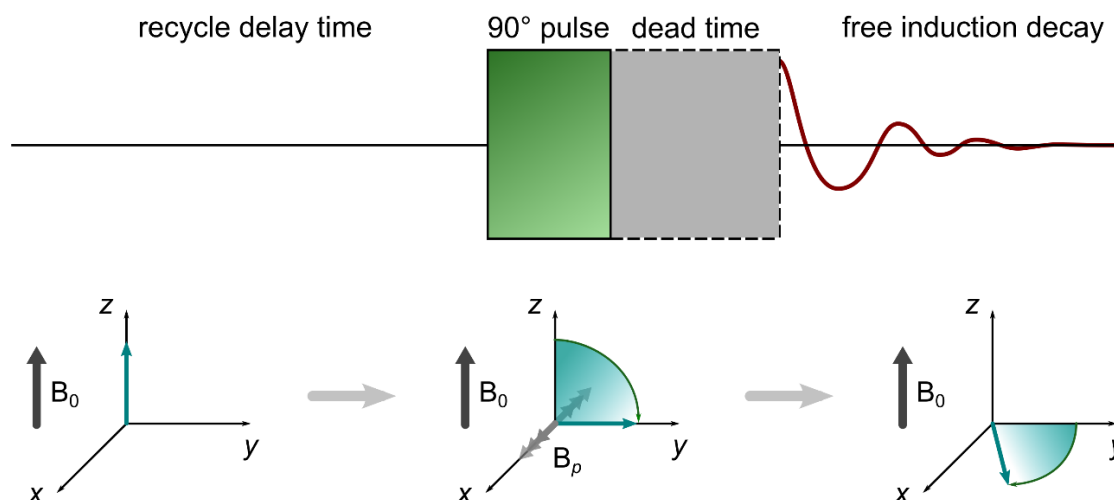
Figure 3.1: In pulse-Fourier transform NMR spectroscopy, pulse sequences are repeated, separated by a recycle delay time, to reduce the signal to noise of an accumulated signal. The goal of the recycle delay time is to allow the sample to return to its initial thermal equilibrium. In this state the lowest and thus most populous magnetic state (blue arrow) is aligned with the main magnetic field, $\mathbf{B_0}$, as shown at the bottom left. For a single-pulse sequence, typically an oscillating electromagnetic magnetic pulse, $\mathbf{B_P}$, is delivered via a coil to the sample (top middle) to nutate the spin state to the $x$-$y$ plane (bottom middle), which is referred to as a 90° pulse. Following the pulse there is a dead time to allow the circuit to recover. While the magnetic spin state is in the $x$-$y$ plane it will precess due to the main magnetic field (bottom right). This precessing spin state causes an oscillating magnetic field in the coil used to deliver a pulse. Thus this can be observed as an electric induction in that coil (top right), which is referred to as a free induction decay (FID). The signal of an FID can be weak so pulse sequences are often repeated to reduce decoherent noise by averaging subsequent FIDs.
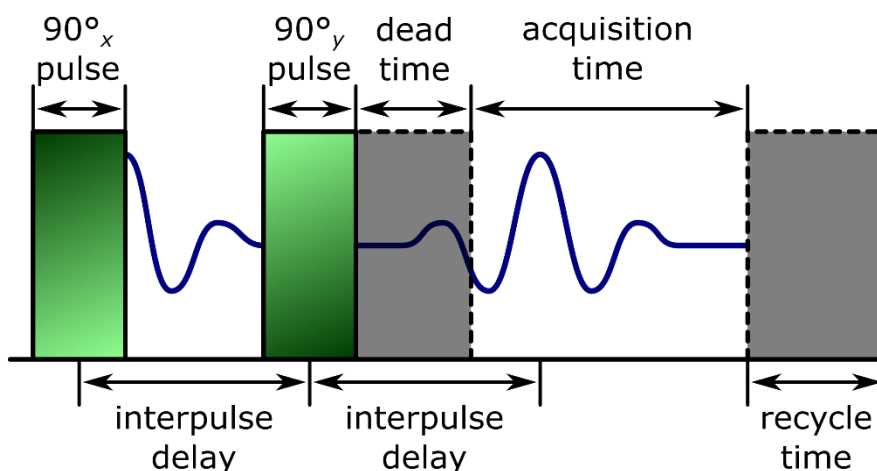
Figure 3.2: The solid echo pulse sequence begins with a 90° pulse. After this pulse (during the interpulse delay) the signal decays due to decoherence from orientationally-dependent, static interactions, and thermal relaxation towards equilibrium. Then another 90° pulse is delivered but at a 90° phase-offset from the original pulse. In the figure, the first pulse is pointed along the x-axis while the second pulse is pointed along the y-axis (in the rotating frame) thus achieving the 90° phase-offset. The goal of this second pulse is to refocus the decoherence due to the orientational and static dependence but it cannot reverse thermal decay back to equilibrium. This results in an echo at a time equivalent to the interpulse delay after the second pulse. If the interpulse delay is chosen wisely, this echo appears after the dead time. This allows the observation of a significant portion of the signal which is often lost in single pulse experiments. As with single pulse experiments, this sequence can be repeated after a recycle delay time to improve signal to noise of the observed FID.
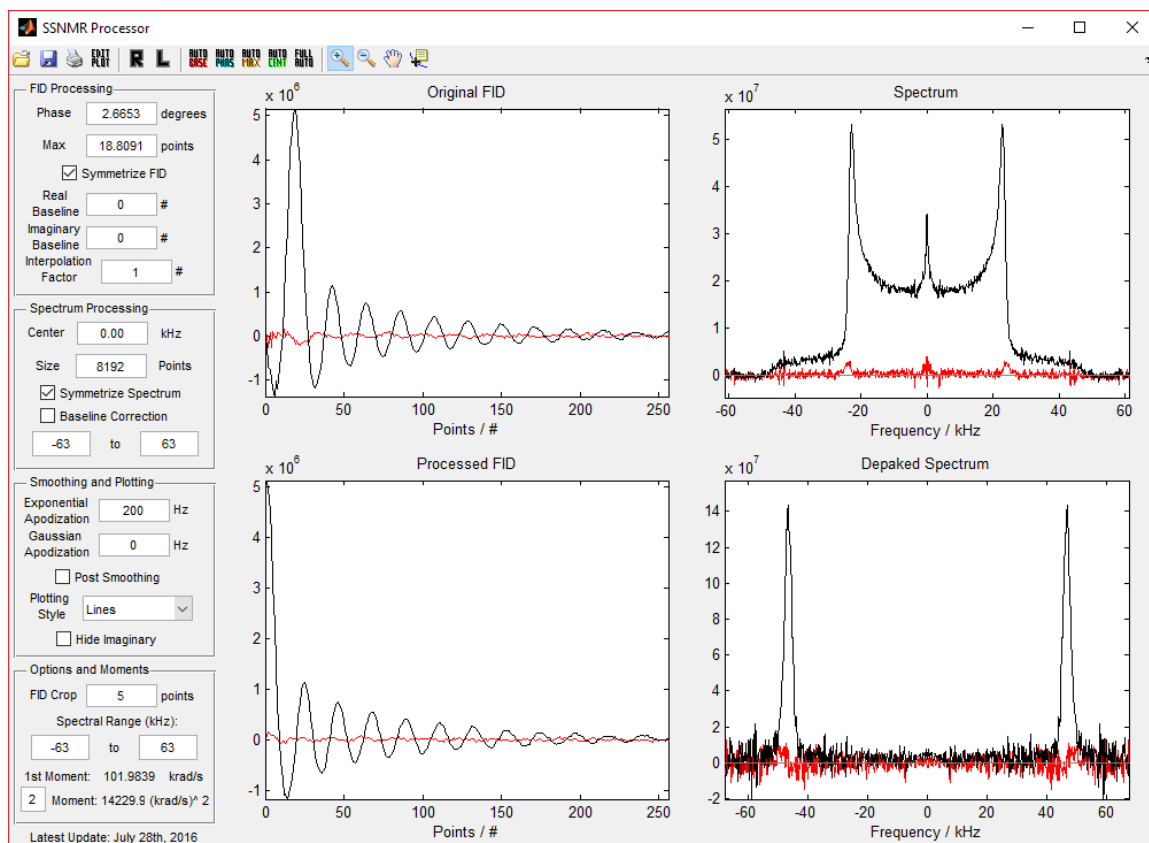
Figure 3.3: EchoNMR processor opens FID files and displays them in the Original FID area, where the real signal is denoted in black and the imaginary is denoted in red. Here a sample spectrum of POPC/chol-$d_1$ (1:1 mol.) at 37 °C in MLV form is shown. This sample was prepared as a 50 wt% aqueous dispersion in 50 mM Tris buffer (pH 7.5). The FID Processing section (upper left) allows the user to phase the FID by angle, specify the maximum, and specify the FID baseline. The result of which is shown in a Processed FID area. Simultaneously EchoNMR processor performs a fast Fourier transform to yield the spectrum (top right) and also a weighted fast Fourier transform to yield a dePaked spectrum (bottom right). The center of the spectra, the amount of data points to be displayed (by zero filling the FID before the Fourier transform), symmetrization (enabled here), and the spectral baseline can be specified in the Spectral Processing section (left). All of these values have automated procedures (upper bar) to aid the user in their determination. The smoothing and plotting section allows users to smooth the spectra via exponential or Gaussian apodization of the FID or post Fourier transform by convoluting the spectra with their Fourier representations. Here the user can change how the spectra is displayed and hide the imaginary parts. Finally, the Options and Moments section provides a few extra features and the ability to calculate moments of arbitrary order.
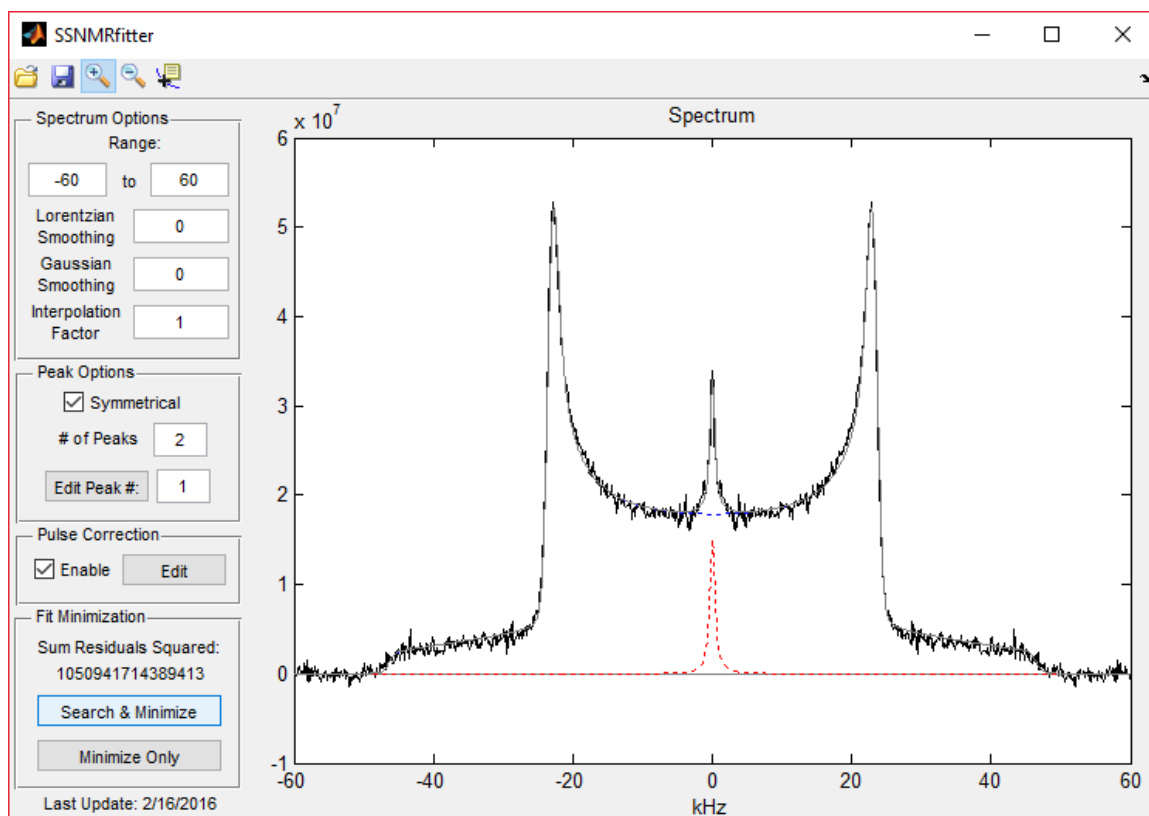
Figure 3.4: EchoNMR fitter is a program designed to simulate NMR lineshapes and fit them to spectra generated by EchoNMR processor. It has the capability of fitting asymmetric powder patterns, isotropic peaks, multiple peaks, and can account for distortion due to pulse widths and relaxation. It utilizes the Nelder–Mead algorithm, or can randomly search a parameter space, to minimize the sum of the squared difference between the recorded spectrum and the simulated spectrum. Here is a sample fit of a spectrum of POPC/chol-$d_1$ (1:1 mol. from Figure 3.3) in 50 wt% aqueous dispersion in 50 mM Tris buffer (pH 7.5) fitted with a powder pattern and isotropic lineshapes within the EchoNMR fitter. The original spectrum is denoted by the black solid line, while simulated powder patterns are represented by red and blue dotted lines (respectively), and their summation is indicated by a grey solid line.

Figure 3.5: EchoNMR fitter is a program designed to simulate NMR lineshapes and fit them to spectra generated by EchoNMR processor. It has the capability of fitting asymmetric powder patterns, isotropic peaks, multiple peaks, and can account for distortion due to pulse widths and relaxation. It utilizes the Nelder–Mead algorithm, or can randomly search a parameter space, to minimize the sum of the squared difference between the recorded spectrum and the simulated spectrum. Here is a sample fit of a spectrum of POPC/chol-$d_1$ (1:1 mol. from Figure 3.3) in 50 wt% aqueous dispersion in 50 mM Tris buffer (pH 7.5) fitted with a powder pattern and isotropic lineshapes within the EchoNMR fitter. The original spectrum is denoted by the black solid line, while simulated powder patterns are represented by red and blue dotted lines (respectively), and their summation is indicated by a grey solid line.

Figure 3.6: As well as fitting $^2$H NMR spectra, EchoNMR fitter can fit other spectra which produce result in second-order Legendre polynomial dependent power patterns and isotropic lineshapes. Here is a sample $^{31}$P NMR spectrum fit with two (single-transition) powder patterns to determine amount of each observed component (Shaikh et al., 2002). The two components are POPE and SM in a POPE/SM (1:1) mixture in MLV form.

# CHAPTER 4.    THE EFFECT OF DHA ON RAFT DOMAINS

## 4.1    Introduction

This work is reprinted and modified from J. J. Kinnun, R. Bittman**,** S. R. Shaikh and S. R. Wassall (2018). DHA Modifies the Size and Composition of Raft-like Domains: A Solid State ^{2}H NMR Study. *Biophys. J., 114*(2), 380–391 Copyright (2017), with permission from Elsevier.

Omega-3 polyunsaturated fatty acids (n-3 PUFA) constitute an influential class of fatty acids that are characterized by having the last double bond located three carbons from the terminal methyl group (Mozaffarian & Wu, 2011). Their dietary intake in fish oils confers a wide range of health benefits that includes the alleviation of inflammation in diseases such as inflammatory bowel disorder, cardiovascular disease, rheumatoid arthritis, nonalcoholic fatty liver disease, obesity and Alzheimer's disease (Calder, 2013; Mozaffarian & Wu, 2011; Simopoulos, 2002). Despite extensive research, the molecular mechanism remains unclear. We have proposed (Shaikh, Kinnun, et al., 2015), as have others (Calder, 2012; Ma et al., 2004) , that modification of molecular organization in plasma membranes following the incorporation of n-3 PUFA into phospholipids may be, in part, responsible. An emerging model has n-3 PUFA remodeling the architecture of membrane domains, often called lipid rafts, enriched in sphingolipids and cholesterol (chol) that compartmentalize signaling proteins (Shaikh, 2012; Shaikh, Wassall, et al., 2015).

There is now general agreement that the lateral distribution of lipids and proteins in membranes is not random (Stillwell, 2015). Driven by differential affinity between the diverse collection of lipids that comprise biological membranes, patches or domains of specific lipid composition exist providing the environment necessary for the function of resident proteins (I. Leventhal et al., 2010). Lipid rafts, especially, have received attention (Lingwood & Simons, 2010). They are tightly packed regions of sphingolipids and cholesterol (chol). The origin of their stability is the structural compatibility of the largely linear configuration adopted by the predominantly saturated chains of sphingolipids and

the planar façade of the tetracyclic ring of chol, together with hydrogen bonding of the hydroxyl group on the sterol to the amide group in the sphingosine backbone of sphingolipids. Polyunsaturated phospholipids have physical properties that in most respects are the antithesis of sphingolipids (Stillwell & Wassall, 2003). The shallow energy barrier to rotation around the single bonds in the repeating =CH-CH$_2$-CH= unit in a PUFA chain allows rapid isomerization through a variety of conformations (Feller et al., 2001). These fluctuations in structure push the rigid steroid moiety of chol away and, to avoid close proximity, polyunsaturated phospholipids segregate into highly disordered domains depleted in chol that are the complete opposite of a lipid raft (Wassall & Stillwell, 2008). This scenario was substantiated in a series of studies on lipid bilayers composed of polyunsaturated 1-palmitoyl-2-docosahexaenoylphosphatidylethanolamine (PDPE) combined with raft-forming chol and sphingomyelin (SM) (Shaikh et al., 2004; Shaikh et al., 2009; Soni et al., 2008). The consensus of results from solid state $^2$H NMR, detergent extraction and DSC was that the mixed membrane separates into PDPE-rich/chol-poor and SM-rich/chol-rich domains that are nanoscale in size. That the degree of segregation depends upon phospholipid head group became apparent in subsequent work that substituted 1-palmitoyl-2-docosahexaenoylphosphatidylcholine (PDPC) for PDPE in the mixture of lipids (Williams et al., 2012). Although PDPC-rich/chol poor domains were formed, an analysis of $^2$H NMR spectra obtained with an analog of PDPC perdeuterated in the *sn*-1 chain (PDPC-d$_{31}$) indicated that a substantial amount of the polyunsaturated phospholipid infiltrated SM-rich/chol-rich raft-like domains. This finding made with a protein-free model system correlates with the uptake of n-3 PUFA into detergent-resistant membranes (DRM) seen in vitro and in vivo, which was central to the formulation of the hypothesis that n-3 PUFA target lipid rafts (Yaqoob & Shaikh, 2010).

 In the experiments described here, solid state $^2$H NMR spectroscopy is applied to compare the molecular organization of [$^2$H$_{31}$]-*N*-palmitoylsphingomyelin (PSM-d$_{31}$) in model membranes prepared from PDPC/PSM-d$_{31}$ (1:1 mol) and 1-palmitoyl-2-oleoylphosphatidycholine (POPC)/PSM-d$_{31}$ (1:1 mol) in the absence and presence of chol (1:1:1 mol) (the molecular structure of each lipid is shown in Figure B.1, Appendix B). The 1:1:1 mol mixture represents the canonical raft mixture employed in studies of model

membranes (Veatch & Keller, 2003a) and allows direct comparison with our previous work (Shaikh, Kinnun, et al., 2015; Williams et al., 2012). PDPC is representative of a phospholipid where n-3 PUFA consumed in the diet incorporates (Lands, M. Inoue, Sugiura, & Okuyama, 1982). It has a saturated fatty acid, palmitic acid, at the *sn*-1 position and docosahexaenoic acid (DHA, 22:6$\Delta$) with 22 carbons and 6 double bonds (Feller et al., 2001; I. Levental et al., 2010; Shaikh, 2012; Shaikh, Kinnun, et al., 2015; Soni et al., 2008; Yaqoob & Shaikh, 2010), which is one of major bioactive components in fish oils, at the *sn*-2 position. POPC with oleic acid (OA, 18:1$\Delta$) at the *sn*-2 position (Stillwell, 2015) serves as a monounsaturated control. While earlier work established that PDPC incorporates into domains enriched in SM and chol, what happened to molecular organization within the raft-like domain remained to be determined. By observing PSM-$d_{31}$, an analog of SM with perdeuterated palmitic acid for its amide-linked side chain, one of the raft-forming molecules was directly probed in the current research. Complementary experiments looking at $[3\alpha{-}^2H_1]$cholesterol (chol-$d_1$), an analog of chol with deuterium substituted at the $3\alpha$ position, were also performed.

## 4.2    Materials and Methods

Avanti Polar Lipids (Alabaster, AL) was the source for POPC, PDPC and egg SM (eSM with *N*-acyl fatty acid composition (in mol%) 16:0 (86%), 18:0 (6%), 22:0 (3%), 24:1 (3%) and unknown (2%) assayed by the supplier). PSM-$d_{31}$ was synthesized as previously described (Bittman & Verbicky, 2000). Chol and chol-$d_1$ were purchased from Sigma Chemical (St. Louis, MO) and Cambridge Isotope Laboratories (Andover, MA), respectively. Butylated hydroxyl toluene (BHT) was obtained from Fisher Science Education (Hanover Park, IL), while Cambridge Isotope Laboratories was the supplier for deuterium depleted water.

Multilamellar dispersions of 50 wt% PDPC/PSM-$d_{31}$ (1:1 mol), PDPC/PSM-$d_{31}$/chol (1:1:1 mol), POPC/PSM-$d_{31}$ (1:1 mol), POPC/PSM-$d_{31}$/chol (1:1:1 mol), PDPC/eSM/chol-$d_1$ (1:1:1 mol) and POPC/eSM/chol-$d_1$ (1:1:1 mol) were prepared in 50 mM Tris (pH 7.5). The procedure, which included precautions to minimize oxidation, was outlined in our earlier publications (Williams et al., 2012). Briefly, lipid mixtures comprised of ~30-50 mg

total lipid were first codissolved in chloroform. BHT was also added in 1:250 mol ratio with respect to lipid to serve as an antioxidant for samples containing PDPC. The organic solvent was evaporated using a stream of argon (samples containing PDPC) or nitrogen (samples containing POPC) gas and the samples were then put under vacuum overnight to remove remaining chloroform. An equal weight of 50 mM degassed Tris buffer solution relative to dried lipid was added, the samples were vortex-mixed and 2 mL extra deuterium depleted water was added to enable the measurement of pH that was adjusted to 7.5. Three lyophilizations of the samples were subsequently performed in the presence of excess (2 mL) deuterium depleted water to reduce the amount of $^2$HHO from its naturally abundant level. Samples were finally rehydrated to 50 wt%, followed by 3 cycles of freezing and thawing to ensure a uniform mixture. In all instances, hydration was performed above 45 °C, which exceeds the temperature of the gel-to-liquid-crystalline phase transition for all the lipids (Koynova & Caffrey, 1998; Shaikh et al., 2009). The resultant samples were transferred to a 5 mm NMR tube, which was sealed with a cap and Teflon tape.

Solid state $^2$H NMR experiments were performed at 46.0 MHz on a homebuilt NMR spectrometer with a 7.05 T superconducting magnet (Oxford Instruments, Osney Mead, UK) (Williams et al., 2012). The spectrometer is equipped with an in-house assembled programmable pulse generator, a dual-channel digital oscilloscope (R1200 M; Rapid Systems, Seattle, WA) to acquire signals in quadrature and a temperature controller (1600 Series; Love Controls, Michigan City, IN) that regulates temperature to ±0.5°C. A phase-alternated quadrupolar echo sequence ($90°_x$-τ-$90°_y$-aquire-delay) was implemented to eliminate spectral distortion due to the receiver recovery time (J.H. Davis, Jeffrey, Bloom, Valic, & Higgs, 1976). The parameters used were 90° pulse width = 3.7 μs; separation between pulses $τ$ = 50 μs; delay between pulse sequences = 1.0 s; sweep width = ±100 or ±250 kHz; and number of scans = 2,000-100,000 depending on signal intensity.

## 4.3   POPC/PSM-d$_{31}$ and POPC/PSM-d$_{31}$/chol Results

Solid-state $^2$H NMR spectra were acquired for PSM-d$_{31}$ in mixtures with POPC (1:1 mol) and POPC and chol (1:1:1 mol), as well as for chol-d$_1$ in mixtures with with POPC and eSM (1:1:1 mol). The experiments were run from high to low temperature between a

maximum of 45 °C and a minimum of -25 °C, which encompasses the gel-to-liquid-crystalline phase transition for each individual lipid. PSM-d$_{31}$ serves as a deuterium labeled substitute for eSM. As the major constituent (86 mol%), PSM dominates the physical properties of the natural lipid. The gel to liquid crystalline transition for eSM at 39 °C (width-at-half height ~1-2 °C) compares with 41 °C (width-at-half height ~1 °C) for pure PSM (28,29). Thus, the results obtained with PSM-d$_{31}$ and chol-d$_1$ here, and with POPC-d$_{31}$ in mixtures with eSM and chol in earlier work by Williams et al. (Williams et al., 2012), provide information on closely similar systems.

Examples of the spectra recorded for POPC/PSM-d$_{31}$ (1:1 mol) are shown in Figure 4.1 (left column). The spectrum obtained at -10 °C is characteristic of the gel phase (J. H. Davis, 1983). It is broad and relatively featureless with shoulders at around ±63 kHz and a central pair of peaks separated by ~15 kHz. This shape reflects the slow rotational diffusion undergone by the rigid, all-*trans* palmitic acid chains on PSM-d$_{31}$ in the mixed membrane with POPC. The same overall spectral shape remains upon raising the temperature to 2 °C, although intensity is reduced at the edges as the chains move more freely. By 23 °C the spectrum is narrowed by fast axial rotation to one that is a signature for the lamellar liquid crystalline phase (J. H. Davis, 1983). Isomerization occurs about C-C bonds in the PSM-d$_{31}$ chains that are melted in the mixture with POPC. The spectrum consists of a narrow signal with peaks at ±2 kHz due to the disordered terminal methyl groups superposed upon a broader superposition of signals due to progressively more ordered methylene groups. A plateau region of methylene groups that are motionally equivalent in the upper portion of the chain is responsible for the sharp edges at ±18 kHz. The further narrowing and sharpening of peaks that take place at higher temperature as the chains become increasingly more mobile are illustrated by the spectra collected at 30 and 37 °C.

The spectra for POPC/PSM-d$_{31}$/chol (1:1:1 mol) displayed in Figure 4.1 (right column) demonstrate that the sterol affects the molecular organization of the sphingolipid in the mixture with POPC. As in the absence of chol, the spectrum at -10 °C is gel-like in form. There is a reduction in the intensity of the outermost shoulders, nevertheless, that is symptomatic of the disruption of chain packing that chol produces in the gel state. At 0 °C

the impact of the sterol is even more apparent. A spectral component that is ±30 kHz in width, indicating the onset of axial rotation for methylene groups, has begun to emerge. The intensity of this component, within which peaks also appear, grows with increasing temperature until by 20 °C the spectrum has become entirely liquid crystalline-like in form. The constraint on motion of the PSM-d$_{31}$ chains imposed by the rigid steroid in the liquid crystalline state, however, is discernible in the much greater width of the spectrum. An increase in order of >50% due to chol is indicated by the sharp edges at ±30 kHz that characterize the spectral shape. This trend continues as the temperature is raised to 30 and 37 °C. Despite a reduction in width and greater resolution of peaks, inspection of the spectra collected at the higher temperatures implies a similar differential in order between with and without sterol persists.

Figure 4.1 presents spectra that are representative of the data obtained over the entire range of temperature studied. To elaborate the trends seen, the first moment $M_1$ was calculated for all of the spectra that were collected using equation 2.50 and was then plotted against temperature in Figure 4.2 (upper panel). Moments slowly decreasing with temperature designate that PSM-d$_{31}$ adopts gel higher (> 13 °C) temperature, respectively, in the 1:1 mol mixture with POPC when chol is absent. A drop in the value of $M_1$ between these temperature regimes occurs with a midpoint at 10 °C. The drop is ascribed to the motional narrowing of the spectrum that accompanies the melting of the perdeuterated $N$-acyl chain on PSM-d$_{31}$. It is appreciably depressed in temperature compared to the gel to liquid crystalline transition for pure PSM-d$_{31}$ (38 °C) (Bunge et al., 2008). In the presence of chol, by contrast, there is no longer a discontinuity in the variation of the moments with temperature. The magnitude of $M_1$ for PSM-d$_{31}$ mixed with POPC and chol in 1:1:1 mol ratio gradually reduces from a value indicating gel phase to one associated with a liquid crystalline state that is substantially ordered by the sterol.

The spectra for PSM-d$_{31}$ in POPC/PSM-d$_{31}$ bilayers and in POPC/PSM-d$_{31}$/chol bilayers are interpreted in terms of heterogeneous mixing of lipids. According to the model, there is incomplete de-mixing of lipids so that SM-rich and PC-rich domains form (Shaikh, Kinnun, et al., 2015; Williams et al., 2012). This view is corroborated by the marked

disparity in molecular organization revealed by the first moments measured here for PSM-$d_{31}$ in POPC/SM-$d_{31}$ and the values we published for POPC-$d_{31}$ in bilayers of POPC-$d_{31}$/eSM prepared in the same molar ratio (Figure B.2, Appendix B) (Williams et al., 2012). The first moment may be equated via equation 2.51 to an average order parameter $\bar{S}_{CD}$ at temperatures ($\geq$20 °C) where the spectra establish both PSM-$d_{31}$ and POPC-$d_{31}$ are liquid crystalline in their respective mixtures. Consistent with the formation of SM-rich (more ordered) and PC-rich (less ordered) domains, the value of $\bar{S}_{CD}$ evaluated at 37 °C is substantially higher for PSM-$d_{31}$ ($\bar{S}_{CD}$ = 0.203) than POPC-$d_{31}$ ($\bar{S}_{CD}$ = 0.137) (Table B.1, Appendix B). A significant distinction between the moments determined in the current work for PSM-$d_{31}$ and previously for POPC-$d_{31}$, likewise, exists following the addition of chol to POPC/PSM-$d_{31}$ and POPC-$d_{31}$/eSM in 1:1:1 molar amount (Figure B.2, Appendix B) (Williams et al., 2012). Indicative of segregation into domains, once again the average order parameter evaluated at 37 °C for PSM-$d_{31}$ ($\bar{S}_{CD}$ = 0.288) is correspondingly much greater than for POPC-$d_{31}$ ($\bar{S}_{CD}$ = 0.231) (Table B.1, Appendix B). It should be borne in mind that a differential in order between lipids does not necessarily mean they are in separate domains. Lipids with chains that possess substantially different intrinsic order can exhibit different order parameters when homogeneously mixed (Hsueh, Giles, Kitson, & Thewalt, 2002). The difference in average order parameter ($\Delta\bar{S}_{CD} \sim 0.06$) measured between lipids in mixed bilayers in the current study, however, is too big to be entirely explained by this effect.

A fundamental tenet of our spectral analysis is that the domains formed in POPC/PSM-$d_{31}$ and POPC/PSM-$d_{31}$/chol mixed membranes are nanoscale (<10's nm) in dimension. The small size explains why only a single spectral component, rather than separate signals from SM-rich and PC-rich domains, is discernible in the spectra observed in the current work at higher temperature that are liquid crystalline in form (Fig. 4.1, left and right column). Lateral diffusion of PSM-$d_{31}$ in-and-out of domains is sufficiently fast to produce a spectrum that is a population weighted average for the two environments (Bloom & Thewalt, 1994). The same interpretation was applied to the $^{2}$H NMR spectra for POPC-$d_{31}$ that were observed under equivalent conditions in our prior study of POPC-$d_{31}$/eSM and POPC-$d_{31}$/eSM/chol (Williams et al., 2012). Single component spectra have also been

reported for deuterated analogs of lipids in POPC/SM/chol bilayers by other groups and attributed to fast exchange between domains (Aussenac, Tavares, & Dufourc, 2003; Bartels, Lankalapalli, Bittman, Beyer, & Brown, 2008; Bunge et al., 2008; Engberg, Yasuda, et al., 2016). That coexisting domains form in bilayers containing SM, unsaturated PC and chol has been confirmed by a variety of approaches, and the consensus is that they are nanoscopic in POPC/SM/chol bilayers (Pathak & London, 2015; Petruzielo, Heberle, Drazba, Katsaras, & Feigenson, 2013). Direct evidence, in particular, was obtained using techniques sensitive on a shorter length scale/faster timescale (such as Förster resonance energy transfer (FRET) and small angle neutron scattering (SANS)) than $^2$H NMR spectroscopy.

## 4.4    PDPC/PSM-d$_{31}$ and PDPC/PSM-d$_{31}$/chol Results

Solid-state $^2$H NMR spectra were acquired for PSM-d$_{31}$ in mixtures with PDPC (1:1 mol), PDPC and chol (1:1:1 mol), as well as for chol-d$_1$ in mixtures with PDPC and eSM (1:1:1 mol). Similar to the POPC mixtures, the experiments were run from high to low temperature between a maximum of 45 °C and a minimum of -25 °C, which encompasses the gel-to-liquid-crystalline phase transition for each individual lipid.

Examples of the spectra recorded for PDPC/PSM-d$_{31}$ (1:1 mol) are shown in Figure 3 (left column). At -10 °C the spectrum for PDPC/PSM-d$_{31}$ is broad with shoulders near ±63 kHz signifying gel phase. The presence of rapidly reorienting PSM-d$_{31}$, unlike in the mixture with POPC at the same temperature (Figure 4.1, left column), is apparent in the central portion of the spectrum where there is a narrow pair of peaks separated by ~3 kHz superposed upon a spectral component with edges at ±17 kHz. Peaks begin to become visible in this central portion of the spectrum, presumably reflecting a gradient of mobility in the bottom part of the PSM-d$_{31}$ chains, and there is a reduction in the relative intensity of the broad component on raising the temperature to 0 °C. By 20 °C the broad component has disappeared and more peaks are resolved. The spectrum, with sharp edges at ±15 kHz due to the plateau region of approximately uniform order parameter in the top half of the chains, has the definitive shape associated with the liquid crystalline state. A slight narrowing and better resolution of peaks is possessed by the spectra at 30 and 37 °C that

retain the same overall shape. Reflecting the influence of the polyunsaturated phospholipid on the sphingolipid, greater disorder and a shorter plateau region are indicated by the smaller width and lower intensity of the edges seen for PSM-d$_{31}$ in the mixed membrane with PDPC than POPC (Figuure 4.1, left column). This trait was observed in spectra comparing PDPC-d$_{31}$ and POPC-d$_{31}$, originally in single component bilayers and subsequently in mixtures with eSM (Salmon, Dodd, Williams, Beach, & Brown, 1987; Williams et al., 2012).

A gel-like state following the introduction of cholesterol is indicated by the broad spectrum shown for PDPC/PSM-d$_{31}$/chol (1:1:1 mol) at -10 °C in Figure 4.3 (right column). That the packing of PSM-d$_{31}$ chains is disrupted by the sterol is evident, like in PSM-d$_{31}$/POPC/chol at the same temperature (Fig. 1, right column), from the small intensity in the wings of the spectrum at around ±60 kHz. A little higher in temperature, a spectral component with shoulders at ±30 kHz appears riding on the wider background of the spectrum at 0 °C. It is attributed to methylene groups on PSM-d$_{31}$ chains rotating in extended conformation, revealing coexistence of liquid ordered (l$_{o}$) and gel phases. Then by 20 °C, spectral intensity due to PSM-d$_{31}$ in the gel phase has disappeared. The spectral component ascribed to rotating PSM-d$_{31}$ chains has become narrower with edges that are better defined. Peaks within this component have begun to show up, with a resolution that the spectra at 30 and 37 °C illustrate improves with increasing temperature. An almost doubling in the width of the spectra relative to PDPC/PSM-d$_{31}$ (Figure 4.3, left column) reflects the expected ordering effect of cholesterol on lipid chains in the liquid crystalline state. The increase is somewhat greater than seen in the POPC/PSM-d$_{31}$/chol. What is more notable with respect to the POPC-containing system is the appearance of two separate signals (indicated by arrows) for the methyl groups in the center of the spectra for PDPC/PSM-d$_{31}$/chol at the higher temperatures (Figure 4.3, right column). These peaks are ascribed PSM-d$_{31}$ residing in more-ordered (outer pair of peaks) and less-ordered domains (inner pair of peaks) in the PDPC-containing system.

The variation with temperature of all of the spectra acquired with the PDPC/PSM-d$_{31}$ and PDPC/PSM-d$_{31}$/chol samples is summarized in the plot of first moment against temperature in Figure 4.2 (lower panel). As in the mixture with POPC (Figure 4.2, upper panel), gel ($M_1 > 11 \times 10^4$ s$^{-1}$) and liquid crystalline ($M_1 < 6 \times 10^4$ s$^{-1}$) phase are indicated for PSM-d$_{31}$ mixed with PDPC by moments that decrease slowly with temperature at low ($< 5$ °C) and high ($> 12$ °C) temperature, respectively. The midpoint of the abrupt drop in value of the first moment between the two phases occurs at 8 °C, slightly lower than in POPC/PSM-d$_{31}$ (10 °C) and much lower again than in single component PSM-d$_{31}$ bilayers (38 °C) (Bunge et al., 2008). Following the addition of chol, like with POPC/PSM-d$_{31}$/chol (Figure 4.2, upper panel), the dependence upon temperature of the moments for PDPC/PSM-d$_{31}$/chol does not exhibit a discontinuity over the temperature range studied (Figure 4.2, lower panel). There is a gradual reduction with increasing temperature in the magnitude of $M_1$ for PSM-d$_{31}$ mixed with PDPC and chol in 1:1:1 mol ratio from a value representative of gel phase to one signifying a liquid crystalline state that the sterol has ordered appreciably.

We attribute the spectra for PDPC/PSM-d$_{31}$ and PDPC/PSM-d$_{31}$/chol to a superposition of signals from PSM-d$_{31}$ partitioned between coexisting SM-rich and PC-rich domains. Similar to what we found in the samples containing POPC, this assessment is supported by comparing the first moments reported here with the very different values measured for PDPC-d$_{31}$ in our earlier study of PDPC-d$_{31}$/eSM and PDPC-d$_{31}$/eSM/chol (Figure B.3, Appendix B) (Williams et al., 2012). Average order parameters calculated from the moments obtained at 37 °C illustrate the difference in molecular organization between SM and PC (Table B.1, Appendix B). The average order parameter for PSM-d$_{31}$ ($\bar{S}_{CD} = 0.155$) in PDPC/PSM-d$_{31}$ is >25% higher than for PDPC-d$_{31}$ ($\bar{S}_{CD} = 0.122$) in PDPC-d$_{31}$/eSM, while the average order parameter for PSM-d$_{31}$ ($\bar{S}_{CD} = 0.253$) in PDPC/PSM-d$_{31}$/chol is >30% higher than for PDPC-d$_{31}$ ($\bar{S}_{CD} = 0.192$) in PDPC-d$_{31}$/eSM/chol. Both in the absence and presence of chol, the values reflect the greater order expected for SM-rich relative to PC-rich domains.

The domains must be small (<10's nm) in PDPC/PSM-$d_{31}$ since, just as we saw in POPC/PSM-$d_{31}$ (Fig. 1, left column), separate signals from PSM-$d_{31}$ in SM-rich and PC-rich domains possessing differing degrees of chain order are not resolved in the liquid crystalline-like spectra recorded at higher temperature (Figure 4.3, left column). Lateral diffusion produces fast exchange between the domains, collapsing the spectrum to a population-weighted average of the spectra for the individual domains. The same explanation was similarly invoked to interpret the spectra obtained with the equivalent sample where the labeled analog was switched from PSM-$d_{31}$ to PDPC-$d_{31}$ in PDPC-$d_{31}$/eSM (Williams et al., 2012). Inspection of the spectra for PDPC/PSM-$d_{31}$/chol reveals that the situation changes upon the introduction of chol (Figure 4.3, right column). Two spectral components due to PSM-$d_{31}$ in ordered SM-rich and less ordered PC-rich domains are resolved at higher temperature, as is clearly reflected in the splitting into two signals of the signal assigned to the methyl groups in the center of the spectra. The domains are enlarged in size (> 10's nm) in the PUFA-containing membrane when chol is present, so that the exchange of PSM-$d_{31}$ between domains is slow and a superposition of spectra from the two environments is the outcome. An increased domain size was analogously deduced from the $^2$H NMR spectra that we observed for PDPC-$d_{31}$ in the corresponding PDPC-$d_{31}$/eSM/chol system (Williams et al., 2012). Consistent with the larger domains we see in PDPC- vs. POPC-containing mixtures with SM and chol, imaging microscopy and computer simulations show that replacing DHA- for OA-containing PC promotes the formation of larger domains in mixed membranes of analogous composition (Georgieva et al., 2015; Konyakhina & Feigenson, 2016; K. R. Levental et al., 2016).

## 4.5   DHA Increases Domain Size

The lipid raft concept continues to evolve as an underlying principle in the structure and functioning of cellular membranes, especially for signal transduction (I. Levental & Veatch, 2016; Lingwood & Simons, 2010). The potential role that n-3 PUFA may play in remodeling the architecture of lipid rafts is addressed in the current study. Nutritionally, n-3 PUFA are associated with reducing the symptoms of a multitude of diseases (Calder, 2013, 2015; Mozaffarian & Wu, 2011; Simopoulos, 2002). The uptake of n-3 PUFA into phospholipids in the plasma membrane that then modulate the stability of lipid rafts and

thereby the activity of signaling proteins has been suggested to be a contributing factor (Calder, 2015; Lindblom & Orädd, 2009; Ma et al., 2004; Shaikh, 2012; Shaikh, Kinnun, et al., 2015; Shaikh, Wassall, et al., 2015; Yaqoob & Shaikh, 2010).

To study how PDPC affects the structure of raft-like domains solid-state $^2$H NMR spectroscopy was utilized. $^2$H labeled analogs of the lipid-raft molecules SM (PSM-$d_{31}$) and chol (chol-$d_1$) were observed in model membranes prepared from mixtures with PDPC and, as a monounsaturated reference, POPC. An increase in the size of domains in the presence of PDPC is revealed by the spectra. These results are further interpreted in terms of heterogeneity in the lateral distribution of DHA-containing PC molecules within raft-like domains.

The observation of two components attributed to methyl groups in the spectra of PDPC/PSM-$d_{31}$/chol (Figure 4.3, right column), while only one component appears in the spectra of POPC/PSM-$d_{31}$/chol (Figure 4.1, right column), indicates that substituting DHA for OA increases domain size. In the OA-containing membrane, diffusion mediated exchange between SM-rich (more ordered) and PC-rich (less ordered) domains at a rate faster than the difference in intrinsic quadrupolar splitting for PSM-$d_{31}$ in the domains produces a time-averaged spectrum (Mannock, McIntosh, Jiang, Covey, & McElhaney, 2003). Exchange between the domains that are larger in the DHA-containing membrane is slow compared to the difference in splitting for PSM-$d_{31}$ within them, so that separate signals are observed. This assessment is consistent with earlier work comparing PDPC-$d_{31}$/eSM/chol and POPC-$d_{31}$/eSM/chol mixtures (1:1:1 mol) where two spectral components due to methyl groups were resolved for PDPC-$d_{31}$ but just one for POPC-$d_{31}$ (Williams et al., 2012). Further support is given by spectra for the PDPC/eSM/chol-$d_1$ and POPC/eSM/chol-$d_1$ mixtures (1:1:1 mol) (Figure B.4, Appendix B). There is a superposition of powder patterns from chol-$d_1$ in two domains in the presence of PDPC, clearly discernible in two pairs of peaks - an outer pair from chol-$d_1$ (split by $\Delta\nu_r \sim 48$ kHz) in the ordered SM-rich domain and an inner pair from chol-$d_1$ (split by $\Delta\nu_r \sim 40$ kHz) in the disordered PC-rich domain (Figure B.4, Appendix B). By contrast, the spectrum is collapsed to a single powder pattern in the mixture with POPC (Figure B.4, left column).

An estimation of the size of domains in PDPC/PSM-d$_{31}$/chol was made from the splittings measured for the methyl groups on PSM-d$_{31}$ in the spectra at 30 °C (Table B.2, Appendix B). The difference in splitting ($\Delta v$) between the domains provides a lower limit for the lifetime of PSM-d$_{31}$ in a domain ($\tau > (2\pi\Delta v)^{-1}$), from which a domain size $r > 30$ nm was calculated ($r = \sqrt{4D\tau}$) assuming a typical value for the lateral diffusion coefficient ($D \approx 5 \times 10^{-12}$ m$^2$s$^{-1}$) taken from the literature (Lindblom & Orädd, 2009). A lower limit to domain size in the same ballpark was similarly estimated on the basis of the difference in splitting between domains measured when PDPC-d$_{31}$ ($r > 50$ nm) and when chol-d$_1$ ($r > 20$ nm) were the labeled analogs in the mixed membrane (Table B.2, Supplemental Information). This order of magnitude for the size of domains, in comparison, represents an upper limit in the equivalent mixtures containing POPC instead of PDPC. Taking the quadrupolar splitting measured for the methyl group here on PSM-d$_{31}$ ($\Delta v_r = 6.7$ kHz) in POPC/PSM-d$_{31}$/chol and previously on POPC-d$_{31}$ ($\Delta v_r = 5.1$ kHz) in POPC-d$_{31}$/eSM/chol (Williams et al., 2012) as representative of the SM-rich and PC-rich domains, respectively, an upper limit for the lifetime ($\tau < (2\pi\Delta v)^{-1}$) in a domain and corresponding domain size $r < 45$ nm were evaluated.

A propensity for polyunsaturated phospholipids to enlarge domains has been noted in other studies. Indicative of the slow exchange of lipid molecules between raft-like and non-raft domains, separate signals assigned to domains > 35 nm in radius were resolved in $^2$H NMR spectra that we recorded for 1-[$^2$H$_{31}$]palmitoyl-2-eicosapentaenoylphosphatidylcholine (PEPC-d$_{31}$) with eicosapentaenoic acid (EPA, 20:5$\Delta$) at *sn*-2 position (Calder, 2012; Lingwood & Simons, 2010; Shaikh et al., 2009; Shaikh, Wassall, et al., 2015; Wassall & Stillwell, 2008) in a mixed membrane containing eSM and chol (Williams et al., 2012). A transition from coexisting domains that are nano- to micro-scale in size on replacing 1-stearoyl-2-docosahexaenoyphosphatidylcholine (SDPC) for 1-stearoyl-2-oleoylephosphatidylcholine (SOPC) and PDPC for POPC in mixtures with SM and chol was evinced by a combination of spectroscopic and imaging techniques using probes that discriminate between liquid ordered (l$_o$) and liquid disordered (l$_d$) environments (Georgieva et al., 2015; Konyakhina & Feigenson, 2016). Coarse grain molecular dynamics (CGMD) simulations performed over a simulation time of 32 μs on a bilayer

composed of PDPC or POPC mixed with 1,2-dipalmitoylphosphatidylcholine (serving as substitute for SM) and chol (1:1:1 mol), in addition, revealed a growth of domains with the polyunsaturated phospholipid that was not apparent with its monounsaturated counterpart (K. R. Levental et al., 2016). An even greater enhancement in domain size was observed in subsequently published simulations run with 1,2-didocosahexaenoylphosphatitdylcholine (DDPC) that has DHA esterified at both *sn*-1 and -2 positions for the polyunsaturated phospholipid (Lin et al., 2016).

The formation of larger domains in the presence of polyunsaturated phospholipids is attributed here to the high disorder of PUFA chains. The segregation of chol into regions rich in SM with saturated chains that are predominantly linear in conformation is promoted because PUFA adopt a multitude of rapidly varying configurations that are incompatible with close proximity to the rigid steroid moiety (Wassall & Stillwell, 2009). High disorder and the accompanying larger molecular cross-sectional area, reduce the thickness of the bilayer for regions rich in polyunsaturated phospholipids (Stillwell, Shaikh, Zerouga, Siddiqui, & Wassall, 2005). Domains then enlarge to relieve the line tension associated with an increased hydrophobic mismatch between thicker SM-rich and thinner polyunsaturated phospholipid-rich regions (García-Sáez, Chiantia, & Schwille, 2007). In support of this scenario, that the size of domains formed in mixtures of saturated lipids and chol with unsaturated lipids depends upon the extent of unsaturation (hence degree of disorder) of the unsaturated lipid is well documented (Ackerman & Feigenson, 2015; Veatch & Keller, 2003b). A direct correlation between the size and differential in thickness of coexisting $l_o$ and $l_d$ domains was measured by SANS in mixed membranes composed of saturated 1,2-distearoylphosphatidylcholine (DSPC) and chol combined with POPC and 1,2-dioleoloylphosphatidylcholine (DOPC) in varying relative proportion (Heberle et al., 2013). As the fraction of more disordered DOPC with OA at the *sn*-1 and -2 positions was increased, the radius of domains and the mismatch in their hydrophobic thickness enlarged in a roughly linear manner. However, reservations have been expressed about generalizing this result (Bleecker, Cox, & Keller, 2016). It has been advocated that the size and stability of domains formed in lipid mixtures are strongly linked to the differential in order than thickness between them (Georgieva et al., 2015; Lin et al., 2016).

An increase in domain size due to DHA was not apparent in $^2$H NMR spectra observed in our earlier work on 1:1:1 mol mixtures of PDPE with SM and chol (Shaikh et al., 2009; Soni et al., 2008). Like in control experiments run on mixtures with POPE, only a single component was resolved in spectra collected for deuterated analogs of PDPE and SM. The spectra were interpreted in terms of fast exchange back and forth between more ordered SM-rich and less ordered PE-rich domains < 20 nm in size for both OA- and DHA-containing membranes (Soni et al., 2008). We ascribe the reduction in the size of domains with PDPE compared to PDPC to the smaller head group for PE than PC. The consequent smaller cross-sectional area for PE constrains the reorientation of lipid chains, resulting in higher order parameters and concomitantly a thicker bilayer (Kučerka et al., 2015; Lafleur, Cullis, & Bloom, 1990). Thus, regions rich in PE are closer in order and thickness to raft-like domains rich in SM and chol than the counterpart PC. The smaller PE head group also produces negative stress curvature, as demonstrated by a tendency to adopt inverted hexagonal H$_{II}$ phase (Shaikh, Cherezov, Caffrey, Stillwell, & Wassall, 2003), which can reduce line tension between domains (Kuzmin et al., 2005).

## 4.6    DHA Infiltrates Raft-like Domains

Work on model membranes established that, driven by high disorder and aversion for chol, PDPE is largely excluded from ordered raft-like domains in mixtures with SM and chol (Shaikh et al., 2004; Shaikh, Kinnun, et al., 2015; Shaikh et al., 2009; Soni et al., 2008). The implication is that DHA-containing PE indirectly exerts an influence on lipid rafts *via* changes in molecular organization of non-raft regions. Substituting PDPE for PDPC in a subsequent investigation, however, it was discovered a substantial amount of DHA-containing PC enters raft-like domains (Shaikh, Kinnun, et al., 2015; Williams et al., 2012). A differential in affinity for the sterol due to head group size was proposed to be responsible. Here it is thus inferred that PDPC, unlike PDPE, penetrates lipid rafts and directly influences their molecular organization.

$^2$H NMR spectroscopy has the ability to directly provide an estimate of the composition of lipid domains when separate signals from the lipid species in each domain are resolved. The relative integrated intensity (area) of signals from a deuterium labeled lipid in the

different domains corresponds to the relative amount of that lipid species in the domains. Here this approach was applied to the spectral components assigned to more ordered raft-like and less ordered non-raft domains that were resolved in the $^2$H NMR spectra recorded in the current work for PDPC/PSM-d$_{31}$/chol (Figure 4.3, right column) and PDPC/eSM/chol-d$_1$ (Figure B.4, right column), and in the earlier study for PDPC-d$_{31}$/eSM/chol (Williams et al., 2012).

This method of analysis is illustrated in Figure 4.4. The FTT depaked spectra presented are equivalent to spectra for a sample of single alignment oriented with the bilayer normal parallel to the direction of the magnetic field (McCabe & Wassall, 1997). They consist of a superposition of doublets, rather than of powder patterns as in a conventional FFT spectrum. The terminal methyl groups on PSM-d$_{31}$ in PDPC/PSM-d$_{31}$/chol (Figure 4.4, upper left panel) and on PDPC-d$_{31}$ in PDPC-d$_{31}$/eSM/chol (Figure 4.4, upper right panel) are responsible for the pair of doublets in the middle of the depaked spectra - the inner doublet is due to PSM-d$_{31}$ and PDPC-d$_{31}$ in the more disordered (non-raft) domain while the outer doublet is due to PSM-d$_{31}$ and PDPC-d$_{31}$ in the more ordered (raft-like) domain. Analogously, the inner and outer doublets in the depaked spectrum for PDPC/eSM/chol-d$_1$ (Figure 4.4, lower left panel) are respectively due to chol-d$_1$ in non-raft and raft-like domains. From the relative integrated intensity of the signals ascribed to the two domains, the relative amount of PSM-d$_{31}$, PDPC-d$_{31}$ and chol-d$_1$ was determined (Table B.3, Appendix B). The results are summarized in the pie charts plotted in Figure 4.4 (inset, lower right panel), which assume an approximately equivalent distribution of lipids between domains with eSM and PSM. Here it is found that the raft-like domain contains most of the total lipid - SM (28%) and chol (29%) comprise the majority with, as previously discovered (Williams et al., 2012), a significant amount of PDPC (23%). In the non-raft domain, PDPC is the major component (11%) together with lesser amounts of SM (4%) and chol (5%). Interestingly, the SM:chol ratio is nearly 1:1 mol in both domains. It is an observation consistent with high affinity between these two lipids and the existence of stoichiometric compositions at which lipids form a complex with the sterol (Lange, Tabei, Ye, & Steck, 2013).

These results reveal that, despite high disorder and aversion for chol, PDPC infiltrates SM-rich/chol-rich domains. Similar behavior has been seen in other mixtures of lipids that form raft-like domains. Like PDPC-$d_{31}$, two populations of PEPC-$d_{31}$ in mixtures with eSM and chol (1:1:1 mol) were identified in $^2$H NMR spectra obtained in earlier work (Williams et al., 2012). The amount of PEPC-$d_{31}$ (8%) in the spectral component attributed to the raft-like domain was less than PDPC-$d_{31}$. It was suggested greater disorder caused PEPC to be less compatible with infiltration into a more ordered environment. $^2$H NMR spectra consisting of a superposition of two spectral components were recorded for ternary mixtures of DOPC/*N*-stearoylsphingomyelin (SSM)/chol (1:1:1 mol) prepared with selectively deuterated analogs of the three lipids (Yasuda et al., 2015). In common with our interpretation, incorporation into raft-like and non-raft domains was deemed to be responsible. Although the distribution of SM and chol between the domains resembles that seen with PDPC, not nearly as much DOPC (10%) was found in the raft-like domain. Possible reasons include a greater mismatch in thickness for SSM vs. DOPC than for PSM vs. PDPC. SSM is thicker than PSM due to its longer amide-linked chain (stearic (18:0) as opposed to palmitic (16:0) acid), while comparable values have been published for the thickness of DOPC and PDPC bilayers (Ausili et al., 2017; Kučerka et al., 2008). The saturated *sn*-1 chain on PDPC may also pack better with the saturated chains on SM and the rigid steroid moiety of chol than the unsaturated (oleic (18:1)) chains at both *sn*-1 and -2 positions on DOPC. Coexistence of $l_o$ and $l_d$ domains was observed in SDPC/brain SM (bSM)/chol mixtures by a combination of FRET and fluorescence imaging in another study (Konyakhina & Feigenson, 2016). The mixing of SDPC with bSM/chol, it was concluded, is comparable to DOPC and POPC.

Insight into how DHA affects molecular organization within rafts, in addition, may be gleaned from the $^2$H NMR spectra where two components were resolved. PSM-$d_{31}$ in more ordered, raft-like domains is responsible for the outermost doublet ($\pm$54.2 kHz) in the depaked $^2$H NMR spectrum for PDPC/PSM-$d_{31}$/chol at 30 °C (Figure 4.4, upper left panel - see also Figure B.5, Appendix B). Several methylene groups contribute to the high intensity of this composite doublet, which we attribute to a plateau region of approximately constant order ($S_{CD} \approx 0.43$) in the upper portion of the chain (Lafleur et al., 1989). As

judged by comparison with smoothed order parameter profiles published for bilayers of PSM-d$_{31}$ mixed with just chol (Bartels et al., 2008; Bunge et al., 2008), the impact of PDPC on the raft-like environment is modest. Order in the initial plateau region of these profiles appears to asymptotically approach a limit ($S_{CD} \sim 0.45$) with increasing concentration of chol in the binary mixture that only slightly exceeds the value measured for the raft-like domain in the ternary mixture with PDPC as well as PSM-d$_{31}$ and chol. The incorporation of DOPC similarly produced minimal change in the order of SSM raft-like l$_o$ domains formed in DOPC/SSM/chol (1:1:1 mol) mixtures (Yasuda et al., 2015). Quadrupolar splittings measured with deuterated analogs of SSM selectively labeled throughout the entire amide linked chain were almost identical in the raft-like domains to measurements made on SSM/chol (1:1 mol) mixtures.

Like PDPC/PSM-d$_{31}$/chol, we ascribe the outermost signal ($\pm 42.4$ kHz) in the depaked $^2$H NMR spectrum for PDPC-d$_{31}$/eSM/chol at 30 °C to a plateau region of almost constant order ($S_{CD} \approx 0.34$) in the upper portion of the $sn$-1 chain for PDPC-d$_{31}$ within more ordered raft-like domains (Figure 4.4, upper right panel – see also Figure B.5, Appendix B). The large disparity in order ($\Delta S_{CD} \approx 0.09$) with respect to PSM-d$_{31}$ implies that PDPC taken up into a raft-like domain does not mix homogeneously with SM. A definitive explanation eludes us at present. Two possible models are depicted in Figure 5. According to one scenario, PDPC sequesters into small-localized patches ($r < 10$ nm) to reduce the unfavorable exposure of DHA chains to the high concentration of chol in the raft-like domain (Figure 4.5, top panel). These small patches would not be devoid of chol, but the amount of sterol would be lower than in the surrounding environment. The second scenario has PDPC accumulating at the perimeter of raft-like domains (Figure 4.5, lower panel). A gradient in concentration of polyunsaturated phospholipid and thickness, and thereby line tension, would be created at the boundary with the thinner non-raft regions.

## 4.7   Conclusion

The $^2$H NMR experiments on model membranes performed here demonstrate that ordered domains enriched in chol and sphingolipids (lipid rafts) are a viable target for n-3 PUFA in the plasma membrane. The observation that replacing POPC with PDPC in mixtures

with SM and chol enlarges domains supports an underlying lipid driven mechanism by which n-3 PUFA regulate the size of lipid rafts. The take up of highly disordered n-3 PUFA into phospholipids in the non-raft environment increases the differential in order relative to lipid rafts, causing the rafts to cluster together into larger domains and thereby turn on resident signaling proteins. This view is consistent with imaging studies that have shown treating cells with EPA and DHA *in vitro* or by administration of EPA/DHA to mice increases the size of regions identified as rafts (Chapkin, Wang, Fan, Lupton, & Prior, 2008; Hou, McMurray, & Chapkin, 2016; Kim et al., 2008; Rockett et al., 2012). Studies with fluorescently labeled DHA have also shown incorporation of DHA directly into liquid ordered domains (Teague, Ross, Harris, Mitchell, & Shaikh, 2012). The effects of increasing raft size have functional consequences on the localization of proteins and their signaling (Kim et al., 2008; Rockett, Melton, Harris, Bridges, & Shaikh, 2013). Future studies will need to address other long chain n-3 PUFA, particularly docosapentaenoic acid (DPA) that is the elongation product of EPA, which could modulate raft size (M. Harris, Kinnun, Kosaraju, Leng, & Wassall, 2016). Subsequent studies, furthermore, should go beyond the use of a canonical 1:1:1 mixture of lipids given that DHA is esterified into phospholipids at lower levels in the plasma membrane of cells (Stillwell & Wassall, 2003).

It is the observation here that PDPC, although highly disordered, infiltrates ordered raft-like domains in mixtures with SM and chol adds credence to the assessment made on the basis of biochemical detergent assays that n-3 PUFA are incorporated into rafts in cells. In these studies EPA and DHA were detected in detergent resistant membranes (DRM), which are purported to crudely correspond to rafts (Pathak & London, 2011), isolated from cells incubated with n-3 PUFA (Rockett et al., 2012; Turk & Chapkin, 2013). A coherent picture has yet to emerge, however, on how n-3 PUFA affect molecular organization in regions identified as rafts in cellular systems. Increased (Kim et al., 2008), as well as decreased (Zech et al., 2009), order has been described following treatment with n-3 PUFA. This apparent contradiction in outcome reflects the complexity of biological cells, where variation in the levels of other fatty acids can moderate the response. Studies of lipid bilayers open a window on the response to controlled changes in composition that can help decipher what happens in more complex, biological membranes. In the current study, a

minimal effect of DHA on order in raft-like domains was inferred from the $^2$H NMR spectra obtained for PSM-d$_{31}$ in mixtures with PDPC and chol. Sequestration of PDPC into small patches within raft-like domains is one possible scenario (Figure 4.5, top panel) that offers support for a proposal by which n-3 PUFA modify protein activity by de-clustering rafts (Shaikh, 2012).

POPC/PSM-d$_{31}$ | POPC/PSM-d$_{31}$/chol

37 °C

30 °C

23 °C

2 °C

−10 °C

37 °C

30 °C

20 °C

0 °C

−10 °C

-60  -30  0  30  60
kHz

-60  -30  0  30  60
kHz
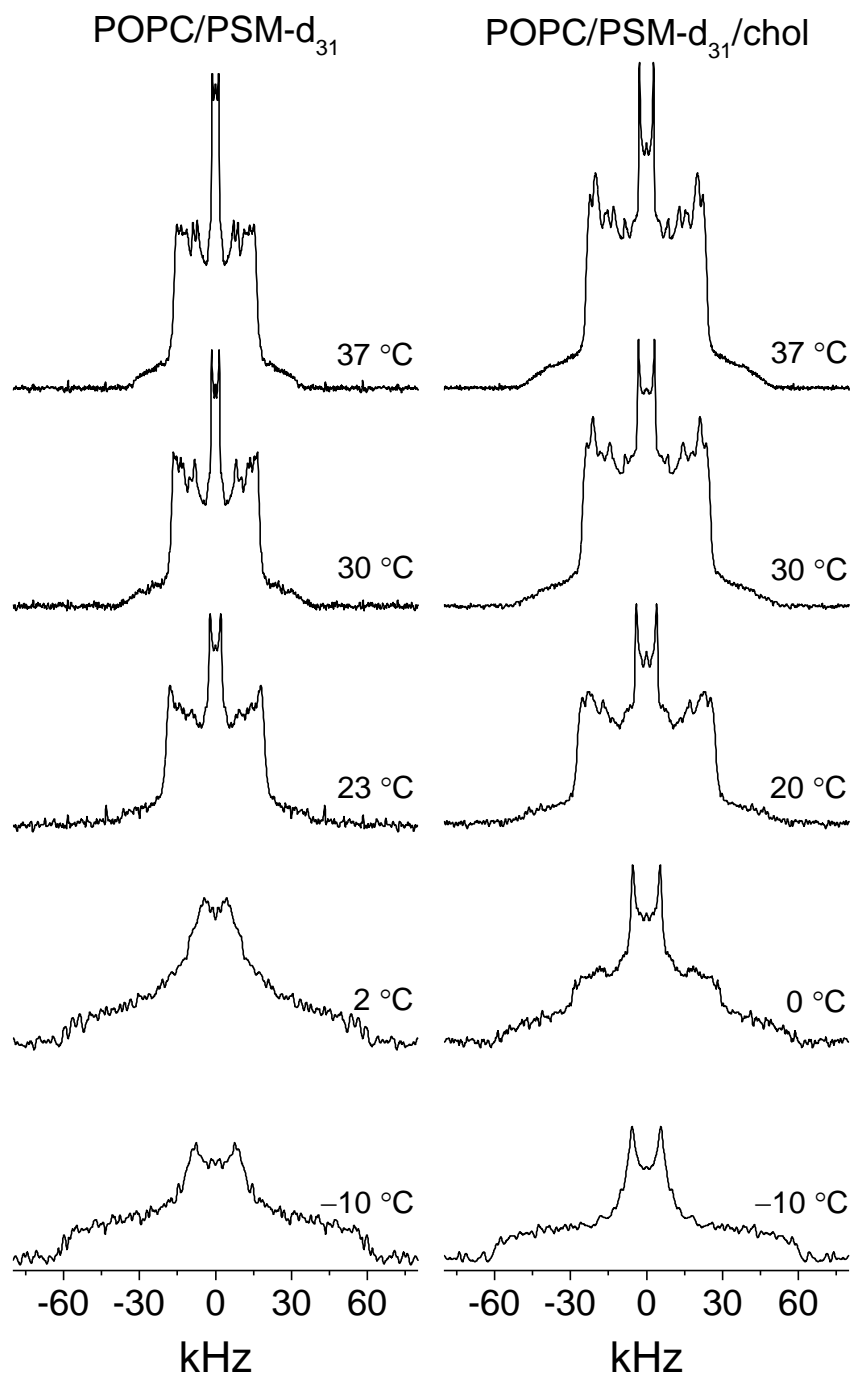
Figure 4.1: $^2$H NMR spectra for 50 wt% aqueous dispersion in 50 mM Tris buffer (pH 7.5) of POPC/PSM-d$_{31}$ (1:1 mol) (left column) and POPC/PSM-d$_{31}$/chol (1:1:1 mol) (right column). Spectra are symmetrized about the central frequency to enhance signal/noise.
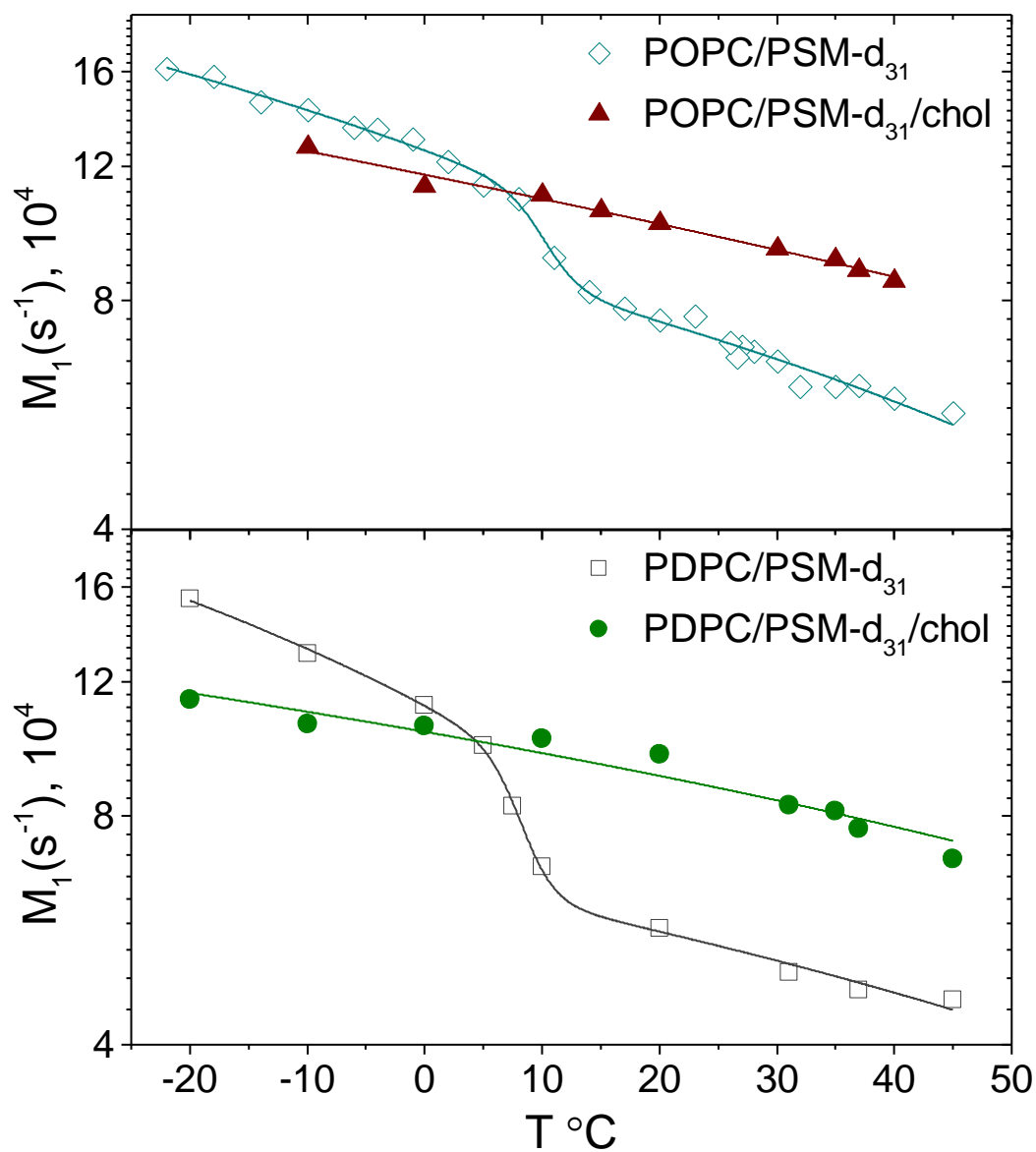
Figure 4.2: Variation of the first moment $M_1$ as a function of temperature for POPC/PSM-$d_{31}$/ (1:1 mol) ($\diamondsuit$) and POPC/PSM-$d_{31}$/chol (1:1:1 mol) ($\blacktriangle$) (top panel); and for PDPC/PSM-$d_{31}$ (1:1 mol) ($\square$) and PDPC/PSM-$d_{31}$/chol (1:1:1 mol) ($\bullet$) (bottom panel). $M_1$ is plotted logarithmically for clarity. The lines through the data are merely meant to guide the eye. They were fit with a sigmoid function modified by a slope.

PDPC/PSM-d$_{31}$ PDPC/PSM-d$_{31}$/chol
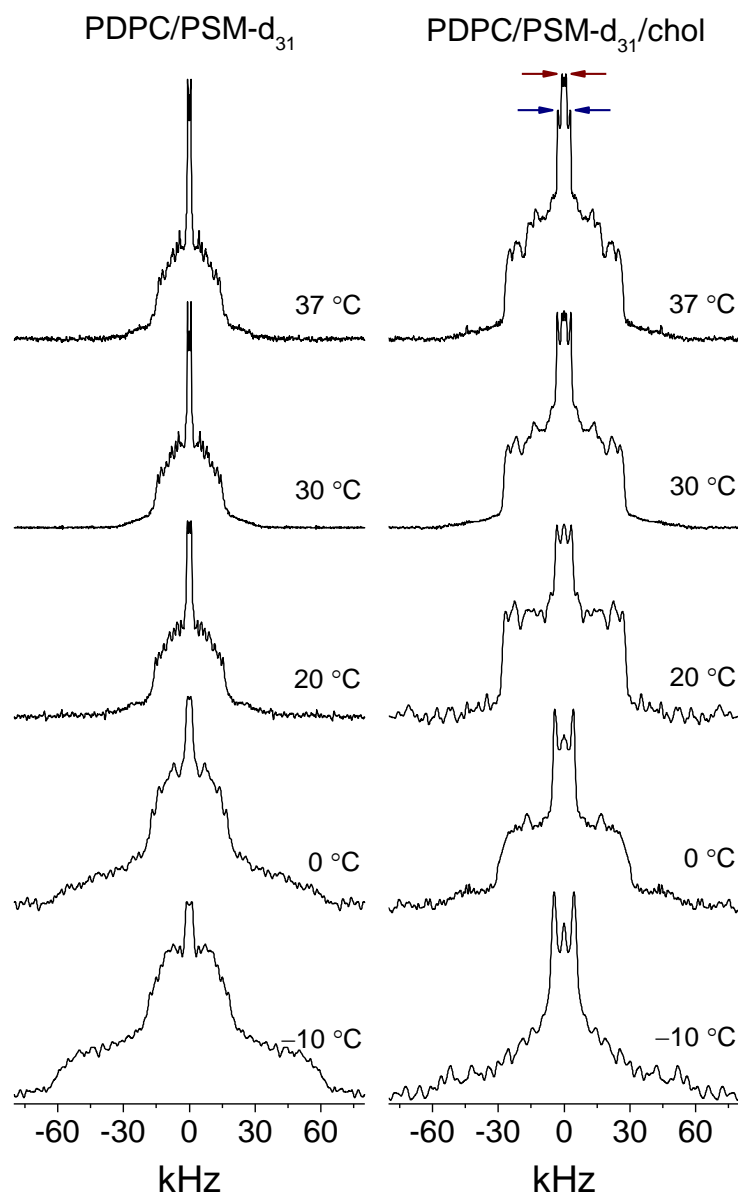


Figure 4.3: $^2$H NMR spectra for 50 wt% aqueous dispersion in 50 mM Tris buffer (pH 7.5) of PDPC/PSM-d$_{31}$ (1:1 mol) (left column) and PDPC/PSM-d$_{31}$/chol (1:1:1 mol) (right column). Spectra are symmetrized about the central frequency to enhance signal/noise. Arrows included in the spectrum for PDPC/PSM-d$_{31}$/chol at 37 °C illustrate the resolution of signals assigned to the methyl groups on PSM-d$_{31}$ in SM-rich (outer splitting) and PC-rich (inner splitting) domains. Spectra are symmetrized about the central frequency to enhance signal/noise.
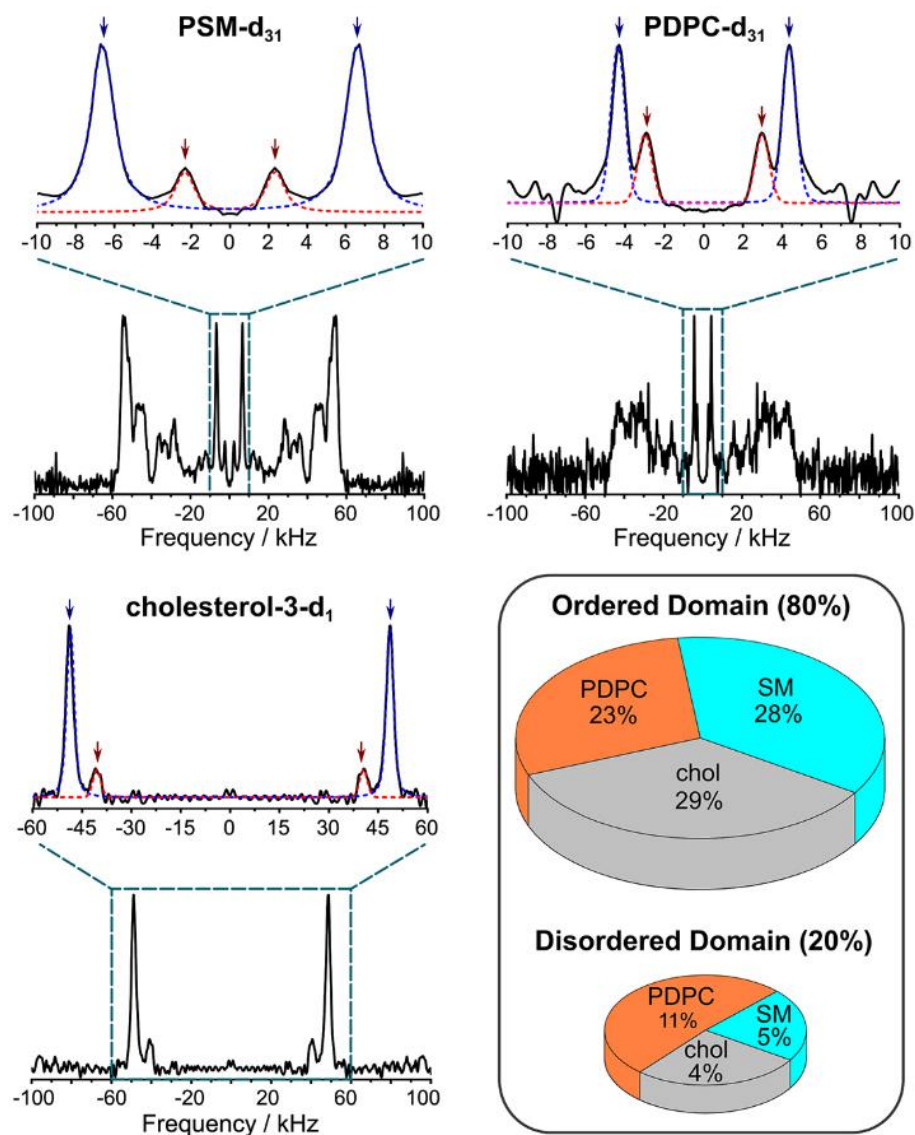
Figure 4.4: $^2$H NMR spectra at 30 °C for PDPC/PSM-d$_{31}$/chol (upper left panel), PDPC-d$_{31}$/eSM/chol (1:1:1 mol) (upper right panel) and PDPC/eSM/chol-d$_1$ (lower left panel) (1:1:1 mol). Depaked spectra, together with an expansion of the central region in each case (above), are shown. The arrows designate pairs of signals assigned to the terminal methyl group on PSM-d$_{31}$ and PDPC-d$_{31}$ and to the 3α group on chol-d$_1$ in more ordered SM-rich/chol-rich (outer splitting) and more disordered PDPC-rich/chol-poor (inner splitting) domains. A Voigt lineshape (dashed lines) was fit to the peaks. The data for the samples containing PDPC-d$_{31}$ are taken from Williams et al. (Williams et al., 2012). Spectra are symmetrized about the central frequency to enhance signal/noise. Pie charts depicting the composition of domains obtained from the fit of the peaks in the spectra are shown in the inset (lower right). The percentages are the amount of each lipid species in a domain with respect to the total amount of lipid in the mixed membrane. As shown, the majority of each lipid species resides within the more ordered (raft-like) domain. In total, 80% of the lipids reside within this domain. The reader is directed to Table B.3, Appendix B for the relative amount of each lipid in raft-like vs. non-raft domains.
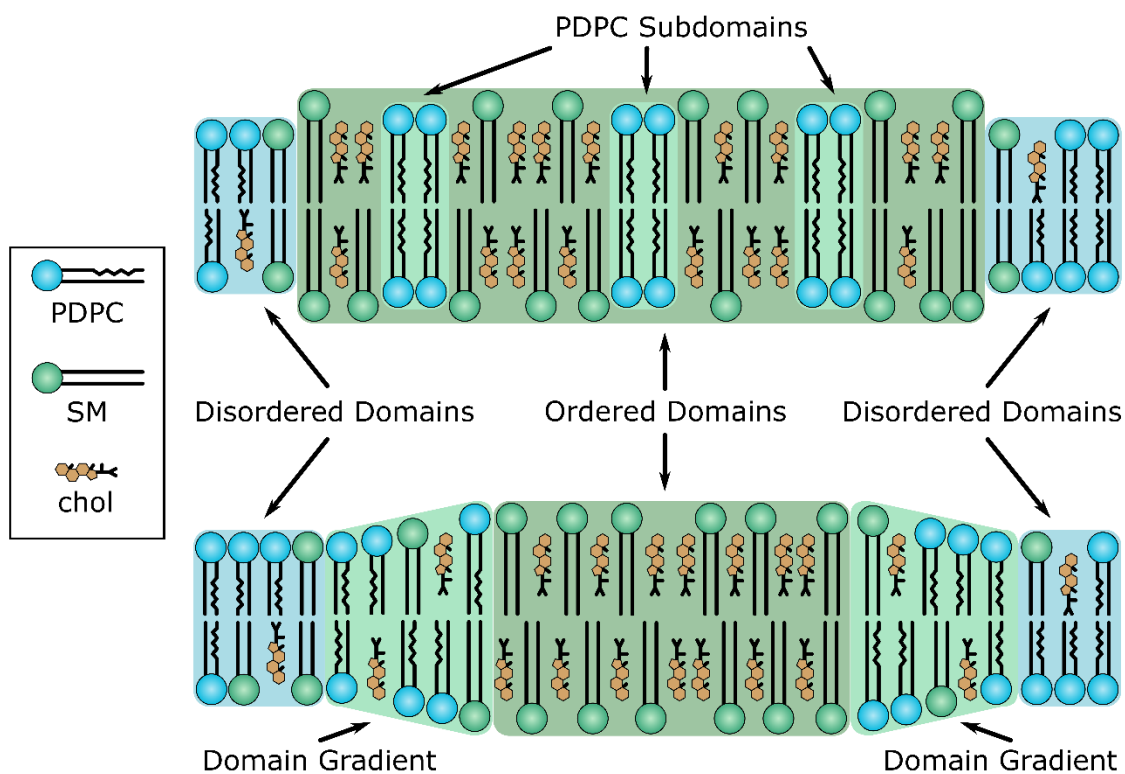
Figure 4.5: A model depicting two possible scenarios for the arrangement of PDPC taken up into a SM-rich/chol-rich ordered domain. Top - PDPC molecules cluster together in small subdomains within the bigger raft-like, SM-rich/chol-rich domain. Bottom - PDPC molecules accumulate at the edge of the raft-like domain, creating a gradient in concentration and thickness at the border with the thinner PDPC-rich/chol-poor region.

# CHAPTER 5.    CONCLUSIONS

The main focus of the thesis was characterizing the interaction of PUFA (in the form of DHA) with the raft-like domains (containing sphingomyelin and cholesterol) of model membranes. The major technique used here was solid-state $^2$H NMR spectroscopy, in which custom software was developed for. This chapter will summarize the work presented and suggest future directions.

## 5.1    $^2$H NMR Spectroscopy Data Processing and Analysis

For bulk materials in the solid state, broadline NMR spectroscopy extracts details of molecular orientation and anisotropy of molecular reorientation by analysis of the lineshape. This technique allows for a direct measurements of order and dynamics in solids and gels which has been extensively applied to biological materials (Kinnun et al., 2015) and non-biological materials (Kinnun et al., 2013) as described in Chapter 2. It is a niche area of NMR for which standard software often lack necessary features.

Both EchoNMR processor and fitter developed here, collectively referred to as EchoNMR tools as described in Chapter 3, process data obtained by broadline NMR spectroscopy. These tools have been designed with a focus on user usability and the open-source mindset, to allow for quick processing of data and flexibility. This is achieved in the MATLAB® (Mathworks) programming environment which allows for the development of the graphical user interfaces and runs as an interpreter which allows the code to be open-source. The collection of solid state $^2$H NMR spectra from model membranes relies on using the solid echo NMR pulse sequence to avoid phase distortion due to the receiver dead time. EchoNMR processor facilitates the transformation of the signal recorded in the time domain by this sequence to a broadline spectrum. This includes many automated routines in EchoNMR processor to help eliminate human guess work in data processing. There is then the option in EchoNMR fitter to make corrections (e.g. for the pulse width) and to perform lineshape fits to extract spectral parameters.

## 5.2    The Effect of PUFA on Raft Domain Formation

Docosahexaenoic acid (DHA) is an omega-3 polyunsaturated fatty acid (n-3 PUFA) that relieves the symptoms of a wide variety of chronic inflammatory disorders. As yet the structural mechanism is not completely understood. However, studies suggest it may be membrane mediated (Rockett et al., 2013; Rockett et al., 2012). Using protein-free model membranes of controlled composition, this research was on the plasma membrane as a site of action.

The molecular organization of $[^2H_{31}]$-*N*-palmitoylsphingomyelin (PSM-$d_{31}$) mixed with 1-palmitoyl-2-docosahexaenoylphosphatylcholine (PDPC) or 1-palmitoyl-2-oleoylphosphatidylcholine (POPC), as a monounsaturated control, and cholesterol (chol) (1:1:1 mol) was examined in a model membrane by solid state $^2H$ NMR spectroscopy. The spectra were analyzed in terms of segregation into ordered SM-rich/chol-rich (raft-like) and disordered PC-rich/chol-poor (non-raft) domains that are nanoscale in size. Spectra that are single-component, attributed to fast exchange between domains ($r < 45$ nm), for PSM-$d_{31}$ mixed with POPC and chol become two-component, attributed to slow exchange between domains ($r > 30$ nm), for PSM-$d_{31}$ mixed with PDPC and chol. The appearance of two spectral components suggests an increase in the size of domains when POPC was replaced by PDPC. Thus, the interpretation here agrees with the proposal that PUFA can increase the size of raft domains.

Determination of domain composition identifies the infiltration of raft-like domains by DHA. The resolution of separate signals from PSM-$d_{31}$, and correspondingly from $[3\alpha$-$^2H_1]$cholesterol (chol-$d_1$) and 1-$[^2H_{31}]$palmitoyl-2-docosahexaenoylphosphatidylcholine (PDPC-$d_{31}$), in raft-like and non-raft domains enabled the determination of the composition of the domains in the PDPC-containing membrane. Most of the lipid (28% SM, 29% chol and 23% PDPC with respect to total lipid at 30 °C) was found in the raft-like domain. Despite substantial infiltration of PDPC into raft-like domains, there appears to be minimal effect on the order of SM implying the existence of internal structure that limits contact between SM and PDPC. The likely culprit is an of DHA aversion for cholesterol. Two scenarios arise from this observation, where PDPC is either sequestered in subdomains

within the raft or in an annulus around the raft-like domain. It is my opinion that it is improbable that the area of an annulus the domain would be large enough such that the diffusion of PDPC between the non-raft domain and the annulus would be slow enough to be observable with $^2$H NMR spectroscopy. Thus it is more probable that the ordered component observed for PDPC is due to PDPC sub-domains "lost" within the large raft-like domain. These results suggest a significant refinement to the model by which DHA regulate the architecture of ordered, sphingolipid-chol-enriched domains (rafts) in membranes.

## 5.3   NMR Software Development

The software developed here has focused on quickly processing and analyzing anisotropic lineshapes produced by one-dimensional NMR spectroscopy. The rapid nature of the data processing is partially due to the rapid weighted-FFT dePaking algorithm (McCabe & Wassall, 1997). Because this technique is almost as fast as a standard FFT it could have potential beyond one dimensional experiments. Multidimensional NMR spectroscopy arises when pulse sequences have multiple time parameters. By default, there is always the direct time parameter which is the time domain of the FID. However, the solid echo pulse experiment (discussed in Chapter 3) has an additional time parameter, the inter pulse delay, which can be referred to as the indirect dimension. If multiple FID are recorded with sequential increments in the indirect dimension, both the FID and then the indirect dimension can be fast Fourier transformed to yield a two dimensional spectrum. Traditionally multidimensional NMR spectroscopy has found wide-application in samples in solution form, which has allowed the structural and dynamical determination of many molecules and compounds (Palmer & Dinshaw, 2002; Shampo et al., 2012). Until the advent of magic angle spinning NMR spectroscopy, multidimensional techniques have been lacking for samples in the solid state. This is due to the incomplete motional averaging in solids producing broad lineshapes that can be difficult to interpret, especially in multiple dimensions. Magic angle spinning is one way to remedy this, which narrows the broadened lineshape.

A less utilized technique is to enhance the spectral resolution via dePaking. This has not been traditionally used as it has been computationally intensive in a single dimension, which becomes significantly worse in multiple dimensions. However, the development of the weighted-FFT algorithm has drastically reduced the computation required (McCabe & Wassall, 1997). This allows the technique of dePaking to be used in multiple dimensions, especially for axially symmetric spectra which is produced in $^2$H NMR spectroscopy. In some ways a dePaking technique has already been used to observe the relaxation of specific spectral components by Brown et al. (Brown, Thurmond, Dodd, Otten, & Beyer, 2002), by plotting dePaked spectra as a time series to resolve site-dependent relaxation. However, the authors used a more-intensive dePaking algorithm and were only able to have a few time points. With the use of the more rapid dePaking algorithm, it is quicker to dePake along the direct time domain, which can then be traditionally fast Fourier transformed along the indirect time domain, and thus generate a true two-dimensional spectrum. If paired with pulse sequences, such as ones used in correlation spectroscopy (Levitt, 2008), this could yield additional structural parameters (due to correlations in the second dimension) along with the dynamical parameters provided by the order parameters. As for all new techniques, there are possible technical limitations to overcome. First, it is unclear the exact effect of dePaking on partially relaxed spectra which are often produced in multidimensional NMR spectroscopy. Partially-relaxed spectra were dePaked by the aforementioned work by Brown et al. (Brown et al., 2002) with little detriment. This could be due to the many dePaking techniques being sensitive primarily to the sharp components produced by perpendicular orientations of the labeled sample (McCabe & Wassall, 1997) and thus potentially insensitive to the exact features of the rest of the powder pattern which may be distorted. Another technical limitation is the appearance of artifacts at twice the frequency of observed peaks. As these artifacts are due to the partial derivative of the weighted-FFT technique detecting the shoulders of powder patterns, it is possible they could exhibit correlations in the second dimension. A user of the technique would have to be aware of this as it could result in false-peaks.

### 5.4    Future Directions of PUFA and Raft Research

The size and biological role of raft-domains continues to be discussed and debated (I. Levental & Veatch, 2016), however, it is of general consensus that the membrane is laterally inhomogeneous at some scale. Further the origin of this inhomogeneity is also under debate with the two prime candidates for a lipid-driven mechanism being thickness mismatch or difference in order. Theoretically thickness mismatch produces curvature strain, thus line tension, at domain boundaries (Kuzmin et al., 2005) and there has been experimental evidence showing that increased thickness mismatch increases domain size (Heberle et al., 2013; Williams et al., 2012). Although there has been experimental evidence showing that the difference in order, due to cholesterol interactions, can also result in domain formation (K. R. Levental et al., 2016; Veatch & Keller, 2003b) there has been less application of theory in such cases. There may be an entropic cost, thus potential line tension, for disordered lipids to reside near cholesterol, however it is difficult to calculate. One potential way to calculate this is to estimate the average length and depth of cholesterol perpendicular to the membrane normal, and then estimate the entropic cost of extending the length of a lipid chain, thus reducing the number of configurations, to match this conformation. The difficulty in this is choosing an appropriate model to estimate the entropy. Lipids are not entropic springs, rather they are under lateral pressure which produces orienting potential. There has been work in modeling this potential (Petrache et al., 2000) which continues to be tested (Kinnun et al., 2015) that could potentially be used in estimating this entropic cost. However, modeling has typically been focused on saturated chains rather than unsaturated chains. Thus it may be advantageous to use molecular dynamics simulations to aid in determining a simple theory in the prediction of domain formation in the cases of cholesterol.

It is becoming clear that PUFA fatty acids increase membrane inhomogeneity. Although the focus here was on the raft-like domain and the effect of DHA, there are other n−3 PUFAs found in foods, which may have biological roles. For example, eicosapentaenoic acid (EPA, 20:5) is also common in fish oils alongside DHA. Previously it was discovered that EPA has a greater propensity than DHA to promote raft-like domains (Williams et al., 2012). Here the reduced chain length of EPA when compared to DHA, presumably reduces

the lipid order (Williams et al., 2012) thus producing a thinner lipid and theoretically increases the line tension between domains. However, future experiments would need to confirm this. Interestingly EPA, within cells often converts to docosapentaenoic acid (DPA, 22:5) (M. Harris et al., 2016), which increases the chain length of the fatty acid to be equivalent to DHA albeit with one less double bond. A recent study has shown order to be approximately equal to or slightly greater in DPA- than DHA-containing bilayers (M. Harris et al., 2016). This means that DPA could affect rafts similar to DHA. Unfortunately, studies are lacking for DPA on its effects on raft-like domains, thus there are plenty of opportunities to study phospholipids containing this n-3 PUFA and its biological roles. In particular, the technique of $^2$H NMR spectroscopy used here would be equally well-suited in studying the effect of DPA-containing lipids on raft-like domains.

# APPENDIX A. SUPPLEMENTAL MATERIAL FOR LINESHAPE SIMULATION

Relaxation can be orientationally dependent, which manifests as a frequency dependent decay (Domenici, 2009; Morrison & Bloom, 1993, 1994; Separovic & Cornell, 2000). For this reason, signals far away from the center-frequency of the spectrum can appear to have lower amplitudes in the frequency domain. The relaxation rate is often proportional to square of the frequency (Domenici, 2009; Morrison & Bloom, 1993). To handle this, one component of the signal observed can be assumed to be a cosine decayed by an amplitude function, $A(t)$:

$$S(t) = A(t)P(t) \tag{A.1}$$

where $P(t) = cos(\omega t)$ is the sinusoidal signal. The amplitude function is assumed to be a Gaussian decay:

$$A(t) = A_0 exp(-Gt^2) \tag{A.2}$$

where $A_0$ is the initial amplitude and $G$ is the corresponding Gaussian relaxation rate (units of $1/s^2$). This type of decay is seen in standard compounds such as perdeuterated hexamethylbenzene (hexamethylbenzene-$d_{18}$ obtained from Sigma Aldrich, St. Louis) in powder form as shown in Figure A.2. For this sample a Bruker AMX-300 spectrometer (Kinnun et al., 2013) with a 7.05 T superconducting magnet (Oxford Instruments, Osney Mead, UK) was used. Keep in mind that relaxation still occurs before the echo and after the last pulse, which I denote by the time $t_0$ and is equivalent to the interpulse delay, and modifies equation A.2 to become:

$$A(t) = exp(-G(t + t_0)^2) \tag{A.3}$$

This expands to:

$$A(t) = exp(-Gt^2)exp(-2Gt_0t)exp(-Gt_0^2) \tag{A.4}$$

where the first term, $exp(-Gt^2)$, is the expected Gaussian decay and the second term, $exp(-2Gt_0t)$, is an exponential decay which becomes more relevant at longer times until acquisition, $t_0$. The effect of this decay on the observed spectrum is better understood in the Fourier space. Inserting equation A.4 into equation A.1 and performing a Fourier transform ($s(\omega) = ft[A(t)P(t)]$) yields:

$$s(\omega) = \left[ \frac{exp\left(-\frac{\omega^2}{4G}\right)}{\sqrt{2G}} \right] \otimes \left[ \frac{2Gt_0}{\pi((2Gt_0)^2 + \omega^2)} \right] \otimes [exp(-Gt_0{}^2)p(\omega)] \qquad (A.5)$$

where $\otimes$ indicates a frequency-dependent convolution. The first two terms broaden the spectrum in the Fourier space, however the last term, $exp(-Gt_0{}^2)$, modifies the amplitude of the spectrum, $p(\omega)$. This last term has the potential of distorting the observed potential.

Evidence, as shown in Figure A.2 (right bottom), suggests the Gaussian relaxation term, $G$, should be frequency dependent which distorts the observed spectra according to equation A.6. Given the evidence that these rates depend on the square of the frequency, I assume the Gaussian relaxation rate to take the form of:

$$G = R_0{}^2 + (\omega R_\omega)^2 \qquad (A.6)$$

where $R_0$ is the frequency-independent relaxation rate (units of $rad/s$) and $R_\omega$ is the frequency-dependent relaxation rate (unitless due to the presence $\omega$), which is typically referred to as a square-law dependence. Given equation A.6, the last term in equation A.5 becomes:

$$exp(-Gt_0{}^2)p(\omega) = exp\left(-R_0{}^2t_0{}^2\right)exp(-(\omega R_\omega)^2t_0{}^2)p(\omega) \qquad (A.7)$$

where the first term, $exp\left(-R_0{}^2t_0{}^2\right)$, is the overall reduction of the spectrum, $p(\omega)$, and the second term, $exp(-(\omega R_\omega)^2t_0{}^2)$, distorts the spectrum by a Gaussian lineshape. EchoNMR fitter implements equation A.7 with A.5 via a frequency-dependent convolution process which distorts the lineshape (as shown in equation A.7) but also includes the frequency-dependent line-broadening that results. An example of this type of fit is shown in Figure A.3.
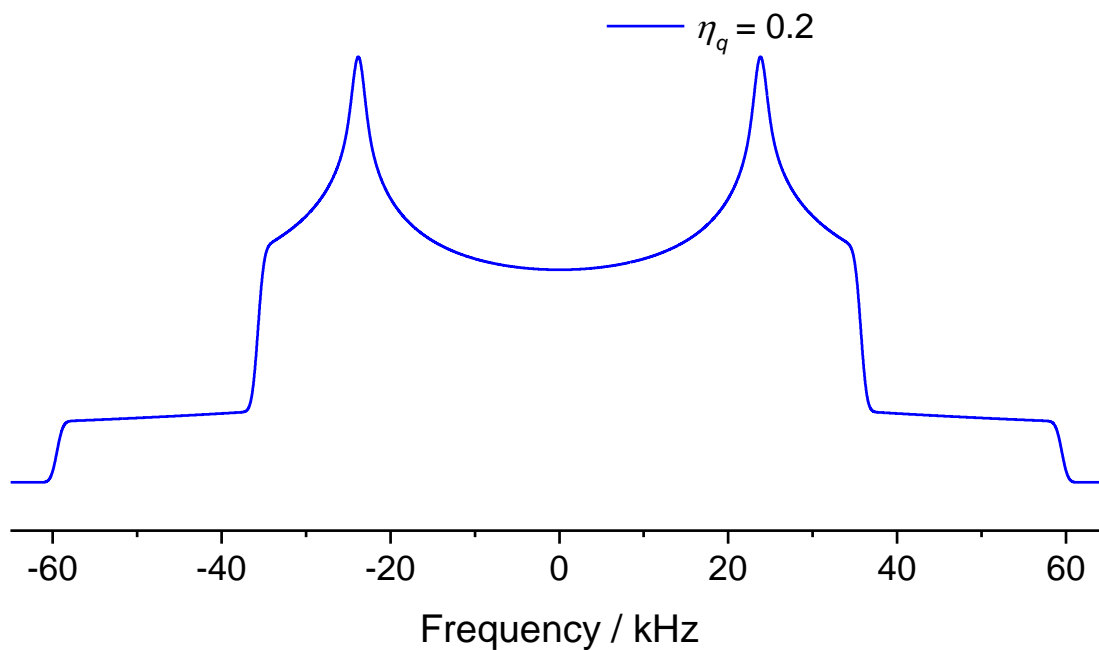
Figure A.1: EchoNMR fitter is capable of simulating, and capable of fitting, asymmetric powder patterns. From table 2.1, the asymmetry parameter is derived in terms of the electric field gradients as $\eta = \sqrt{2/3}\left(V_{yy}^{\text{PAS}} - V_{xx}^{\text{PAS}}\right)/V_{zz}^{\text{PAS}}$. Here is a sample simulation of an asymmetric powder pattern with an asymmetry parameter of 0.20. In axially-symmetric powder patterns this parameter is zero.
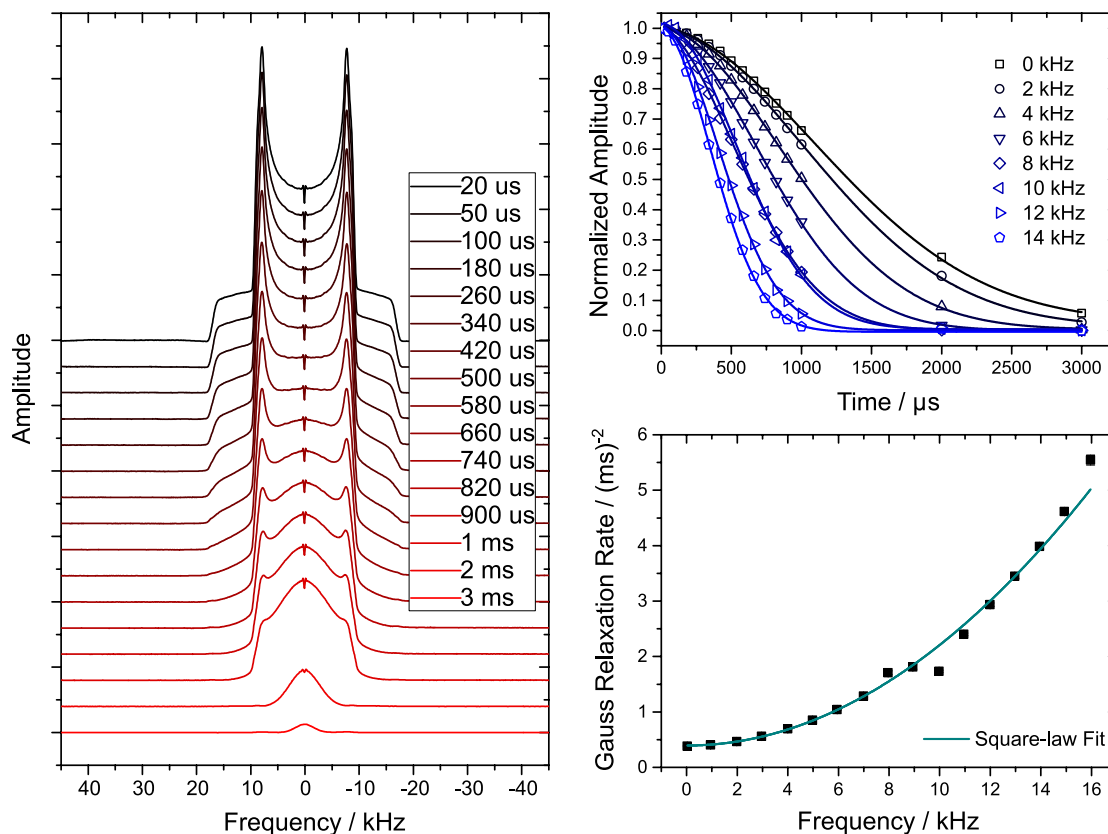
Figure A.2: A solid echo pulse sequence was performed on powder hexamethylbenzene-$d_{18}$ with varying interpulse delays. The resulting spectra obtained after fast Fourier transform from the echo peak is shown on the left, with the interpulse delay given in the inset. For long interpulse delays the spectrum becomes distorted due to frequency-dependent relaxation, which diminishes the shoulders. The amplitude of the spectra, as a function of interpulse delay, decays as a Gaussian which is shown in the right-top (the amplitude has been normalized). The Gaussian relaxation (decay rate) depends on the square of the frequency (right bottom) which is referred to as a square law. Near the theoretical singularity, ~9 kHz, the uncertainty increases as the broadened peak affects neighboring amplitudes. This likewise happens for the edges of the spectrum.
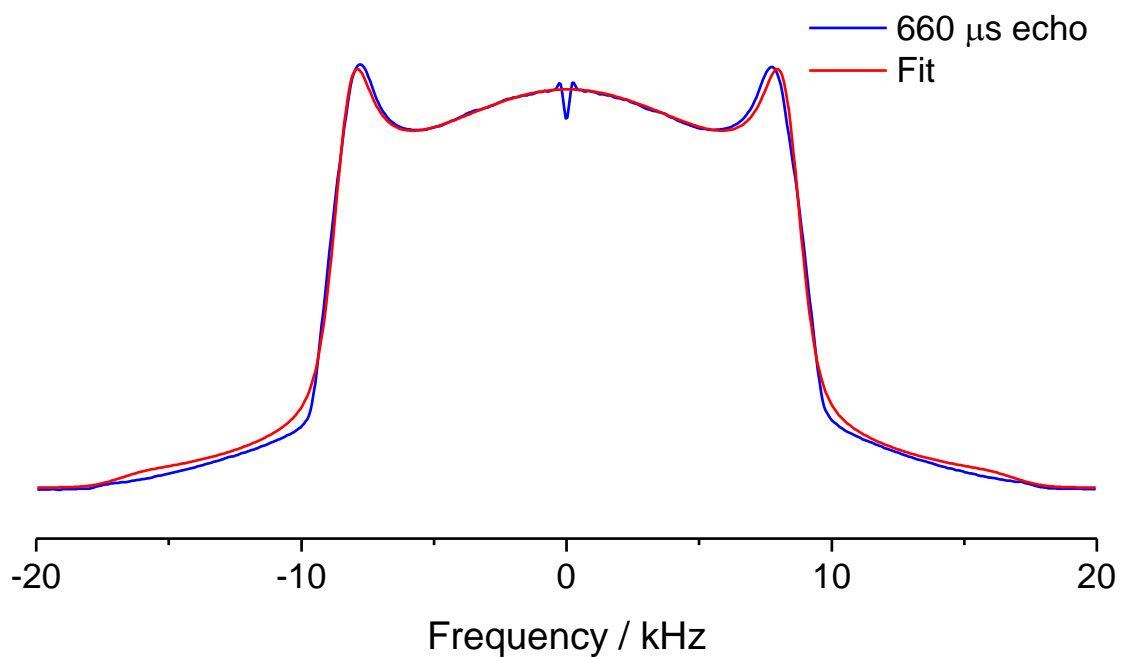
Figure A.3: EchoNMR fitter can fit lineshapes which are distorted due to pulse effects and relaxation effects. A sample spectrum of powder hexamethylbenzene-d$_{18}$ recorded using a solid echo pulse sequence with an interpulse delay of 660 μs is shown here to illustrate diminished shoulders due to relaxation effects.

# APPENDIX B. SUPPLEMENTAL MATERIAL FOR THE EFFECT OF DHA ON RAFT DOMAINS

Table B.1: Average order parameters $\bar{S}_{CD}$ derived from $^2$H NMR spectra for POPC/PSM-$d_{31}$ and POPC-$d_{31}$/eSM in 1:1 mol mixtures and in 1:1:1 mol mixtures with chol, and for PDPC/PSM-$d_{31}$ and PDPC-$d_{31}$/eSM in 1:1 mol mixtures and 1:1:1 mol mixtures with chol at 37 ºC. The values for samples prepared with POPC-$d_{31}$ and PDPC-$d_{31}$ are taken from Williams et al. (Williams et al., 2012). [a]Values are comparable in magnitude to average order parameters published for POPC/PSM-$d_{31}$ and POPC-$d_{31}$/PSM (1:1 mol) (Bunge et al., 2008).

| Membrane composition | $\bar{S}_{CD}$ | |
|---|---|---|
| | No cholesterol | With cholesterol |
| POPC /PSM-$d_{31}$ | 0.203[a] | 0.288 |
| POPC-$d_{31}$/eSM | 0.137[a] | 0.231 |
| PDPC /PSM-$d_{31}$ | 0.155 | 0.253 |
| PDPC-$d_{31}$/eSM | 0.122 | 0.192 |

Table B.2: Quadrupolar splitting at 30 °C of the terminal methyl peaks on PSM-d$_{31}$ and PDPC-d$_{31}$ and of the 3α site on chol-d$_1$ in each domain for the PDPC/SM/chol (1:1:1) mixture. These values were measured from the depaked spectra plotted in Figure 4.4 and correspond to the frequency of the respective signals (indicated by arrows). They were used to estimate a lower bound for the lifetime ($\tau > 1/2\pi\Delta\nu$) within domains and for the size ($r = \sqrt{4D\tau}$) of the domains. The values for PDPC-d$_{31}$ are taken from Williams et al. (Williams et al., 2012).

| Lipid | Disordered Peak $\Delta\nu_r$ (kHz) | Ordered Peak $\Delta\nu_r$ (kHz) | $\Delta\nu$ (kHz) | $\tau$ (µs) |
|---|---|---|---|---|
| PSM | 2.3 | 6.6 | 4.3 | >37.2 |
| PDPC | 3.0 | 4.4 | 1.4 | >115 |
| Cholesterol | 40.5 | 48.6 | 8.1 | >19.8 |
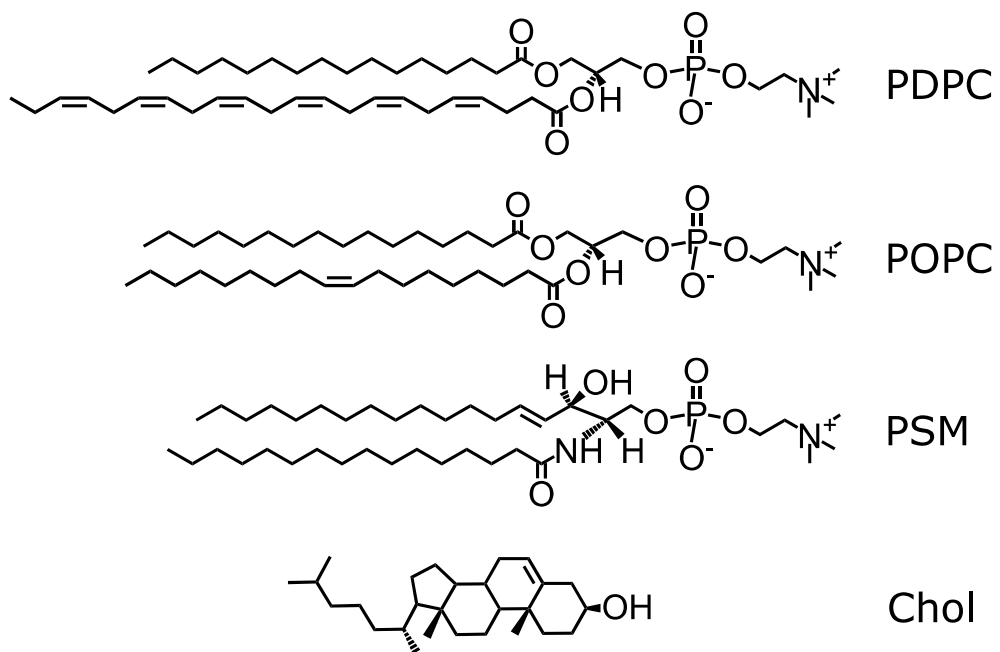
Figure B.1: Molecular structure of PDPC, POPC, PSM and chol.
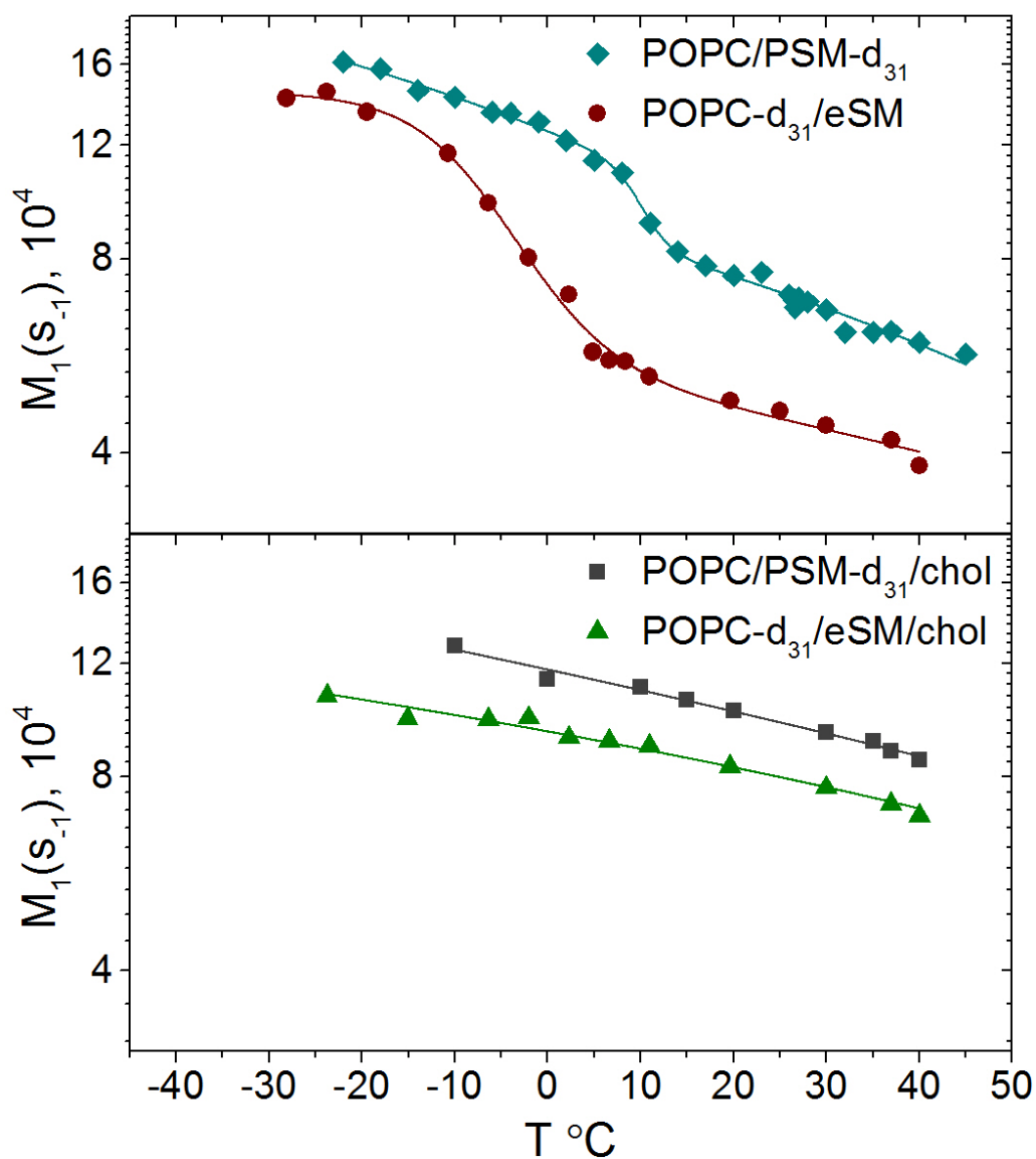
Figure B.2: A comparison of the variation of the first moment $M_1$ as a function of temperature for POPC/PSM-$d_{31}$ (1:1 mol) (♦) and POPC-$d_{31}$/eSM/chol (1:1:1 mol) (●) (top panel); and for POPC/PSM-$d_{31}$ (1:1 mol) (■) and POPC-$d_{31}$/eSM/chol (1:1:1 mol) (▲) (bottom panel). $M_1$ is plotted logarithmically for clarity. The data for the samples containing POPC-$d_{31}$ are taken from Williams et al. (Williams et al., 2012).
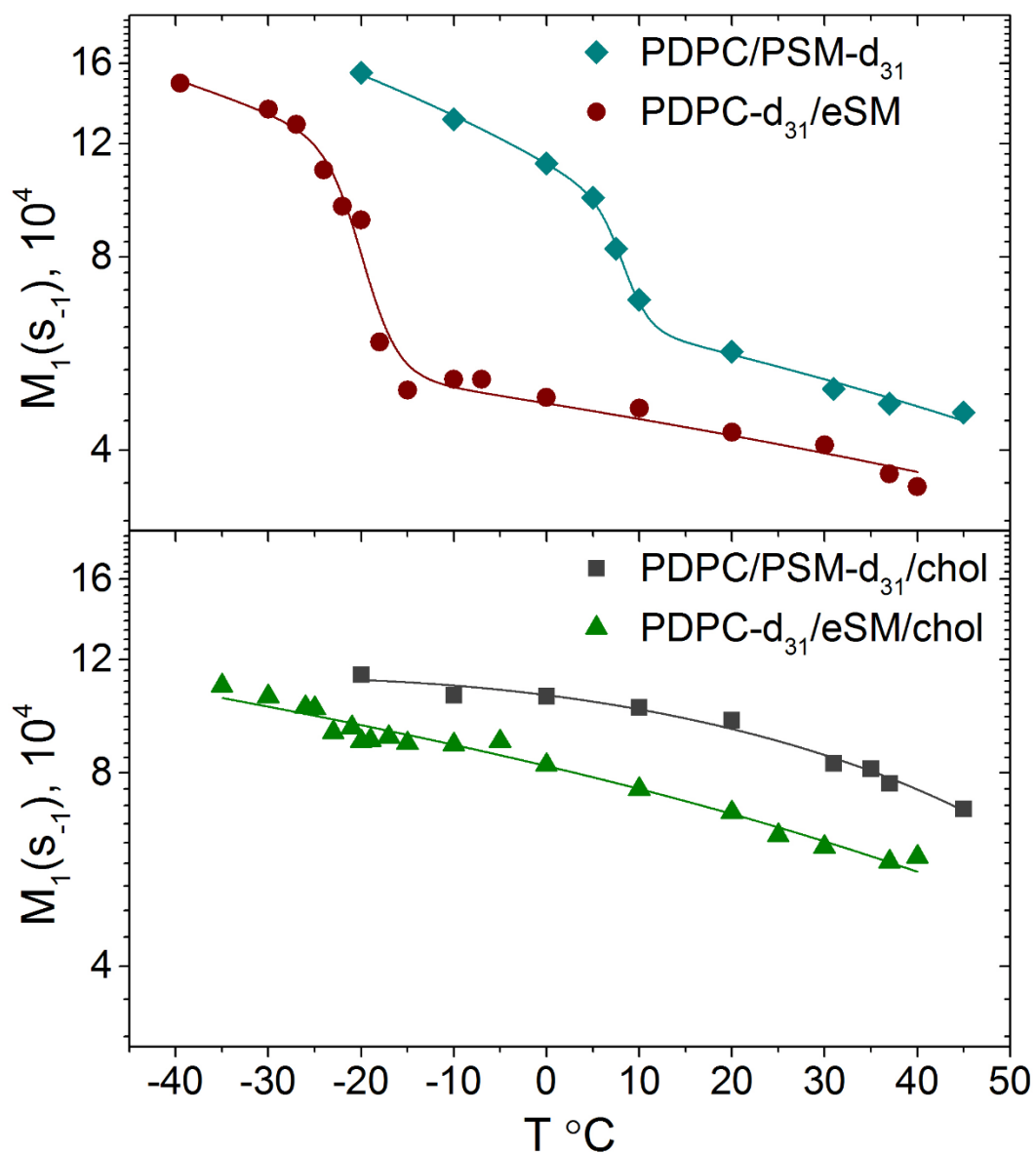
Figure B.3: A comparison of the variation of the first moment $M_1$ as a function of temperature for PDPC/PSM-$d_{31}$ (1:1 mol) (◆) and PDPC-$d_{31}$/eSM/chol (1:1:1 mol) (●) (top panel); and for PDPC/PSM-$d_{31}$ (1:1 mol) (■) and PDPC-$d_{31}$/eSM/chol (1:1:1 mol) (▲) (bottom panel). $M_1$ is plotted logarithmically for clarity. The data for the samples containing PDPC-$d_{31}$ are taken from Williams et al. (Williams et al., 2012).
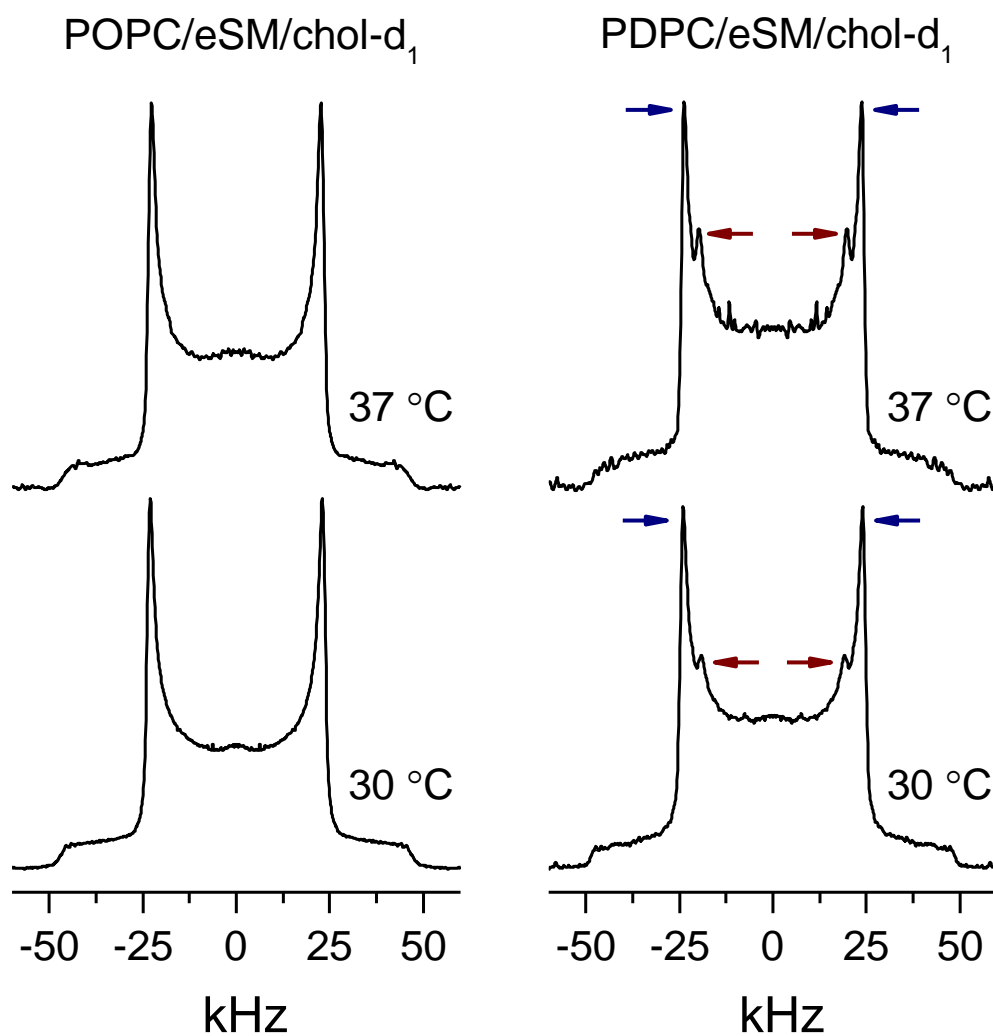
Figure B.4: $^2$H NMR spectra for 50 wt% aqueous dispersion in 50 mM Tris buffer (pH 7.5) of POPC/eSM/chol-d$_1$ (1:1:1 mol) (left column) and PDPC/eSM/chol-d$_1$ (1:1:1 mol) (right column). Spectra are symmetrized about the central frequency to enhance signal/noise. Arrows included in the spectra for PDPC/eSM/chol-d$_1$ illustrate the resolution of signals assigned to the 3α group on chol-d$_1$ in SM-rich (outer splitting) and PC-rich (inner splitting) domains. Spectra are symmetrized about the central frequency to enhance signal/noise.
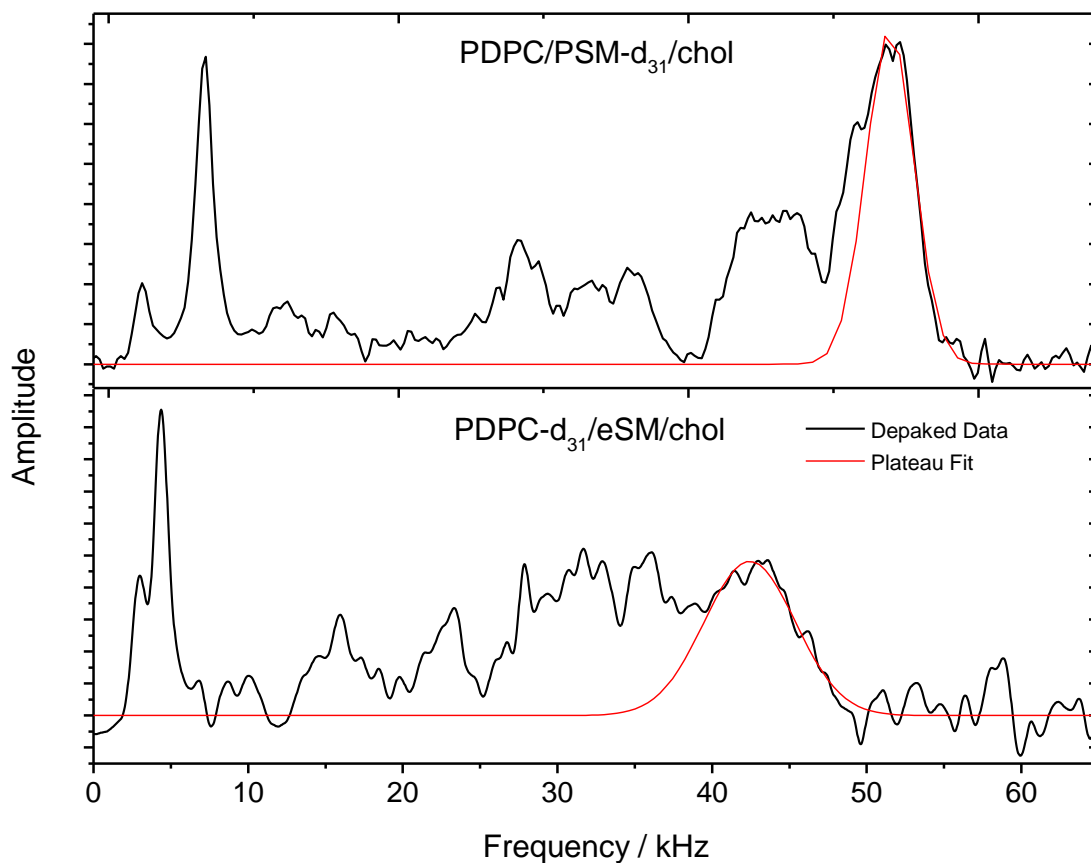
Figure B.5: $^2$H NMR spectra for 50 wt% aqueous dispersion in 50 mM Tris buffer (pH 7.5) of POPC/eSM/chol-d$_1$ (1:1:1 mol) (left column) and PDPC/eSM/chol-d$_1$ (1:1:1 mol) (right column). Spectra are symmetrized about the central frequency to enhance signal/noise. Arrows included in the spectra for PDPC/eSM/chol-d$_1$ illustrate the resolution of signals assigned to the 3α group on chol-d$_1$ in SM-rich (outer splitting) and PC-rich (inner splitting) domains. Spectra are symmetrized about the central frequency to enhance signal/noise.

# REFERENCES

Abbott, S. K., Else, P. L., Atkins, T. A., & Hulbert, A. J. (2012). Fatty acid composition of membrane bilayers: Importance of diet polyunsaturated fat balance. *Biochim. Biophys. Acta, 1818*(5), 1309–1317. doi:10.1016/j.bbamem.2012.01.011

Abragam, A. (1961). *The Principles of Nuclear Magnetism*. London: Oxford University Press.

Ackerman, D. G., & Feigenson, G. W. (2015). Lipid bilayers: clusters, domains and phases. *Essays Biochem., 57*, 33-42.

Alberts, B., Johnson, A., Lewis, J., Raff, M., Roberts, K., & Walter, P. (2002). *Molecular Biology of the Cell* (4th ed.). New York: Garland Science.

Almeida, P. F. F., Pokorny, A., & Hinderliter, A. (2005). Themodynamics of membrane domains. *Biochim. Biophys. Acta, 1720*, 1–13.

Ausili, A., de Godos, A. M., Torrecillas, A., Aranda, F. J., Corbalán-García, S., & Gómez-Fernández, J. C. (2017). The vertical location of α-tocopherol in phosphatidylcholine membranes is not altered as a function of the degree of unsaturation of the fatty acyl chains. *Phys. Chem. Chem. Phys., 19*, 6731-6742.

Aussenac, F. M., Tavares, M., & Dufourc, E. J. (2003). Cholesterol dynamics in membranes of raft composition: a molecular point of view from $^2$H and $^{31}$P solid-state NMR. *Biochemistry, 42*, 1383-1390.

Bartels, T., Lankalapalli, R. S., Bittman, R., Beyer, K., & Brown, M. F. (2008). Raftlike Mixtures of Sphingomyelin and Cholesterol Investigated by Solid-State $^2$H NMR Spectroscopy. *J. Am. Chem. Soc., 130*, 14521–14532.

Bittman, R., & Verbicky, C. A. (2000). Methanolysis of sphingomyelin: toward an epimerization-free methodology for the preparation of D-erythro-sphingosylphosphocholine. *J. Lipid Res., 41*, 2089-2093.

Bleecker, J. V., Cox, P. A., & Keller, S. L. (2016). Mixing temperatures of bilayers not simply related to thickness differences between $L_o$ and $L_d$ phases. *Biophys. J., 19*, 55-62.

Bloom, M., Davis, J. H., & Valic, M. I. (1980). Spectral distortion effects due to finite pulse widths in deuterium NMR spectroscopy. *Can. J. Phys., 58*, 1510-1517.

Bloom, M., & Thewalt, J. L. (1994). Spectroscopic determination of lipid dynamics in membranes. *Chem. Phys. Lipids, 73*, 27-38.

Brown, M. F. (1996). Membrane Structure and Dynamics Studied with NMR Spectroscopy. In K. Merz Jr. & B. Roux (Eds.), *Biological Membranes: A Molecular Perspective from Computation and Experiment* (pp. 175–252). Basel: Birkhäuser.

Brown, M. F. (2012). Curvature Forces in Membrane Lipid–Protein Interactions. *Biochemisty, 51*(49), 9782–9795.

Brown, M. F., Lope-Piedrafita, S., Martinez, G. V., & Petrache, H. I. (2006). Solid-State Deuterium NMR Spectroscopy of Membranes. In G. A. Webb (Ed.), *Modern Magnetic Resonance* (pp. in press). Heidelberg: Springer.

Brown, M. F., Thurmond, R. L., Dodd, S. W., Otten, D., & Beyer, K. (2002). Elastic Deformation of Membrane Bilayers Probed by Deuterium NMR Relaxation. *J. Am. Chem. Soc., 124*, 8471–8484.

Bunge, A., Müller, P., Stöckl, M., Herrmann, A., & Huster, D. (2008). Characterization of the Ternary Mixture of Sphingomyelin, POPC, and Cholesterol: Support for an Inhomogeneous Lipid Distribution at High Temperatures. *Biophys. J., 94*, 2680–2690.

Burnett, L. J., & Muller, B. H. (1971). Deuteron quadrupole coupling constants in three solid deuterated paraffin hydrocarbons: $C_2D_6C_4D_{10}$, $C_6D_{14}$. *J. Chem. Phys., 55*, 5829-5831.

Calder, P. C. (2012). Mechanisms of action of (n-3) fatty acids. *J. Nutr., 142*, 592S-599S.

Calder, P. C. (2013). Omega-3 polyunsaturated fatty acids and inflammatory processes: nutrition or pharmacology? *Br. J. Clin. Pharmacol., 75*(3), 645–662. doi:10.1111/j.1365-2125.2012.04374.x

Calder, P. C. (2015). Marine omega-3 fatty acids and inflammatory processes: Effects, mechanisms and clinical relevance. *Biochim. Biophys. Acta, 1851*, 469-484.

Chaikin, P. M., & Lubensky, T. C. (1995). *Principles of Condensed Matter Physics*. Cambridge: Cambridge University Press.

Chapkin, R. S., Wang, N., Fan, Y. Y., Lupton, J. R., & Prior, I. A. (2008). Docosahexaenoic acid alters the size and distribution of cell surface microdomains. *Biochim. Biophys. Acta, 1778*, 466-471.

Cooper, G. M. (2000). *The Cell: A Molecular Approach* (2nd ed.). Sunderland: Sinauer Associates.

Davis, J. H. (1983). The Description of Membrane Lipid Conformation, Order and Dynamics by $^2$H-NMR. *Biochim. Biophys. Acta, 737*, 117-171.

Davis, J. H., Jeffrey, K. R., Bloom, M., Valic, M. I., & Higgs, T. P. (1976). Quadrupolar echo deuteron magnetic resonance spectroscopy in ordered hydrocarbon chains. *Chem. Phys. Lett., 44*, 390-394.

de Gennes, P. G. (1974). *The Physics of Liquid Crystals*. London: Oxford University Press.

Domenici, V. (2009). Quantitative analysis of 2H NMR T1Q, T1Z and T2 relaxation times in the SmA phase of a liquid crystal dendrimer. *Phys. Chem. Chem. Phys., 11*(38), 8496-8506.

Edidin, M. (2003). The state of lipid rafts: from model membranes to cells. *Annu. Rev. Biophys. Biomol. Struct., 32*, 257-283.

Engberg, O., Hautala, V., Yasuda, T., Dehio, H., Murata, M., Slotte, J. P., & Nyholm, T. K. M. (2016). The Affinity of Cholesterol for Different Phospholipids Affects Lateral Segregation in Bilayers. *Biophys. J., 111*(3), 546-556.

Engberg, O., Yasuda, T., Hautala, V., Matsumori, N., Nyholm, T. K. M., Murata, M., & Slotte, J. P. (2016). Lipid interactions and organization in complex bilayer membranes. *Biophys. J.*(110), 1563-1573.

Farquhar, M. G., & Palade, G. E. (1981). The Golgi Apparatus (Complex)-(1954-1981) from Artifact to Center Stage. *J. Cell Biol., 91*(1), 77s-103s.

Feller, S. E., Gawrisch, K., & MacKerell, A. D. (2001). Polyunsaturated fatty acids in lipid bilayers: intrinsic and environmental contributions to their unique physical properties. *J. Am. Chem. Soc., 124*, 318–326.

García-Sáez, A. J., Chiantia, S., & Schwille, P. (2007). Effect of line tension on the lateral organization of lipid membranes. *J. Biol. Chem., 282*(46), 33537-33544.

Georgieva, R., Chachaty, C., Hazarosova, R., Tessier, C., Nuss, P., Momchilova, A., & Staneva, G. (2015). Docosahexaenoic acid promotes micron scale liquid-ordered domains. A comparison study of docosahexaenoic versus oleic acid- containing phosphatidylcholine in raft-like mixtures. *Biochim. Biophys. Acta, 1848*(6), 1424–1435.

Griffin, R. G. (1998). Dipolar recoupling in MAS spectra of biological solids. *Nature Struct. Biol., 5*, 508-512.

Griffiths, D. J. (2005). *Introduction to Quantum Mechanics* (2nd ed.). Upper Saddle River: Pearson.

Gullingsrud, J., & Schulten, K. (2004). Lipid Bilayer Pressure Profiles and Mechanosensitive Channel Gating. *Biophys. J., 86*, 3496–3509.

Häberlen, U. (1976). *High Resolution NMR in Solids. Selective Averaging*. New York: Academic Press.

Hahn, E. L. (1950). Spin echoes. *Phys. Rev., 80*, 580–594.

Harris, M., Kinnun, J. J., Kosaraju, R., Leng, X., & Wassall, S. R. (2016). Membrane disordering by EPA in B lymphomas is reduced by elongation to docosapentaenoic acid as revealed with solid-state NMR spectroscopy of model membranes. *J. Nutr., 146*, 1283-1289.

Harris, W. S., Mozaffarian, D., Lefevre, M., Toner, C. D., Colombo, J., Cunnane, S. C., . . . Whelan, J. (2009). Towards establishing dietary reference intakes for eicosapentaenoic and docosahexaenoic acids. *J. Nutr., 139*(4), 804S–819S.

Heberle, F. A., Petruzielo, R. S., Pan, J., Drazba, P., Kučerka, N., Standaert, R. F., . . . Katsaras, J. (2013). Bilayer Thickness Mismatch Controls Domain Size in Model Membranes. *J. Am. Chem. Soc., 135*(18), 6853–6859.

Hou, T. Y., McMurray, D. N., & Chapkin, R. S. (2016). Omega-3 fatty acids, lipid rafts, and T cell signaling. *Eur. J. Pharmacol, 785*, 2-9.

Hoult, D. I. (2009). The origins and present status of the radio wave controversy in NMR. *Concepts Magn Reson, 34A*(4), 193–216.

Hsueh, Y.-W., Giles, R., Kitson, N., & Thewalt, J. L. (2002). The effect of ceramide on phosphatidylcholine membranes: a deuterium NMR study. *Biophys. J., 82*, 3089-3095.

Israelachvili, J. N., & Wennerström, H. (1992). Entropic Forces between Amphiphilic Surfaces in Liquids. *J. Phys. Chem., 96*, 520-531.

Janiak, M. J., Small, D. M., & Shipley, G. G. (1979). Temperature and Compositional Dependence of the Structure of Hydrated Dimyristoyl Lecithin. *J. Biol. Chem., 254*(13), 6068-6078.

Jouhet, J. (2013). Importance of the hexagonal lipid phase in biological membrane organization. *Front Plant Sci., 4*(494), 1-5.

Kim, W., Fan, Y. Y., Barhoumi, R., Smith, R., McMurray, D. N., & Chapkin, R. S. (2008). n-3 polyunsaturated fatty acids suppress the localization and activation of signaling proteins at the immunological synapse in murine CD4+ T cells by affecting lipid raft formation. *J. Immunol., 181*(9), 6236-6243.

Kinnun, J. J., Leftin, A., & Brown, M. F. (2013). Solid-State NMR Spectroscopy for the Undergraduate Physical Chemistry Laboratory. *J. Chem. Educ., 90*(1), 123–128. doi:10.1021/ed2004774

Kinnun, J. J., Mallikarjunaiah, K. J., Petrache, H. I., & Brown, M. F. (2015). Elastic deformation and area per lipid of membranes: atomistic view from solid-state deuterium NMR spectroscopy. *Biochim. Biophys. Acta, 1848*(1 Pt B), 246–259.

Klein, W. (1990). Nuclear magnetic resonance: Free-induction decay and spin echoes in a 0.05-T magnetic field. *Am. J. Phys., 58*(2), 143–147.

Konyakhina, T. M., & Feigenson, G. W. (2016). Phase diagram of a polyunsaturated lipid mixture: brain sphingomyelin/1-stearoyl-2-docosahexaenoyl-sn-glycero-3-phosphocholine/cholesterol. *Biochim. Biophys. Acta, 1858*, 153–161.

Koynova, R., & Caffrey, M. (1998). Phases and phase transitions of the phosphatidylcholines. *Biochim. Biophys. Acta, 1376*, 91–145.

Kučerka, N., Marquardt, D., Harroun, T. A., Mu-Ping, N., Wassall, S. R., de Jong, D. H., . . . Katsaras, J. (2010). Cholesterol in Bilayers with PUFA Chains: Doping with DMPC or POPC Results in Sterol Reorientation and Membrane-Domain Formation. *Biochemistry, 49*(35), 7485–7493.

Kučerka, N., Nagle, J. F., Sachs, J. N., Feller, S. E., Pencer, J., A., J., & Katsaras, J. (2008). Lipid bilayer structure determined by the simultaneous analysis of neutron and x-ray scattering data. *Biophys. J., 95*, 2356–2367.

Kučerka, N., van Oosten, B., Pan, J., Heberle, F. A., Harroun, T. A., & Katsaras, J. (2015). Molecular structures of fluid phosphatidylethanolamine bilayers obtained from simulation-to-experiment comparisons and experimental scattering density profiles. *J. Phys. Chem. B, 119*, 1947-1956.

Kuzmin, P. I., Akimov, S. A., Chizmadzhev, Y. A., Zimmerberg, J., & Cohen, F. S. (2005). Line Tension and Interaction Energies of Membrane Rafts Calculated from Lipid Splay and Tilt. *Biophys. J., 88*, 1120–1133.

Lafleur, M., Cullis, P. R., & Bloom, M. (1990). Modulation of the orientational order profile of the lipid acyl chain in the L$\alpha$ phase. *Eur. Biophys. J., 19*, 55-62.

Lafleur, M., Fine, B., Sternin, E., Cullis, P. R., & Bloom, M. (1989). Smoothed orientational order profiles of lipid bilayers by [2]H-nuclear magnetic resonance. *Biophys. J., 56*, 1037-1041.

Lands, W. E., M. Inoue, M., Sugiura, Y., & Okuyama, H. (1982). Selective incorporation of polyunsaturated fatty acids into phosphatidylcholine by rat liver microsomes. *J. Biol. Chem., 257*, 14968–14972.

Lange, Y., Tabei, S. M., Ye, J., & Steck, T. L. (2013). Stability and stoichiometry of bilayer phospholipid-cholesterol complexes: relationship to cellular sterol distribution and homeostasis. *Biochemistry, 52*, 6950-6959.

Leventhal, I., Grzybek, M., & Simons, K. (2010). Greasing their way: lipid modifications determine protein association with membrane rafts. *Biochemistry, 49*, 6305–6316.

Leventhal, I., & Veatch, S. L. (2016). The continuing mystery of lipid rafts. *J. Mol. Biol., 428*, 4749-4764.

Levental, K. R., Lorent, J. H., Skinkle, A. D., Surma, M. A., Stockenbojer, E. A., Gorfe, A. A., & Levental, I. (2016). Polyunsaturated lipids regulate membrane domain stability by tuning membrane order. *Biophys. J., 110*, 1800-1810.

Levitt, M. H. (2008). *Spin Dynamics: Basics of Nuclear Magnetic Resonance* (2nd ed.). Chichester: John Wiley & Sons.

Lin, X., Lorent, J. H., Skinkle, A. D., Levental, K. R., Waxham, M. N., Gorfe, A. A., & Levental, I. (2016). Domain Stability in Biomimetic Membranes Driven by Lipid Polyunsaturation. *J. Phys. Chem. B, 120*, 11930−11941.

Lindblom, G., & Orädd, G. (2009). Lipid lateral diffusion and membrane heterogeneity. *Biochim. Biophys. Acta, 1788*, 234–244.

Lingwood, D., & Simons, K. (2010). Lipid rafts as a membrane-organizing principle. *Science, 327*, 46–50.

Ma, D. W. L., Seo, J., Switzer, K. C., Fan, Y., N., M. D., R., L. J., & Chapkin, R. S. (2004). n-3 PUFA and membrane microdomains: a new frontier in bioactive lipid research. *J. Nutr. Biochem., 15*, 700-706.

Mannock, D. A., McIntosh, T. J., Jiang, X., Covey, D. F., & McElhaney, R. N. (2003). Effects of natural and enantiomeric cholesterol on the thermotropic phase behavior and structure of egg sphingomyelin bilayer membranes. *Biophys. J., 84*, 1038-1046.

Mansfield, P. (1965). Multiple-Pulse Nuclear Magnetic Resonance Transients in Solids. *Phys. Rev., 137*, A961–A974.

Mathworks. (2017, December 5). MATLAB. Retrieved from www.mathworks.com

McCabe, M. A., & Wassall, S. R. (1997). Rapid deconvolution of NMR powder spectra by weighted fast Fourier transformation. *Solid State Nucl. Magn. Reson., 10*, 53-61.

McConnell, H. M. (1991). Structures and Transitions in Lipid Monolayers at the Air-Water Interface. *Annu. Rev. Phys. Chem., 42*, 171-195.

McKee, T., & McKee, J. R. (2015). *Biochemistry: The Molecular Basis of Life* (6th ed.). New York: Oxford.

McKersie, B. D., & Thompson, J. E. (1979). Influence of Plant Sterols on the Phase Properties of Phospholipid Bilayers. *Plant Physiol., 63*, 802-805.

Morrison, C., & Bloom, M. (1993). General orientation dependence of NMR spin-lattice relaxation for spin 1. *J. Magn. Reson. A, 103*, 1-7.

Morrison, C., & Bloom, M. (1994). Orientation Dependence of $^{2}$H Nuclear Magnetic Resonance Spin-Lattice Relaxation in Phospholipid and Phospholipid:Cholesterol Systems. *J. Chem. Phys., 101*, 749-763.

Mozaffarian, D., & Wu, J. H. Y. (2011). Omega-3 fatty acids and cardiovascular disease: effects on risk factors, molecular pathways, and clinical events. *J. Am. Coll. Cardiol., 58*, 2047-2067.

Nicolson, G. L. (2014). The Fluid—Mosaic Model of Membrane Structure: Still relevant to understanding the structure, function and dynamics of biological membranes after more than 40 years. *Biochim. Biophys. Acta, 1838*(6), 1451–1466.

Pake, G. E. (1948). Nuclear Resonance Absorption in Hydrated Crystals: Fine Structure of the Proton Line. *J. Chem. Phys., 16*(4), 327-336.

Pallas, N. R., & Harrison, Y. (1990). An automated drop shape apparatus and the surface tension of pure water. *Colloids Surf., 43*(2), 169–194.

Palmer, A. G., & Dinshaw, A. J. (2002). Kurt Wüthrich and NMR of Biological Macromolecules. *Structure, 10*(12), 1603–1604.

Pathak, P., & London, E. (2011). Measurement of lipid nanodaomain (raft) formation and size in sphingomyelin/POPC/cholesterol vesicles shows TX-100 and transmembrane helices increase domain size by coalescing preexisting nanodomains but do not induce domain formation. *Biophys. J., 101*, 2417-2525.

Pathak, P., & London, E. (2015). The effect of membrane lipid composition on the formation of lipid ultrananodomains. *Biophys. J., 109*, 1630-1638.

Patterson, E., Wall, R., Fitzgerald, G. F., Ross, R. P., & Stanton, C. (2012). Health Implications of High Dietary Omega-6 Polyunsaturated Fatty Acids. *Journal of Nutrition and Metabolism, 2012*, 16 pages. doi:10.1155/2012/539426

Petrache, H. I., Dodd, S. W., & Brown, M. F. (2000). Area per lipid and acyl length distributions in fluid phosphatidylcholines determined by $^2$H NMR spectroscopy. *Biophys. J., 79*, 3172–3192.

Petrache, H. I., Feller, S. E., & Nagle, J. F. (1997). Determination of Component Volumes of Lipid Bilayers from Simulations. *Biophys. J., 72*, 2237–2242.

Petrache, H. I., Tu, K., & Nagle, J. F. (1999). Analysis of Simulated NMR Order Parameters for Lipid Bilayer Structure Determination. *Biophys. J., 76*, 2479–2487.

Petruzielo, R. S., Heberle, F. A., Drazba, P., Katsaras, J., & Feigenson, G. W. (2013). Phase behavior and domain size in sphingomyelin-containing lipid bilayers. *Biochim. Biophys. Acta, 1828*, 1302-1313.

Pius, J., Morrow, M. R., & Booth, V. (2012). $^2$H Solid-State Nuclear Magnetic Resonance Investigation of Whole Escherichia coli Interacting with Antimicrobial Peptide MSI-78. *Biochemistry, 51*(1), 118–125.

Rockett, B. D., Melton, M., Harris, M., Bridges, L. C., & Shaikh, S. R. (2013). Fish oil disrupts MHC class II lateral organization on the B-cell side of the immunological synapse independent of B-T cell adhesion. *J. Nutr. Biochem., 24*, 1810-1816.

Rockett, B. D., Teague, H., Harris, M., Melton, M., Williams, J. A., Wassall, S. R., & Shaikh, S. R. (2012). Fish oil increases raft size and membrane order of B cells accompanied by differential effects on function. *J. Lipid Res., 53*, 674-685.

Salmon, A., Dodd, S. W., Williams, G. D., Beach, J. M., & Brown, M. F. (1987). Configurational Statistics of Acyl Chains in Polyunsaturated Lipid Bilayers from $^2$H NMR. *J. Am. Chem. Soc., 109*, 2600–2609.

Schmidt-Rohr, K. S., H. W. (1996). *Multidimensional Solid-State NMR and Polymers*. San Diego: Academic Press Inc.

Seelig, J. (1977). Deuterium Magnetic Resonance: Theory and Application to Lipid Membranes. *Q. Rev. Biophys., 10*, 353-418.

Seelig, J., & Waespe-Sarcevic, N. (1978). Molecular order in cis and trans unsaturated phospholipid bilayers. *Biochemistry, 17*, 3310-3315.

Separovic, F., & Cornell, B. P., R. (2000). Orientation dependence of NMR relaxation time, $T_{1\rho}$, in lipid bilayers. *Chem. Phys. Lipids, 107*(2), 159–167.

Shaikh, S. R. (2012). Biophysical and biochemical mechanisms by which dietary N-3 polyunsaturated fatty acids from fish oil disrupt membrane lipid rafts. *J. Nutr. Biochem., 23*, 101-105.

Shaikh, S. R., Brzustowicz, M. R., Gustafson, N., Stillwell, W., & Wassall, S. R. (2002). Monounsaturated PE Does Not Phase-Separate from the Lipid Raft Molecules Sphingomyelin and Cholesterol: Role for Polyunsaturation? *Biochemistry, 41*, 10593–10602.

Shaikh, S. R., Cherezov, V., Caffrey, M., Stillwell, W., & Wassall, S. R. (2003). Interaction of cholesterol with a docosahexaenoic acid-containing phosphatidylethanolamine: trigger for microdomain/raft formation? . *Biochemistry, 42*, 12028-12037.

Shaikh, S. R., Dumaual, A. C., Castillo, A., LoCascio, D., Siddigui, R. A., Stillwell, W., & Wassall, S. R. (2004). Oleic and docosahexaenoic acid differentially phase separate from lipid raft molecules: a comparative NMR, DSC, AFM, and detergent extraction study. *Biophys. J., 87*(3), 1752–1766.

Shaikh, S. R., Kinnun, J. J., Leng, X., Williams, J. A., & Wassall, S. R. (2015). How polyunsaturated fatty acids modify molecular organization in membranes: insight from NMR studies of model systems. *Biochim. Biophys. Acta, 1848*(1 Pt B), 211–219. doi:10.1016/j.bbamem.2014.04.020

Shaikh, S. R., LoCascio, D., Soni, S. P., Wassall, S. R., & Stillwell, W. (2009). Oleic- and docosahexaenoic acid-containing phosphatidylethanolamines differentially phase separate from sphingomyelin. *Biochim. Biophys. Acta, 1788*(11), 2421–2426.

Shaikh, S. R., Wassall, S. R., Brown, D. A., & R. Kosaraju, R. (2015). n-3 Polyunsaturated fatty acids, lipid clusters and vitamin E. *Curr. Top. Membr., 75*, in press.

Shampo, M. A., Kyle, R. A., & Steensma, D. P. (2012). Richard Ernst—Nobel Prize for Nuclear Magnetic Resonance Spectroscopy. *Mayo Clin Proc., 87*(12), e109.

Simons, K., & Toomre, D. (2000). Lipid rafts and signal transduction. *Nat. Rev. Mol. Cell Biol., 1*, 31-39.

Simopoulos, A. P. (2002). Omega-3 fatty acids in inflammation and autoimmune diseases. *J. Am. Coll. Nutr., 21*, 495–505.

Soni, S. P., LoCascio, D., Liu, Y., Williams, J. A., Bittman, R., Stillwell, W., & Wassall, S. R. (2008). Docosahexaenoic acid enhances segregation of lipids between raft and non-raft domains. *Biophys. J., 95*(1), 203–214.

Soubias, O., & Gawrisch, K. (2007). Docosahexaenoyl chains isomerize on the sub-nanosecond time scale. *J. Am. Chem. Soc., 129*, 6678–6679.

Spiess, H. W., & Steigel, A. (1978). *Dynamic NMR Spectroscopy*. New York: Springer-Verlag.

Sternin, E., Bloom, M., & MacKay, A. L. (1983). De-Pake-ing of NMR spectra. *J. Magn. Reson., 55*, 274-282.

Stillwell, W. (2013). *An Introduction to Biological Membranes: From Bilayers to Rafts*. Amsterdam: Elsevier.

Stillwell, W. (2015). *An Introduction to Biological Membranes: Composition, Structure and Function* (2nd ed.). Amsterdam: Elsevier.

Stillwell, W., Shaikh, S. R., Zerouga, M., Siddiqui, R., & Wassall, S. R. (2005). Docosahexaenoic acid affects cell signaling by altering lipid rafts. *Reprod. Nutr. Dev., 45*, 559-579.

Stillwell, W., & Wassall, S. R. (2003). Docosahexaenoic acid: membrane properties of a unique fatty acid. *Chem. Phys. Lipids, 126*, 1–27.

Tanford, C. (1980). *The hydrophobic effect, 2nd Edition* (2nd ed.). New York: John Wiley and Sons.

Teague, H., Ross, R., Harris, M., Mitchell, D. C., & Shaikh, S. R. (2012). DHA-fluorescent probe is sensitive to membrane order and reveals molecular adaptation of DHA in ordered lipid microdomains. *J. Nutr. Biochem., 24*, 188-195.

Turk, H. F., & Chapkin, R. S. (2013). Membrane lipid raft organization is uniquely modified by n-3 polyunsaturated fatty acids. *Prost. Leuk. Essent. Fatty Acids, 88*(1), 43–47.

van Meer, G., Voelker, D. R., & Feigenson, G. W. (2008). Membrane Lipids: Where They Are and How They Behave. *Nat. Rev. Mol. Cell Biol., 9*(2), 112–124.

Veatch, S. L., & Keller, S. L. (2003a). A closer look at the canonical raft mixture in model membrane studies. *Biophys. J., 84*, 725-726.

Veatch, S. L., & Keller, S. L. (2003b). Separation of Liquid Phases in Giant Vesicles of Ternary Mixtures of Phospholipids and Cholesterol. *Biophys. J., 85*, 3074–3083.

Veatch, S. L., Polozov, I. V., Gawrisch, K., & Keller, S. L. (2004). Liquid domains in vesicles investigated by NMR and fluorescence microscopy. *Biophys. J., 86*, 2910-2922.

Wassall, S. R., & Stillwell, W. (2008). Docosahexaenoic acid domains: the ultimate non-raft membrane domain. *Chem. Phys. Lipids, 153*, 57–63.

Wassall, S. R., & Stillwell, W. (2009). Polyunsaturated fatty acid-cholesterol interactions: domain formation in membranes. *Biochim. Biophys. Acta, 1788*, 24-32.

Wassall, S. R., Thewalt, J. L., Wong, L., Gorrissen, H., & Cushley, R. J. (1986). Deuterium NMR Study of the Interaction of α-Tocopherol with a Phospholipid Model Membrane. *Biochemistry, 25*, 319-326.

Williams, J. A., Batten, S. E., Harris, M., Rockett, B. D., Shaikh, S. R., Stillwell, W., & Wassall, S. R. (2012). Docosahexaenoic and Eicosapentaenoic Acids Segregate Differently between Raft and Nonraft Domains. *Biophys. J., 103*(2), 228–237.

Yaqoob, P., & Shaikh, S. R. (2010). The nutritional and clinical significance of lipid rafts. *Curr. Opin. Clin. Nutr. Metab. Care, 13*, 156–166.

Yasuda, T., Tsuchikawa, H., Murata, M., & Matsumori, N. (2015). Deuterium NMR of Raft Model Membranes Reveals Domain-Specific Order Profiles and Compositional Distribution. *Biophys. J., 108*(10), 2502-2506.

Zech, T., Ejsing, C. S., Gaus, K., de Wet, B., Shevchenko, A., Simons, K., & Harder, T. (2009). Accumulation of raft lipids in T-cell plasma membrane domains engaged in TCR signalling. *EMBO J., 28*(5), 466-476.

**VITA**

**Education**

Indiana University Purdue University Indianapolis, Indianapolis, IN 46202

Doctor of Philosophy, Physics, May 2018

Cumulative GPA:  3.9/4.0

Dissertation Title: Solid-State NMR Spectroscopy Applied to Model Membranes: Effects
of Polyunsaturated Fatty Acids

University of Arizona, Tucson, AZ 85721

Master of Science, Physics, May 2011

Cumulative GPA:  3.3/4.0

Thesis Title: Solid-State $^2$H NMR Spectroscopy and Osmotic Stress Applied to Membrane
Deformation

University of Arizona, Tucson, AZ 85721

Bachelor of Science, Physics; Minors: Chemistry & Mathematics, May 2008

Cumulative GPA:  3.7/4.0

Mohave Community College, Lake Havasu City, AZ 86403

Associate of Science, Chemistry, April 2005

Cumulative GPA:  3.8/4.0

**Research Experience**

Indiana University Purdue University Indianapolis, Indianapolis, IN 46202

Graduate Research Assistant (12/2012–12/2017)

Advisor: Stephen R. Wassall

I led a research program on the effect of DHA (found in fish oil supplements) on lipid rafts in model cellular membranes. This involved sample preparation in low-oxygen and light-sensitive conditions. To study this system, I repaired and operated nuclear magnetic resonance and electron spin resonance

(originally non-functional) spectrometers. Finally, I designed and coded custom processing and analysis software for the repaired spectrometers.

University of Arizona, Tucson, AZ 85721

Graduate Research Assistant (5/2008–12/2012)

Advisor: Michael F. Brown

I co-developed a research program on studying the effects of dehydration and osmotic pressure on model cellular membranes. Here I helped design a protocol to finely control sample hydration by vacuum sealing it in a glass ampule under cryogenic conditions. I also helped develop theory and analysis techniques to process data obtained in nuclear magnetic resonance spectroscopy and x-ray scattering techniques.

**Teaching Experience**

Indiana University Purdue University Indianapolis, Indianapolis, IN 46202

Teaching Assistant (12/2012–Present)

Mechanics: Laboratory Instructor (6 semesters) and Recitation Instructor (3 semesters)

General Physics I: Laboratory Instructor (2 semesters) and Recitation Instructor (1 semester)

General Physics II: Primary Lecturer (1 semester) and Laboratory Instructor (2semesters)

Heat, Electricity & Optics: Laboratory Instructor (4 semesters) and Recitation Instructor (2 semesters)

Physics Learning Space: Tutored students on the principles of physics (2 semesters)

University of Arizona, Tucson, AZ 85721

Teaching Assistant (5/2011–12/2012)

Introductory Mechanics: Laboratory Instructor (1 semester)

Nuclear Magnetic Resonance Spectroscopy: Substitute Lecturer (approx. four lectures)

**Honors/Awards**

January 28th, 2018 – Biophysical Journal New and Notable Article (Volume 114, Issue 2)

April 20th, 2017 – ACS "Think Like a Molecule Poster Session" ACS Chair Award, 3rd place

April 1st, 2017 – IUPUI Outstanding Physics Graduate Student Award

March 8th, 2017 – IUPUI School of Science Graduate Student Council Travel Grant

March 3rd, 2017 – IUPUI Graduate Student Travel Fellowship

January 23rd, 2017 – IUPUI GPSG Graduate and Professional Education Travel Grant

April 6th, 2016 – IUPUI GPSG Graduate and Professional Education Travel Grant

March 9th, 2016 – IUPUI School of Science Graduate Student Council Travel Grant

February 25th, 2016 – ACS "Think Like a Molecule Poster Session" IUPUI Dean's Award, 1st place

May 2nd, 2014 – American Association of Physics Teachers Outstanding Physics Teaching Assistant Award

November 9th, 2013 – IUPUI School of Science Graduate Student Council Travel Grant

January 29th, 2013 – IUPUI Department of Physics Travel Grant

November 16th, 2012 – Biophysical Society Educational Committee Travel Award

August 2008 through May 2009 – University of Arizona Biological Physics Program Fellow

May 2008 – University of Arizona Department of Physics Outstanding Senior Project Award

Fall 2007 – University of Arizona Department of Physics Weaver Award for Undergraduate Research

Spring 2005 – Mohave Community College Award in Chemistry


**Publications**

J. J. Kinnun, R. Bittman, S. R. Shaikh, and S. R. Wassall. (2018) DHA Modifies the Size and Composition of Raft-like Domains: A Solid State 2H NMR Study. *Biophys. J.* **114**: 380–391

X. Leng, J. J. Kinnun, A. T. Cavazos, S. W. Canner, S. R. Shaikh, S. E. Feller, and S. R. Wassall. (2018) All n-3 PUFA are not the same: MD simulations reveal differences in membrane organization for EPA, DHA and DPA. *Biochim. Biophys. Acta* **1860**: 211–219

D. Marquardt, F. A. Heberle, D. V. Greathouse, R. E. Koeppe III, R. F. Standaert, B. J. Van Oosten, T. A. Harroun, J. J. Kinnun, J. A. Williams, S. R. Wassall, and J. Katsaras. (2016) Lipid Bilayer Thickness Determines Cholesterol's Location in Model Membranes. *Soft Matter* **12**: 9393–9594

M. Harris, J. J. Kinnun, R. Kosarajua, X. Leng, S. R. Wassall, S. R. Shaikh. (2016) Membrane Disordering by Eicosapentaenoic Acid in B Lymphomas Is Reduced by Elongation to Docosapentaenoic Acid as Revealed with Solid-State Nuclear Magnetic Resonance Spectroscopy of Model Membranes. *J. Nutr.* **146:** 1283–1289

X. Leng, J. J. Kinnun, D. Marquardt, M. Ghefli, N. Kučerka, J. Katsaras, J. Atkinson, T. A. Harroun, S. E. Feller, and S. R. Wassall. (2015) α-Tocopherol Is Well Designed to Protect Polyunsaturated Phospholipids: MD Simulations. *Biophys. J.* **109**: 1608–1618

J. J. Kinnun, K. J. Mallikarjunaiah, H. I. Petrache, and M. F. Brown. (2015) Area per lipid and elastic deformation of membranes: Atomistic view from solid-state deuterium NMR spectroscopy. *Biochim. Biophys. Acta* **1848**: 246–259

S. R. Shaikh, J. J. Kinnun, X. Leng, J. A. Williams, S. R. Wassall. (2015) How polyunsaturated fatty acids modify molecular organization in membranes: Insight from NMR studies of model systems. *Biochim. Biophys. Acta* **1848**: 211–219

D. Marquardt, J. A. Williams, J. J. Kinnun, N. Kučerka, J. Atkinson, S. R. Wassall, J. Katsaras, and T. A. Harroun. (2014) Dimyristoyl Phosphatidylcholine: A Remarkable Exception to α-Tocopherol's Membrane Presence. *J. Am. Chem. Soc.* **136**: 203–210

J. J. Kinnun, A. Leftin, and M. F. Brown. (2013) Solid-State NMR Spectroscopy for the Undergraduate Physical Chemistry Laboratory. *J. Chem. Ed.* **90**: 123–128

K. J. Mallikarjunaiah, A. Leftin, J. J. Kinnun, M. J. Justice, A. L. Rogozea, H. I. Petrache, and M. F. Brown. (2011) Solid-State $^2$H NMR Shows Equivalence of Dehydration and Osmotic Pressures in Lipid Membrane Deformation. *Biophys. J.* **100**: 98–107

**Platform Talks**

March 25$^{th}$, 2017 – "PUFA: A Raft-Domain Driving Force", 132$^{nd}$ Annual Indiana Academy of Science Meeting, Indianapolis, Indiana

February 14$^{th}$, 2017 – "Raft-like Domains Are Driven Together by PUFA", 61$^{st}$ Annual Biophysical Society Meeting, New Orleans, Louisiana

November 10$^{th}$, 2016 – "Solid State $^2$H NMR Spectroscopy Reveals How PUFA Alter Membrane Structure", IUPUI Department of Physics Public Colloquium, Indianapolis, Indiana

March 26$^{th}$, 2016 – "Raft Busters: A Molecular Role for DHA in Biological Membranes", 131$^{st}$ Annual Indiana Academy of Science Meeting, Indianapolis, Indiana

March 21$^{th}$, 2015 – "Solid State $^2$H NMR Reveals that DHA Disorders Raft-like Domains in Model Membranes", 130$^{th}$ Annual Indiana Academy of Science Meeting, Indianapolis, Indiana

May 12$^{th}$, 2014 – "Intermembrane Forces and Membrane Deformation Observed via Dehydration and Osmotic Pressure", 3$^{rd}$ Annual Bluegrass Molecular Biophysics Symposium, Lexington, Kentucky

March 9$^{th}$, 2013 – "DHA and EPA Interaction with Raft Domains Observed with Solid-State $^2$H NMR Spectroscopy", 128$^{th}$ Annual Indiana Academy of Science Meeting, Indianapolis, Indiana

March 10$^{th}$, 2012 – "Biomembrane Deformation and Intermembrane Forces Probed by Osmotic Stress and Dehydration", 127$^{th}$ Annual Indiana Academy of Science Meeting, West Lafayette, Indiana

October 21$^{st}$, 2011 – "Biomembrane Structure and Dynamics Controlled by Dehydration and Osmotic Stress", American Physical Society 4CS Meeting, Tucson, Arizona

April 2011 – "Modulating Membrane Structure and Dynamics with Osmotic Stress", 8$^{th}$ Annual Arizona Biophest, Tempe, Arizona

March 2011 – "Thermodynamic Equivalence of Hydration and Osmotic Stress in Membrane Deformation", 55$^{th}$ Annual Biophysical Society Meeting, Baltimore, Maryland

April 2010 – "Theoretical Equivalence of Hydration and Osmotic Pressure in Membrane Deformation", 7$^{th}$ Annual Arizona Biophest, Tucson, Arizona

May 2009 – "Theoretical Interpretation of Biomembrane Deuterium NMR Data", 6$^{th}$ Annual Arizona Biophest, Phoenix, Arizona

May 2008 – "Solid-State $^2$H NMR Spectroscopy for the Undergraduate Physics Laboratory", University of Arizona Department of Physics Undergraduate Symposium, Tucson, Arizona

**Poster Presentations**

April 20$^{th}$, 2017 – "DHA Drives Domain Formation in Model Raft Membranes", American Chemical Society Think Like a Molecule Poster Session, Indianapolis, Indiana

April 8$^{th}$, 2016 – "Raft Busters: A Molecular Role for DHA in Biological Membranes", IUPUI Research Day, Indianapolis, Indiana

February 28$^{th}$, 2016 – "Solid-state $^2$H NMR Reveals the Impact of DHA on Molecular Organization in Raft-like Domains", 60$^{th}$ Annual Biophysical Society Meeting, Los Angeles, California

February 25th, 2016 – "Solid-state $^2$H NMR Reveals the Impact of DHA on Molecular Organization in Raft-like Domains", American Chemical Society Think Like a Molecule Poster Session, Indianapolis, Indiana

April 17th, 2015 – "DHA Alters Raft-like Membrane Domains as Revealed by Solid State $^2$H NMR Spectroscopy", IUPUI Research Day, Indianapolis, Indiana

February 9th, 2015 – "DHA Disorders Raft-like Domains as Revealed by Solid State $^2$H NMR", 59th Annual Biophysical Society Meeting, Baltimore, Maryland

February 10th, 2014 – "Solid State $^2$H NMR Studies of the Disordering of Raft-like Domains by N-3 PUFA", 58th Annual Biophysical Society Meeting, San Francisco, California

February 2014 – "Intermembrane Forces & Membrane Deformation Observed via Dehydration & Osmotic Pressure", 58th Annual Biophysical Society Meeting, San Francisco, California

April 5th, 2013 – "DHA and EPA Interaction with Raft Domains Observed with Solid-State $^2$H NMR Spectroscopy", IUPUI Research Day, Indianapolis, Indiana

February 2013 – "Membrane Structure and Intermembrane Forces Observed with Small Angle X-Ray Scattering", 57th Annual Biophysical Society Meeting, Philadelphia, Pennsylvania

February 2013 – "Disordering of Raft Domains BY DHA and EPA Observed with Solid-State $^2$NMR Spectroscopy", 57th Annual Biophysical Society Meeting, Philadelphia, Pennsylvania

February 2010 – "Osmotic Membrane Deformation Revealed by $^2$H NMR and Small-Angle X-Ray Scattering", 54th Annual Biophysical Society Meeting, San Francisco, California

February 2010 – "Collective Membrane Dynamics under Osmotic Stress", 54th Annual Biophysical Society Meeting, San Francisco, California

February 2009 – "Structural and Dynamical Markers of Membrane Osmotic Stress from X-Ray Scattering and Solid-State $^2$H NMR", 53rd Annual Biophysical Society Meeting, Boston, Massachusetts

April 2008 – "Solid-State $^2$H NMR Spectroscopy for the Undergraduate Physical Chemistry Laboratory", University of Arizona Undergraduate Chemistry Fair, Tucson, Arizona


**Leadership/Service**

Indianapolis Project Seed

Mentor (2013, 2014, 2015, 2016, and 2017)

I mentored disadvantaged high school students as they gained hands-on experience in science over the summer months. Students in this program are

monetarily compensated and, at the culmination of their time, they present their research to their peers.

High School Summer Research in Physics at IUPUI
Mentor (2013 and 2017)

I mentored high school students as they gained research experience in physics laboratories during the summer. Before the culmination of the summer, the students present the final outcome of their research to peers and other laboratory members.

Girls Rock Indianapolis
Equipment Assistant and Videographer (2014, 2015, 2016, and 2017)

I helped transport musical equipment, and record performances, for a camp aimed at promoting girl's self-confidence through music.

Indiana Academy of Science
Physics Demonstration Assistant (2015 and 2016)

I demonstrated physical principles using, sound, magnetism, and lasers, aimed at inspiring high school students in pursuing a career in science.

Science Fair Judge (2014, 2015 and 2016)

I judged scientific projects conducted and presented by elementary and middle school students at the Building Blocks Academy in Indianapolis, IN.

Mohave Community College Student Council
Student Senator (2005)

**Professional Affiliations**
American Physical Society
Biophysical Society
Indiana Academy of Science